First measurements of the *a*SPECT spectrometer

Dissertation
zur Erlangung des Grades
Doktor der Naturwissenschaften
am Institut für Physik
der Johannes Gutenberg-Universität Mainz

vorgelegt von
Raquel Muñoz Horta
geboren in Riudellots de la Selva

Mainz am Rhein, February 2011

Als meus pares,

Zusammenfassung

Ziel des aSPECT Experimentes ist, das Protonenergiespektrum beim freien Neutronenzerfall mit höchster Präzision zu messen. Aus diesem Spektrum kann der Neutrino-Elektron-Winkelkorrelationsparameter a abgeleitet werden, der in verschiedenen Tests des Standardmodell eine Rolle spielt, so z.B. für den Unitaritätstest der Cabibbo-Kobayashi-Maskawa Quarkmischungsmatrix. aSPECT wurde geplant um den Parameter a mit einer Präzision besser als 3×10^{-4} zu bestimmen, was eine Verbesserung um eine Größenordnung gegenüber der besten bisherigen Messung darstellt. Die ersten Messungen des aSPECT Spektrometer mit Neutronenstrahl wurden an der Forschungsneutronenquelle Heinz Maier-Leibnitz in München durchgeführt. In dieser Arbeit werden die dabei gewonnenen Daten analysiert, womit zum einen das Funktionsprinzips von aSPECT nachgewiesen wird. Andererseits verhindert die Beobachtung von nicht reproduzierbaren und zeitabhängigen Schwankungen des Messuntergrundes die Bestimmung eines neuen Wertes des Parameters a. Mit dem Ziel, das aSPECT Spektrometer für weitere Strahlzeiten zu optimieren, wurde daher eine detaillierte Analyse der Daten und Untergrundschwankungen durchgeführt. Als Ergebnis dieser Untersuchungen konnten in Fallen gefangene Teilchen als (wahrscheinlichste) Ursache der Hintergrundschwankungen identifiziert werden. Außerdem wurde festgestellt, dass die Werte für a die aus Messungen mit weniger gefangenen Teilchen im Spektrometer bestimmt wurden deutlich besser mit dem aktuellen Wert der Particle Data Group übereinstimmen, als solche die aus Messperioden mit einer höheren Anzahl von gefangenen Teilchen bestimmt wurden. Basierend auf diesen Erkenntnissen werden verschiedene Massnahmen vorgeschlagen um mögliche Teilchenfallen im Spektrometer zu eliminieren. Der Erfolg der vorgeschlagenen und realisierten Massnahmen wurde mittlerweile bei neuen Messungen des aSPECT Spektrometer nachgewiesen, bei denen die beobachtbaren Untergrundschwankungen deutlich reduziert waren (Referenzen [Aya11] [Bor11] [Kon11] [Sim10] in Vorbereitung).

Abstract

The aSPECT spectrometer has been constructed to measure, with high precision, the integral proton spectrum of the free neutron decay. From this spectrum the neutrino electron angular correlation coefficient a can be inferred. The coefficient a is involved in several Standard Model tests, like the unitarity test of the Cabibbo-Kobayashi-Maskawa quark mixing matrix. aSPECT has been designed to determine the coefficient a with an accuracy better than 3×10^{-4}, that is, one order of magnitude better than the best current accuracy. First measurements with neutron beam with the aSPECT spectrometer were performed in the Forschungsneutronenquelle Heinz Maier-Leibnitz, in Munich. A study of the data taken in this period is presented in this thesis, demonstrating the proof of principle of the spectrometer. However, the observation of situation and time-dependent background instabilities impedes the report of a new value of the coefficient a. A thorough data analysis is carried out to identify sources of these background instabilities in order to improve the aSPECT experiment for future beam times. The investigation indicates that trapped particles are most likely the reason for the background problems. Furthermore, it has been observed that measurements containing less trapped particles provide a-values closer to the currently Particle Data Group value. Based on this findings, different measures are proposed to eliminate potential traps in the spectrometer. Indeed, with the proposed modifications realized for the following beam-times, the observed background instabilities were greatly reduced (References [Aya11] [Bor11] [Kon11] [Sim10] in preparation).

Contents

Introduction

The unique properties of the neutron permit to use it either as a probe or as an object of study. The neutron experiences all known forces (electromagnetic, gravitational, strong and weak) in strengths accessible to experiments. It is electrically neutral and outside the nucleus unstable with a mean lifetime of about 15 minutes. There exist a quite broad range of neutron energies for use in laboratory research, although most fundamental neutron physics experiments are performed with slow neutrons, i.e. neutrons with energy below 30 meV and wavelengths compatible to the atomic spacing in solids and liquids. Therefore, slow neutron scattering is a very appropriate tool to obtain information about materials, for example concerning their magnetic structure.

But besides solid state physics, experiments involving neutrons become an integral part of investigations in fields as diverse as nuclear and particle physics, astrophysics, cosmology or gravitation. These experiments provide complementary information to that available from existing accelerator-based nuclear physics facilities and high-energy accelerators. In particular, neutron decay is an important process for the investigation of the Standard Model of electroweak interactions. It is sensitive to certain Standard Model extensions in the charged-current electroweak sector and it is used in the search of CP-symmetry and/or time-reversal violations.

Precise measurements of the decay of the free neutron provide a large number of observables. Combined, these observables can be used to determine the Cabibbo-Kobayashi-Maskawa (CKM) matrix element V_{ud} in several independent ways. Also, the existence of scalar and tensor interactions or right-handed currents may be inferred.

In this thesis, first measurements with the aSPECT retardation spectrometer are presented, from which, the value of the angular correlation coefficient a, can be extracted.

One way of inferring the coefficient a is to measure precisely the proton recoil spectrum of the free neutron decay. The shape of this spectrum is sensitive to the electron antineutrino angular correlation coefficient a since it can be written as [Nac68]:

$$w_p(T) \propto g_1(T) + a g_2(T)$$

where T is the kinetic energy of the proton and g_1 and g_2 are functions of T and the masses of the participating particles. A deeper discussion of the theoretical background is given in Chapter 1.

Retardation spectrometers like aSPECT have been used successfully in the past in experiments requiring both good energy resolution and large solid angle acceptance [Lob85].

In *a*SPECT the two requirements are achieved by employing spatially slowly varying electromagnetic fields. Details of the *a*SPECT experimental setup are presented in Chapter 2.

Turning to the free neutron decay, the differential decay rate for a fixed electron energy E_e can be expressed as:

$$d\omega \ \propto 1 + a\frac{\vec{p}_e\vec{p}_{\bar{\nu}}}{E_e E_{\bar{\nu}}} + \vec{\sigma}_n\left(A\frac{\vec{p}_e}{E_e} + B\frac{\vec{p}_{\bar{\nu}}}{E_{\bar{\nu}}}\right)$$

where $\vec{p}_e$, $\vec{p}_{\bar{\nu}}$, E_e, $E_{\bar{\nu}}$ are the momenta and the energies of the electron and the antineutrino, respectively. m_e is the electron mass and $\vec{\sigma}_n$ is the polarization vector of the neutron.

a, A and B are angular correlation coefficients. a is the angular correlation coefficient between electron momentum and antineutrino momentum, whereas A is the angular correlation coefficient between the polarization of the neutron and the electron's momentum. Within the Standard Model (V-A theory), both angular coefficients a and A depend on λ, the ratio of the weak axial-vector and vector coupling constants g_A and g_V, as follows:

$$a = \frac{1 - |\lambda|^2}{1 + 3|\lambda|^2}$$

$$A = -2\frac{|\lambda|^2 + Re(\lambda)}{1 + 3|\lambda|^2}$$

A measurement of one of these angular coefficients makes possible the determination of the parameter λ. The combination of λ measurements together with the lifetime of the neutron τ_n determines the matrix element V_{ud} [Ams08]:

$$|V_{ud}|^2 = \frac{4908.7(1.9)sec}{\tau_n(1 + 3\lambda^2)} \tag{1}$$

In addition, the comparison of λ values obtained independently from measurements of A and a provides a test of the $V - A$ theory.

The accuracy of the present best experiments for a is $\Delta a/a = 5\%$ [Str78] [Byr02], which is too small to extract results with comparable precision to other observables extracted from free neutron decay, like for example the coefficient A which is known to $\Delta A/A \simeq 1\%$ as stated by the Particle Data Group [Ams08]. The *a*SPECT spectrometer has been designed in order to improve the accuracy of the measurement of the coefficient a by one order of magnitude. The process of data taking and the procedure followed to extract the coefficient a from the measured proton spectrum are explained in Chapter 3. Results from the first *a*SPECT beam-time periods at the Forschungsneutronenquelle Heinz Maier-Leibnitz (FRM-II) in Munich are presented in Chapters 4 and 5.

Chapter 1

Neutron beta decay

The weak interaction is one of the four fundamental interactions of nature. Still, its first well established theory was not formulated before 1934. Nowadays we refer to the electroweak interaction since it has been discovered that the electromagnetic and weak interactions can be described within a unified theory. The weak interaction acts between both, leptons and quarks, and is the only interaction capable of changing flavor. To date, bound states for this interaction have never been observed. Due to the large mass of the weak interaction's bosons Z and $W^{\pm}$ (about 90 GeV/c^2), the range of the interaction is limited to 10^{-3} fm, about 1000 times smaller than the diameter of an atomic nucleus.

The electron neutrino angular correlation coefficient a is involved in several tests of the Standard Model of particle physics. In order to understand its implications for the theory, a detailed description of the theory of the beta decay is given in the first half of this Chapter. It starts with an historical overview of the neutron beta decay theories, from the Fermi formulation to the Standard Model, discussing the analogy between weak interaction and electromagnetism, the parity violation evidence, the $V - A$ theory and the CKM matrix. Hypotheses in which the Standard Model symmetries are based, are given afterwards: the absence of second class currents, the conserved vector current, and the partially conserved axial current. Finally, two formulations of physics beyond the Standard Model are presented.

In the second half of the Chapter are presented the observables in the free neutron decay with which the Standard Model can be tested. Special emphasis is placed on the angular correlation a and on the dependence of the a value on the proton spectrum shape, since it is measured with the aSPECT spectrometer. An overview of the status of the several Standard Model tests in which the coefficient a is involved is also given. The Chapter concludes with a summary of previous experiments measuring a.

1.1 From Fermi formulation to the Standard Model

The first attempt in developing a beta decay theory was carried out in the thirties of the last century by Enrico Fermi [Fer34] who, with good intuition, used a formulation in close analogy with the quantum theory of electromagnetic interactions. The Feynman diagram of the interaction of an electron with the electromagnetic field is shown in Fig. 1.1. The coupling between the electron and photon is expressed as a contraction of two 4-vectors by the following Hamiltonian density [Bjo63]:

$$\mathcal{H} = e j_\mu^{em} \cdot A^\mu \tag{1.1}$$

where $j_\mu^{em} = \bar{\Psi}_e \gamma_\mu \Psi_e$ is the electromagnetic current density (with Ψ_e representing the electron spinor field function and $\bar{\Psi}_e$ the corresponding adjoint function). A^μ is the 4-vector potential of the electromagnetic field. The strength of the electromagnetic interaction is characterized by the coupling constant e, the electric charge.

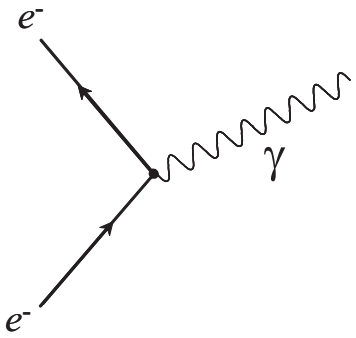

Figure 1.1: Feynman diagram describing the electron-photon vertex.

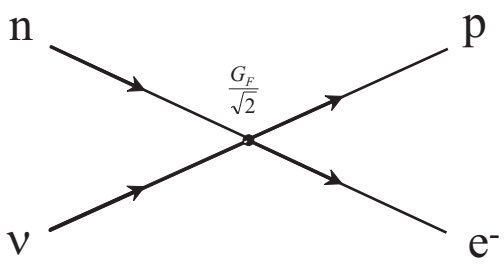

Figure 1.2: Point-like interaction of the neutron beta decay

The transformation terms used to describe weak interactions by analogy to the electromagnetic interaction theory are the following[1]:

$$e \rightarrow \frac{G_F}{\sqrt{2}} \tag{1.2}$$

$$j_\mu^{em} \rightarrow J_\mu^{had} = \bar{\Psi}_p \gamma_\mu \Psi_n \tag{1.3}$$

$$A^\mu \rightarrow J_{lep}^\mu = \bar{\Psi}_e \gamma^\mu \Psi_{\bar{\nu}} \tag{1.4}$$

According to the electromagnetic interaction model, the Fermi theory assumes a point-like interaction between the four fermions that take part in beta decay, but without

[1]The 4-component quantity Ψ is a Dirac spinor and describes a spin 1/2 particle. Following the *Bjorken and Drell* convention [Bjo63], for relativistic spin 1/2 particles, the Dirac matrices $\gamma^0, \gamma^1, \gamma^2, \gamma^3$ are defined by:

$$\gamma^0 = \begin{pmatrix} \mathbf{I} & 0 \\ 0 & \mathbf{-I} \end{pmatrix}, \quad \vec{\gamma} = \begin{pmatrix} 0 & \vec{\sigma} \\ -\vec{\sigma} & 0 \end{pmatrix}, \quad \text{and } \gamma^5 = i\gamma^0\gamma^1\gamma^2\gamma^3$$

the intervention of a propagator[2] (see Fig. 1.2). In Fermi's model an electron-neutrino (leptonic) current plays the role of the 4-vector potential and a hadronic current the role of the electromagnetic current. Both currents are of vector type, as it is seen in Eqs. 1.3 and 1.4. The electric charge e is replaced by the Fermi coupling constant $\frac{G_F}{(\hbar c)^3} = 1.16637(1) \times 10^{-5}\ GeV^{-2}$, which is determined from muon decays [Rit99] [Ams08].

Then, the Hamiltonian density (analog to Eq. 1.1) that describes the beta decay process (known as current-current interaction) is given by:

$$\mathcal{H} = \frac{G_F}{\sqrt{2}} J_\mu^\dagger \cdot J^\mu + h.c. \tag{1.5}$$

where the current J_μ comprises a hadronic and a leptonic contribution,

$$J_\mu = J_\mu^{had} + J_\mu^{lep} \tag{1.6}$$

Fermi's Hamiltonian (Eq. 1.5) gives a very good account of many observed characteristics of the β-decay process in first-order perturbation theory. However, as Fermi already hinted, it exists a more general way to construct a β-decay Hamiltonian considering interactions with different geometric forms in addition to the vector interaction[3].

The most general form of the Hamiltonian contains all possible interaction terms which accomplish invariance under Lorentz-, parity- and time-reversal transformation, and contain linear coupling operators without derivatives. Doing so, following *Severijns et al.* [Sev06], a more general Hamiltonian density of beta decay reads[4]:

$$\mathcal{H} = \sum_i (C_i \bar{\Psi}_p O_i \Psi_n) \cdot (\bar{\Psi}_e O_i \Psi_{\bar{\nu}}) + h.c. \tag{1.7}$$

where the operators O_i represent the 4×4 matrices[5] which create the possible current-current interactions:

---

[2]The propagator of the beta decay due to the W-boson exchange is discussed in Section 1.1.3

[3]One, for instance, may equally well construct a weak interaction by coupling the two axial-vector currents $\bar{\Psi}_p \gamma_\mu \gamma_5 \Psi_n$ and $\bar{\Psi}_e \gamma_\mu \gamma_5 \Psi_\nu$ as proposed by Gamow and Teller [Gam36].

[4]The convention used in *Severijns et al.* for the γ matrices follows the convention used by *Lee and Yang* [Lee56] and *Jackson, Treiman and Wyld* [Jac57]. This convention differs from the one used so far and defined by *Bjorken and Drell* [Bjo63]. In particular, the signs of γ_5 are opposite in the two representations.

[5]I, γ_μ, σ_t, -i$\gamma_\mu\gamma_5$ and γ_5 are the 4×4 matrices that transform as Scalar, Vector, Tensor, Axial-vector and Pseudo-scalar respectively, with $\sigma_t = \frac{\sigma_{\mu\nu}}{\sqrt{2}} = -\frac{i}{2}(\gamma_\mu\gamma_\nu - \gamma_\nu\gamma_\mu)$.

$\bar{\Psi}\Psi$	Scalar (S)
$\bar{\Psi}\gamma_\mu\Psi$	Vector (V)
$\bar{\Psi}\sigma_t\Psi$	Tensor (T)
-i$\bar{\Psi}\gamma_\mu\gamma_5\Psi$	Axial-vector (A)
$\bar{\Psi}\gamma_5\Psi$	Pseudo-scalar (P)

The coupling constants C_i define the relative strength of the interactions and can only be determined experimentally. It is not possible to derive a unique interaction from theoretical arguments alone. From the several alternative interactions, experiments must select the one realized in nature.
In β-decay it is appropriate to use the nonrelativistic limit for the nucleons since the initial nucleon is nonrelativistic and the momentum transferred to the leptons is typically very small. In this limit, the following nuclear spin selection rules for allowed beta transitions can be established (see also Fig. **??**):

ΔJ = 0	Fermi decays (Scalar and Vector couplings)
ΔJ = 0,1 (but no 0 $\rightarrow$ 0)	Gamow-Teller decays (Axial-vector and Tensor couplings)

In this selection, the scalar and vector couplings contribute to the no-spin-change transitions ($\Delta J = 0$) called Fermi transitions. The axial-vector and tensor couplings contribute to the so called Gamow-Teller transitions and are the only ones that involve spin-change transitions ($\Delta J = 1$). In lowest order there is no contribution of pseudoscalar coupling.

Experimentally both, pure Fermi transitions, for instance $^{14}\mathrm{O} \rightarrow {}^{14}\mathrm{N} + e^+ + \nu_e$, and Gamow-Teller transitions, for instance $^6\mathrm{He} \rightarrow {}^6\mathrm{Li} + e^- + \bar{\nu}_e$, are observed. However, most transitions are mixtures, like the neutron decay.

1.1.1 Parity violation and V-A theory

The discovery of parity violation in beta decay[6] [Wu57] [Gar57] showed that the Hamiltonian of beta decay is not necessarily invariant under space inversion and must be either scalar or pseudo-scalar. In the experiment of Wu and her collaborators at the National Bureau of Standards a clear anisotropy was observed in the direction of emission of decay electrons from the radioactive Cobalt 60 isotope, kept at low temperature with their spins aligned along the direction of a strong magnetic field. This result showed that electrons

[6]First postulated by Lee and Yang [Lee56].

are preferentially emitted in a direction opposite to that of the nuclear spin. For Eq. 1.7 this fact implies that there may also exist pseudo-scalar contributions of the form $(\bar{\Psi}_p O_j \Psi_n)(\bar{\Psi}_e O_j \gamma_5 \Psi_{\bar{\nu}})$ in the interaction. Adding these terms with coupling constants C_i', the Hamiltonian density in beta decay takes the form [Sev06]:

$$\mathcal{H} = \sum_i (\bar{\Psi}_p O_i \Psi_n) \cdot (\bar{\Psi}_e O_i (C_i + C_i' \gamma_5) \Psi_{\bar{\nu}}) + h.c. \tag{1.8}$$

Experimentally, parity violation has been found to be maximal. This means, the helicity[7] of electron and neutrino has the same sign for V and A interactions and opposite signs for S, T and P interactions. In other words, if weak interactions violate the parity symmetry, Fermi's V-formalism has to be modified. For the case of a V-A interaction, the beta decay would produce *left-handed* neutrinos; if the interaction is S-T, the neutrinos would all be *right-handed* particles.

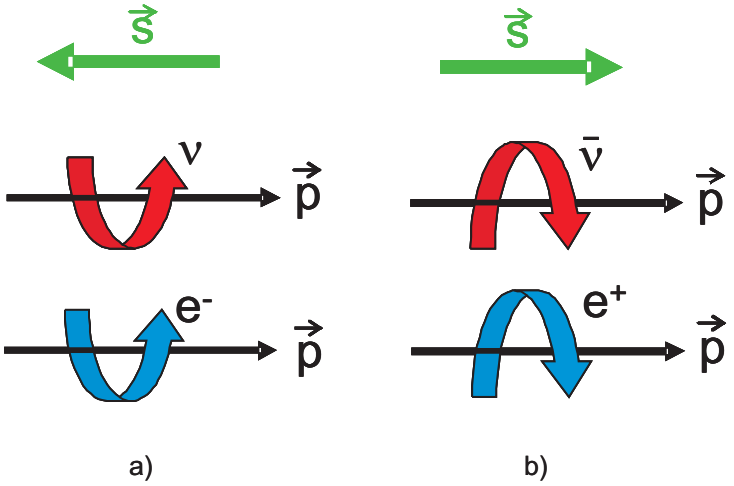

Figure 1.3: In the V-A theory parity is violated. a) electron and neutrino are *left-handed* particles. b) antineutrino and positron are *right-handed* particles.

The experimental evidence that electron and neutrino are left-handed resolved all doubts [Gol58]. As it is shown in Fig. 1.3, the spins of electron and neutrino emitted in beta decay are aligned antiparallel to their momentum and have negative helicity, whereas the spins of the positron and antineutrino are aligned parallel to their momentum, having positive helicity.

These experimental facts are theoretically described in the Feynman-Gell-Mann[8] scheme [Fey58], the so-called V-A theory, which implies not only that in beta decay parity is violated but also that charge conjugation invariance fails. Under charge conjugation, particles are transformed to anti-particles but spins and momenta are left unchanged. Accordingly, charge conjugation is violated if a process and the corresponding one in which particles are replaced by anti-particles do not occur with the same probability. This implies that the scalar and tensor couplings are consistent with zero and that beta decay

[7]The helicity is the projection of the spin $\vec{S}$ onto the direction of the momentum $\vec{p}$ of a particle.

[8]This theory was first proposed (although not first published) by Sudarshan and Marshak [Sud58].

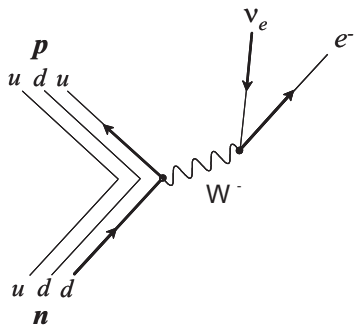

Figure 1.4: Feynman diagram describing the neutron decay in the standard model. A d quark transforms into a u quark via W^- boson exchange.

is a combination of vector (V) and axial-vector (A) couplings, with $C_i = C_i'$. With these results, Eq. 1.8 is rewritten as [Sev06]:

$$\mathcal{H} = \bar{\Psi}_e \gamma_\mu C_V (1+\gamma_5) \Psi_{\bar{\nu}} \bar{\Psi}_p \gamma_\mu \Psi_n - \bar{\Psi}_e \gamma_\mu \gamma_5 C_A (1+\gamma_5) \Psi_{\bar{\nu}} \bar{\Psi}_p \gamma_\mu \gamma_5 \Psi_n + h.c. \tag{1.9}$$

In the standard model:

$$C_A = G_F \frac{V_{ud}}{\sqrt{2}} g_A, \qquad C_V = G_F \frac{V_{ud}}{\sqrt{2}} g_V \tag{1.10}$$

where g_A and g_V are the values of hadronic vector and axial-vector form factors in the limit of zero-momentum transfer. V_{ud} is the ud-matrix element of the Cabibbo-Kobayashi-Maskawa matrix (see Section 1.1.2).

The ratio between the axial-vector and vector coupling constants is known as λ :

$$\lambda = \frac{C_A}{C_V} \tag{1.11}$$

The vector coupling constant C_V corresponds to Fermi decays and the axial-vector coupling constant C_A to Gamow-Teller decays. Neutron beta decay is a "mixed" transition, that is, it implies both, Fermi and Gamow-Teller contributions.

Eq. 1.9 contains a leptonic and a hadronic current of the V-A form, able to describe purely leptonic, purely hadronic and mixed weak decays. Since all these processes can be described with one coupling constant G_F, the universality of weak interactions seems to be proved.

1.1.2 CKM matrix

In the quark model of the weak interaction, nucleons are not fundamental particles but composed of three quarks. This means, neutron beta decay occurs because of the quark transformation $d \rightarrow u$. In this decay a flavor exchange is produced within quarks of the

same generation[9]. However, weak decays where a strange quark transforms into an up quark have been also observed. Examples of such transitions are $K^+ \rightarrow \mu^+\nu$, $\Delta^0 \rightarrow p\pi^-$ or $\Sigma^- \rightarrow ne^-\bar{\nu}$. Due to the fact that in weak decays quarks from different families can interact, it becomes necessary to consider weak quark eigenstates different from the mass eigenstates ones. Instead, they are a linear combination of the mass eigenstates of the quarks from all three generations with the same charge [Cab63] [Kob73]. The corresponding correlation of the weak eigenstates of the quarks to their mass eigenstates is done by the CKM matrix:

$$\begin{pmatrix} d' \\ s' \\ b' \end{pmatrix} = \begin{pmatrix} V_{ud} & V_{us} & V_{ub} \\ V_{cd} & V_{cs} & V_{cb} \\ V_{td} & V_{ts} & V_{tb} \end{pmatrix} \begin{pmatrix} d \\ s \\ b \end{pmatrix} \tag{1.12}$$

where the primed parameters correspond to the weak eigenstates of the quarks and the unprimed ones to their mass eigenstates. The CKM matrix is predicted to be unitary since it plays the role of a rotation matrix. Its deviation from unitarity would point to other physic models beyond the Standard Model (see references [Dub91] [Byr95] [Sev06] [Abe08]). Up to date, the most precise unitarity test comprises the sum of the square of the matrix elements from the first row, which should be equal to one:

$$\sum_i |V_{ui}|^2 = |V_{ud}|^2 + |V_{us}|^2 + |V_{ub}|^2 = 1 \tag{1.13}$$

The transition from one quark q to another quark q' is proportional to $|V_{qq'}|^2$. Assuming unitarity, the nine elements of the CKM matrix can be expressed in terms of four real parameters, namely three real angles and a phase. However, for the *up* and *down* quarks involved in beta decay, heavier quarks do not contribute in lowest order, having only one single mixing parameter:

$$d' \simeq V_{ud}d = \cos\theta_C d \tag{1.14}$$

where θ_C is the Cabibbo angle.

Thus, the correct V-A Hamiltonian describing the neutron beta decay process includes the matrix element V_{ud}, which gives the strength of the $u \leftrightarrow d$ flavor-changing in this decay:

$$\mathcal{H} = \frac{G_F}{\sqrt{2}} V_{ud} g_V (\bar{\Psi}_e \gamma_\mu (1 - \lambda\gamma_5)\Psi_{\bar{\nu}}) \cdot (\bar{\Psi}_u \gamma_\mu (1 + \gamma_5)\Psi_d) + h.c. \tag{1.15}$$

[9]There exist three families of quarks, each one containing two quark flavors:

$$\begin{pmatrix} u \\ d \end{pmatrix}, \begin{pmatrix} c \\ s \end{pmatrix}, \begin{pmatrix} t \\ b \end{pmatrix}$$

1.1.3 The Standard Model

At this point, the theory of weak interactions is able to provide an excellent phenomenological statement about the observed charged weak interactions within first-order perturbation theory. Nevertheless, it turns out to be a generalized version of the Fermi theory, being very successful at a certain level, but with big difficulties to overcome the divergences encountered in higher order perturbation theory. This makes the theory presented so far to be not re-normalizable.

The renormalization problem is solved with the so-called Standard Model, a theory which unifies the weak and the electromagnetic interactions [Gla61] [Sal68] [Wei67]. This model is based on quantum electrodynamics theory, defined mainly by two fundamental principles: it is a *local gauge invariant* theory with *spontaneous symmetry breaking*[10]. Now the interaction is not considered point-like anymore. Instead, the Standard Model postulates that the interaction of quarks and leptons in beta decay is mediated by the exchange of vector bosons $W^{\pm}$ and Z^0 (intermediate bosons), which are very massive[11] as a result of the short range of the weak interaction.

Intermediate bosons are *virtual* particles. They are not directly observable, but only their effect on the process can be observed. Calculations based on Feynman diagrams are used to predict the rate of the process.

In analogy to QED, the interaction via boson exchange with a mass M introduces a propagator term into the Hamiltonian of the form:

$$\frac{1}{Q^2 + M^2} \tag{1.16}$$

where Q is the momentum transfer and M the mass of the intermediate boson. If the momentum transfer is small compared to the boson mass the propagator can be considered to be constant. But it falls as $\frac{1}{Q^2}$ at very high momentum transfer. The uncertainty principle limits the range of force carried by the boson to a distance of about 10^{-3} fm due to its considerably large mass. This explains why the point-like interaction assumption applied in the classic theory is a good approximation in the limit of low momentum transfer.

In the Standard Model the exchange bosons are assumed to couple only to left-handed fermions and right-handed anti-fermions. However, there is no fundamental explanation of this parity violation in the model, the assumption is rather based on the experimental evidence that charged weak currents are of the V-A form.

As a consequence of the hypothesis that weak interaction is mediated by a vector boson analogous to the photon, the current-current interaction of (Eq. 1.15) is replaced by

[10] A mechanism for imparting mass to the intermediate bosons.

[11] $M_{W^{\pm}} = 80.403(29)$ GeV and $M_{Z^0} = 91.1876(21)$ GeV.

$$\mathcal{H} = -\frac{g}{2\sqrt{2}}(J_{\mu}^{weak} W_{\mu}) \tag{1.17}$$

where W_μ plays a similar role like A_μ in the electromagnetic interaction and J_μ^{weak} is the weak current which comprises of a leptonic and a hadronic part. The coupling constant g is given in terms of the Fermi coupling constant G_F by the relation:

$$\frac{g^2}{8M_W^2} = \frac{G_F}{\sqrt{2}} \tag{1.18}$$

However, electromagnetic and weak interactions have differences. First, electromagnetic forces are long range since the photon is massless whereas weak forces are short range because their intermediate bosons are very massive. Second, we can find charged intermediate bosons but the photon is always uncharged. To overcome all these differences, in the Standard Model is assumed that intermediate bosons come in three charge states; $W_\mu^{\pm}$ for the normal charged currents and W_μ^0 for the neutral current.

In the renormalized gauge theory of electroweak interactions there are four gauge vector particles corresponding to the group $SU(2) \times U(1)$ of gauge transformations: a weak iso-triplet $W_\mu^+ W_\mu^0 W_\mu^-$ and a weak iso-singlet B_μ^0. The neutral members W_μ^0 and B_μ^0 mix to produce the photon A_μ and the neutral vector boson Z_μ^0 mediates the weak neutral currents:

$$\begin{aligned} A_\mu &= W_\mu^0 \sin\Theta_W + B_\mu^0 \cos\Theta_W \\ Z_\mu^0 &= W_\mu^0 \cos\Theta_W - B_\mu^0 \sin\Theta_W \end{aligned} \tag{1.19}$$

where Θ_W is the Weinberg angle (or weak mixing angle), defined by:

$$\tan\Theta_W = \frac{g}{g'} \tag{1.20}$$

where g and g' are the couplings of the weak current to the triplet and singlet fields respectively. The value of Θ_W varies as a function of the momentum transfer, Q, at which it is measured[12].

However, in low energy processes such as neutron decay, non-local effects associated to the exchange of massive vector bosons are not observable. So, the four-fermion point-like approximation may be used.

[12] $\sin^2\Theta_W(Q = M_{Z^0}) = 0.23119(14)$[Ams08].

1.2 Symmetries

The symmetry structure of the electroweak theory is based on three important hypotheses: the absence of Second Class Currents (SCC), the Conserved Vector Current (CVC) and the Partially Conserved Axial Current (PCAC). All three hypothesis provide additional tests of the Standard Model in nuclear beta decay. A definition of these hypotheses is given in this section, while a further discussion of experimental tests can be found in Section 1.5.

1.2.1 Induced weak currents

Leptons are point-like particles and their leptonic current can be written in the simple form:

$$J_\mu^{lep} = \bar{\Psi}_e \gamma_\mu (1+\gamma_5) \Psi_{\bar{\nu}} \tag{1.21}$$

However, nucleons are extended objects and therefore structure effects must be included in the hadronic current when the precision of the measurements reaches a level below 10^{-2}. The use of form factors permit to describe nucleons by their spins and momenta including all the internal structure dependent effects. Thus, the general form of the hadronic current including all terms that transform as vector or axial-vector under Lorentz transformations is given by [Sev06],

$$J_\mu^{had} = \bar{\Psi}_p (V_\mu + A_\mu) \Psi_n \tag{1.22}$$

with

$$\bar{\Psi}_p V_\mu \Psi_n = \bar{\Psi}_p \Big[g_V \gamma_\mu + \frac{i}{m_{e^-}} g_S q_\mu + g_{WM} \frac{1}{2M} \sigma_{\mu\nu} q_\nu \Big] \Psi_n \tag{1.23}$$

$$\bar{\Psi}_p A_\mu \Psi_n = \bar{\Psi}_p \Big[g_A \gamma_\mu \gamma_5 + \frac{i}{m_{e^-}} g_P q_\mu \gamma_5 + g_T \frac{1}{2M} \sigma_{\mu\nu} q_\nu \gamma_5 \Big] \Psi_n \tag{1.24}$$

where $q_\mu = (p_i - p_f)_\mu$ is the four-momentum transfer and M the average of the initial and final nucleon mass. The form factors g_i are arbitrary functions of the Lorentz scalar q^2. In the limit $q^2 \to 0$ the form factors g_V and g_A are identified as the conventional vector and axial vector coupling constants. The other terms g_S, g_P, g_{WM} and g_T are **induced form factors**, which are respectively referred to as *induced scalar*, *induced pseudo-scalar*,*weak magnetism* and *induced tensor couplings*.

By means of symmetry arguments these form factors can be restricted. A **G-parity** transformation is defined by a charge conjugation operation followed by a rotation by π around the y axis in isospin space:

$$G = C e^{i\pi I_2} \tag{1.25}$$

where I_2 is the operator associated with the second component of the isospin I.

The **isospin** I and its third component I_3 are quantum numbers related to the strong interaction. Historically they were introduced in order to treat the neutron and proton as charge states of the same particle, the nucleon, since they have nearly equal masses. So, in absence of an electromagnetic field the nucleon has two degenerate isospin states. By convention the proton has $I_3 = +\frac{1}{2}$ and the neutron $I_3 = -\frac{1}{2}$. The isospin is a SU(2) symmetry which satisfies the algebra of the ordinary spin. I has multiplicity $2I + 1$ and I_3 indicates charge Q. The isospin generators satisfy:

$$[I_j, I_k] = \epsilon_{jkl} I_l \tag{1.26}$$

and are denoted by $I_j \equiv \frac{1}{2}\tau_j$, where τ_j are the isospin version of the Pauli matrices:

$$\tau_1 = \begin{pmatrix} 0 & 1 \\ 1 & 0 \end{pmatrix}, \qquad \tau_2 = \begin{pmatrix} 0 & -i \\ i & 0 \end{pmatrix}, \qquad \tau_3 = \begin{pmatrix} 1 & 0 \\ 0 & -1 \end{pmatrix} \tag{1.27}$$

The charge of a particle is related to its hypercharge Y and I_3 by:

$$Q = I_3 + \frac{Y}{2} \tag{1.28}$$

The transformation properties of the terms in the currents of Eqs. 1.23 and 1.24 under the G operation can determine if such terms are dynamically possible. According to [Wei58], the weak magnetism and the induced pseudo-scalar are classified as *first class currents*. They are defined by having vector currents with G parity +1 and axial currents with G parity −1. Induced scalar and induced tensor terms are *second class currents* (SCC), which have opposite parities. Thus, the requirement of the electroweak theory that the hadronic V and A currents have a definite G parity implies that *second class currents* can not exist, so $g_S = 0$ and $g_T = 0$. Indeed, experimental tests performed so far indicate that SCC are consistent with zero [Sev06].

1.2.2 Conserved Vector Current (CVC)

The Conserved Vector Current hypothesis (CVC) assumes the weak vector current to be conserved with a universal coupling constant, in analogy to the electromagnetic vector current. This hypothesis can be formulated using isospin formalism, expressing the electromagnetic current J^{em}_μ and the weak vector current V_μ as:

$$J^{em}_\mu = \frac{1}{2}\bar{\Psi}\gamma_\mu(I + \tau_3)\Psi \tag{1.29}$$

$$V_\mu = \frac{1}{2}\bar{\Psi}\gamma_\mu(\tau_1 + i\tau_2)\Psi \tag{1.30}$$

J_μ^{em} consists of an iso-scalar and an iso-vector part[13]. The iso-scalar part satisfies the current conservation requirement:

$$\partial_\mu(\bar{\Psi}_f\gamma_\mu\Psi_i) = 0 \tag{1.31}$$

whereas the iso-vector part of the electromagnetic and weak vector currents can be written as follows:

$$J_\mu^{em}(\text{iso-vector}) = \frac{1}{2}\bar{\Psi}\gamma_\mu\tau_3\Psi \tag{1.32}$$

$$V_\mu(\text{iso-vector}) = \frac{1}{2}\bar{\Psi}\gamma_\mu(\tau_1 + i\tau_2)\Psi \tag{1.33}$$

The CVC hypothesis assumes that these iso-vector currents are only different components of the same iso-vector current:

$$J_\mu^{em}(\text{iso-vector}) = \frac{1}{2}\bar{\Psi}\gamma_\mu\tau\Psi \tag{1.34}$$

An immediate consequence of the CVC hypothesis is that $C_V = 1$. Furthermore it implies that $g_S = 0$ and predicts the weak magnetism term to be $g_{WM} = \mu^p - \mu^n \sim 3.7$, where μ^p and μ^n are the proton and neutron magnetic moments, respectively.

1.2.3 Partially Conserved Axial Current (PCAC)

The axial-vector current is not a conserved current. This means, the value of C_A at the pure quark coupling level differs from unity. $|C_A|$ is about 1.27 in free neutron decay but smaller in nuclear decays due to screening.

One indication that the axial-vector current is not conserved is the decay of the pion $\pi^\pm$, which is purely axial. The derivative of the axial current, $\partial_\mu A^\mu$, is hence non-zero but since the pion is light on the hadronic mass scale, it can be considered small. Therefore, in the limit of a massless pion, the axial vector current can be considered conserved. Such approximation is called the Partially Conserved Axial Current hypothesis (PCAC) [Nam60] [Gel60].

One of the consequences of PCAC is the Goldberger-Treiman expression[14], which at $q^2 = 0$ relates the pion decay parameters with the axial vector coupling constant as follows:

$$g_{\pi NN}(0)F_\pi = m_N C_A \tag{1.35}$$

[13]The terms *iso-scalar* and *iso-vector* refer, respectively, to scalar and vector transformation properties under the SU(2) group of isospin. The first is a singlet state with $I = 0$ and $I_3 = 0$, the second a triplet state with $I = 1$ and $I_3 = 1, 0, -1$

[14]In a more modern understanding, this relation is a consequence of the approximate chiral symmetry of the strong interaction.

where $g_{\pi NN}$ is the pion-nucleon coupling, F_π the pion decay constant and m_N the nucleon mass. For non-zero q^2 Eq. 1.35 leads to the Goldberger-Treiman expression which relates the induced pseudo-scalar form factor g_P and the axial vector coupling constant:

$$g_P(q^2) = \frac{2m_\mu m_N}{m_\pi^2 - q^2} C_A \tag{1.36}$$

where m_π is the charged pion mass and m_μ is the muon mass. However, the beta decay is not a useful source of information for testing Eq. 1.36, because the momentum transfer is very small. Instead, ordinary muon capture and radiative muon capture are the main sources used to determine g_P and consequently verify the momentum dependence of $g_{\pi NN}$ (see [Gor04] for more information).

1.3 Extensions of the Standard Model

??

Despite the big success of the V-A theory, there exist alternative formulations as extensions of the Standard Model. Their appearance is motivated by open questions which are not explained by the V-A theory, like the experimental evidence of neutrino oscillations or the origin of parity violation. Here we will consider only two extensions of the Standard Model whose contributions appear already at the tree-level of Feynman diagrams, i.e., at 0^{th} order perturbation theory. In Section 1.5 a discussion about experimental sensitivities of the angular correlation coefficient a on both extension models is given.

1.3.1 Right handed currents

The assumption of a left-right symmetric universe after the big bang is included in most grand unified theories. Even though the Standard Model (valid at much lower energies) has incorporated the fact of maximal parity violation, it does not provide an understanding of the origin of the left-right asymmetry in the universe nowadays.

Therefore, left-right symmetric models are attractive extensions of the Standard Model, because they may provide a framework for the origin of parity violation in the weak interaction [Pat74] [Moh75]. The simplest models are based on the gauge group $SU(2)_L \times SU(2)_R \times U(1)$.

In these theories, parity violation is explained as a consequence of spontaneous symmetry breaking in a transition to lower energies. For that purpose, additional gauge bosons $W_R^{\pm}$ with mass m_{W_R} are introduced. According to these models, below energies of about m_{W_R}, the weak interaction is mediated by the boson $W_L^{\pm}$ which is identified with the $W^{\pm}$ boson of the Standard Model. Then, in a similar way to the quark-mixing, the weak eigenstates of the $W_{L,R}$ bosons are given by a linear combination of the mass eigenstates $W_{1,2}$:

$$\begin{pmatrix} W_L \\ W_R \end{pmatrix} = \begin{pmatrix} \cos\zeta & \sin\zeta \\ -e^{i\omega}\sin\zeta & e^{i\omega}\cos\zeta \end{pmatrix} \begin{pmatrix} W_1 \\ W_2 \end{pmatrix}$$

where ζ is a mixing angle and ω a CP-violating phase. If $\zeta = 0$ and the W_R is infinitely heavy, the Standard Model is restored.

So far, no experimental evidence of right-handed currents has been observed. Limits on the mixing angle ζ and the mass parameter $\delta = (m_1/m_2)^2$ exists from μ-decay experiments. One expects W_R to be very massive, of about $m_{W_R} \approx 10^4$ GeV (see [Her01] and references therein).

1.3.2 Scalar and Tensor interactions

Some of the extensions of the Standard Model do not assume that the weak interaction is a pure V-A interaction and, hence, include all possible contributions: S,T,P,V,A. The more general form of the Hamiltonian in beta decay interactions is then given by Eq. 1.8, which can be splitted in three terms:

$$\mathcal{H} = \mathcal{H}_{V,A} + \mathcal{H}_{S,P} + \mathcal{H}_T \tag{1.37}$$

$\mathcal{H}_{V,A}$ contains the vector and axial-vector interactions, $\mathcal{H}_{S,P}$ the scalar and pseudo-scalar interactions, and $\mathcal{H}_T$ contains tensor interactions. The forms of $\mathcal{H}_{V,A}$, $\mathcal{H}_{S,P}$ and $\mathcal{H}_T$ can be found in detail in [Her01], although the pseudo-scalar contribution $\mathcal{H}_P$ is neglected since the pseudo-scalar current vanishes in the nonrelativistic approximation for nucleons.

Different approaches in terms of exotic couplings and maximal parity violation can be considered (see [Sev06]). We focus in the case where the contributions of Scalar and Tensor interactions are pure right-handed currents. This restricts the coupling constants of Eq. 1.8 with the following relations:

$$C_{V,A} = C'_{V,A} \qquad C_{S,T} = -C'_{S,T} \tag{1.38}$$

Scalar and tensor interactions are ruled out only to the level of about 5-10% of the V and A interactions. A recent analysis of experimental data from both neutron and nuclear beta decay experiments can be found in [Mos00] and [Sev06].

1.4 Observables in neutron decay

Fermi's golden rule gives the transition probability per unit time that a quantum mechanical process takes place. It is given by:

$$w_{i\to f} = \frac{2\pi}{\hbar} |\langle f| \mathcal{H}_{int} |i\rangle|^2 \rho(E) \tag{1.39}$$

where the matrix element $M_{fi} = \langle f| \mathcal{H}_{int} |i\rangle$ accounts for the strength of the interaction between the initial and the final state. The transition rate depends on how many final states are accessible to the system, given by the density of final states per energy interval:

$$\rho(E) = \frac{dn(E)}{dE} \tag{1.40}$$

dn(E) is the number of final states with energy between E and $E + dE$. A given transition is more likely to occur if there is a large number of accessible final states.

1.4.1 Energy Spectra

The final state of the free neutron decay is composed of three particles. Since the masses of the electron and antineutrino are small compared with the energy involved in the decay, the process has to be treated relativistically. However, the proton recoil energy can be neglected and the total decay energy $E_0 = E_e + E_{\bar{\nu}} = m_0c^2 + E_{kin,e} + E_{\bar{\nu}} \simeq 1.3$ MeV is shared among the electron and the antineutrino. The differential decay probability for a neutron decay with outcoming electron energy between E_e and $E_e + dE_e$ is then expressed as:

$$dw(E_e) = \frac{2\pi}{\hbar} |\langle f| \mathcal{H}_{int} |i\rangle|^2 \frac{d\rho(E_0, E_e)}{dE_e} dE_e \tag{1.41}$$

For a given phase space volume $d^3p_e d^3p_{\bar{\nu}}$, the final density of states is

$$d\rho_e = \frac{(4\pi)^2}{(2\pi\hbar)^6} E_e \sqrt{E_e^2 - m_e^2c^4} (E_0 - E_e)^2 dE_e \tag{1.42}$$

giving the electron energy distribution of the unpolarized neutron decay. This formula can be refined if we consider the Coulomb interaction between the outgoing proton and electron. Such interaction leads to a correction of the phase space factor of about 1%, which is specially important at low electron energies. This effect is accounted for multiplying $d\rho_e$ with the *Fermi function*:

$$F(Z, E) \simeq \frac{2\pi\eta}{1 - e^{-2\pi\eta}} \quad \text{with} \quad \eta = \pm\frac{Z\alpha}{v_e} \tag{1.43}$$

where v_e is the velocity of the electron in units of c and α is the fine-structure constant. For the free neutron decay, i.e. for $Z = 1$, the value of η is very small. Then, the electron spectrum with Coulomb interaction correction is

$$d\rho_e = \frac{(4\pi)^2}{(2\pi\hbar)^6} F(1, E_e) E_e \sqrt{E_e^2 - m_e^2 c^4} \cdot (E_0 - E_e)^2 dE_e \tag{1.44}$$

In Fig. 1.5, the shape of the energy spectrum of electrons from free neutron decay is shown.

Analogously to the electron spectrum we can infer the antineutrino spectrum from free neutron decay, which is plotted in Fig. 1.6:

$$d\rho_{\bar{\nu}} = \frac{(4\pi)^2}{(2\pi\hbar)^6} \sqrt{(E_0 - E_{\bar{\nu}})^2 - m_e^2 c^4} \cdot (E_0 - E_{\bar{\nu}}) E_{\bar{\nu}}^2 dE_{\bar{\nu}} \tag{1.45}$$

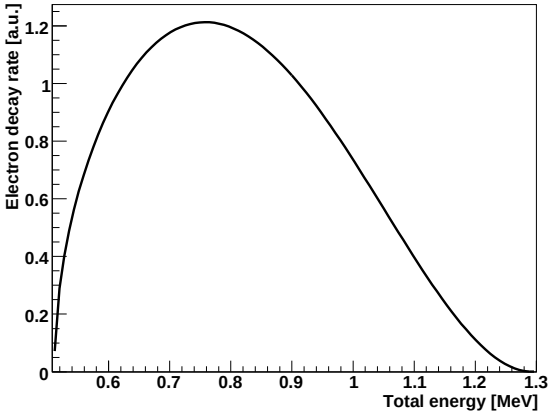

Figure 1.5: Electron spectrum from free neutron decay. Note that $E_e = m_0 c^2 + E_{kin,e}$.

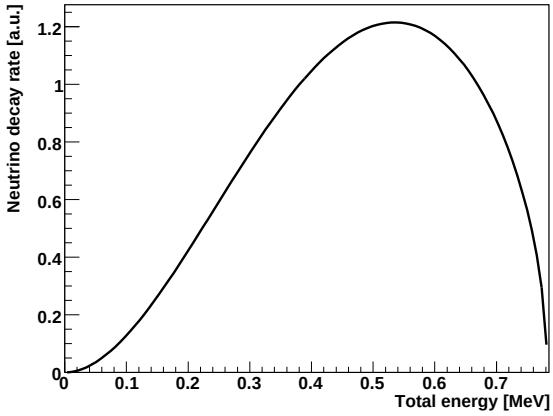

Figure 1.6: Antineutrino spectrum from free neutron decay.

1.4.2 Angular correlation coefficients

Taking into consideration the Hamiltonian derived in Eq. 1.15, the interaction matrix M_{fi} can be obtained as a function of the coupling constants g_V and g_A. Consequently, the differential decay probability of a polarized free neutron is calculated to be [Jac57]:

$$d\omega \propto G_F^2 |V_{ud}|^2 F(E)(g_V^2 + 3g_A^2)\left(1 + a\frac{\vec{p}_e \vec{p}_{\bar{\nu}}}{E E_{\bar{\nu}}} + b\frac{m_e}{E} + \langle \vec{\sigma}_n \rangle \left[A\frac{\vec{p}_e}{E} + B\frac{\vec{p}_{\bar{\nu}}}{E_{\bar{\nu}}} + D\frac{\vec{p}_e \times \vec{p}_{\bar{\nu}}}{E E_{\bar{\nu}}}\right]\right) dE d\Omega_e d\Omega_{\bar{\nu}} \tag{1.46}$$

where $\vec{p}_e$, $\vec{p}_{\bar{\nu}}$, E, $E_{\bar{\nu}}$ are the momentum and the energy of the electron and the antineutrino, respectively. The neutron spin direction is denoted by $\langle \vec{\sigma}_n \rangle$ and the respective solid angles by Ω_i. a, A, B and D are angular correlation coefficients and b the Fierz term.

In the $V - A$ theory these correlation coefficients are only functions of the weak interaction coupling constants g_A and g_V. Using the ratio $\lambda = \frac{C_A}{C_V}$, the correlation coefficients can be expressed as:

$$a = \frac{1-|\lambda|^2}{1+3|\lambda|^2}, \quad A = -2\frac{|\lambda|^2 + Re(\lambda)}{1+3|\lambda|^2}, \quad B = 2\frac{|\lambda|^2 - Re(\lambda)}{1+3|\lambda|^2}, \quad D = \frac{2Im(\lambda)}{1+3|\lambda|^2} \tag{1.47}$$

Please note that the sensitivity on λ is specially high for the angular correlation coefficients a and A, see Fig. 1.7. Since measurements of A and a provide completely independent access to λ values, their comparison provides a test of the $V-A$ theory [Glü95].

The coefficient b, or the Fierz interference term, contains mixed S/V, and A/T interference terms. Therefore, in the framework of the V-A theory, b equals zero. In addition, when time reversal invariance is assumed λ is real and the coefficient D vanishes. In this case, the following relations exist among a, A and B [Mos76]:

$$B = 1 + A - a \tag{1.48}$$

$$aB = A^2 + A \tag{1.49}$$

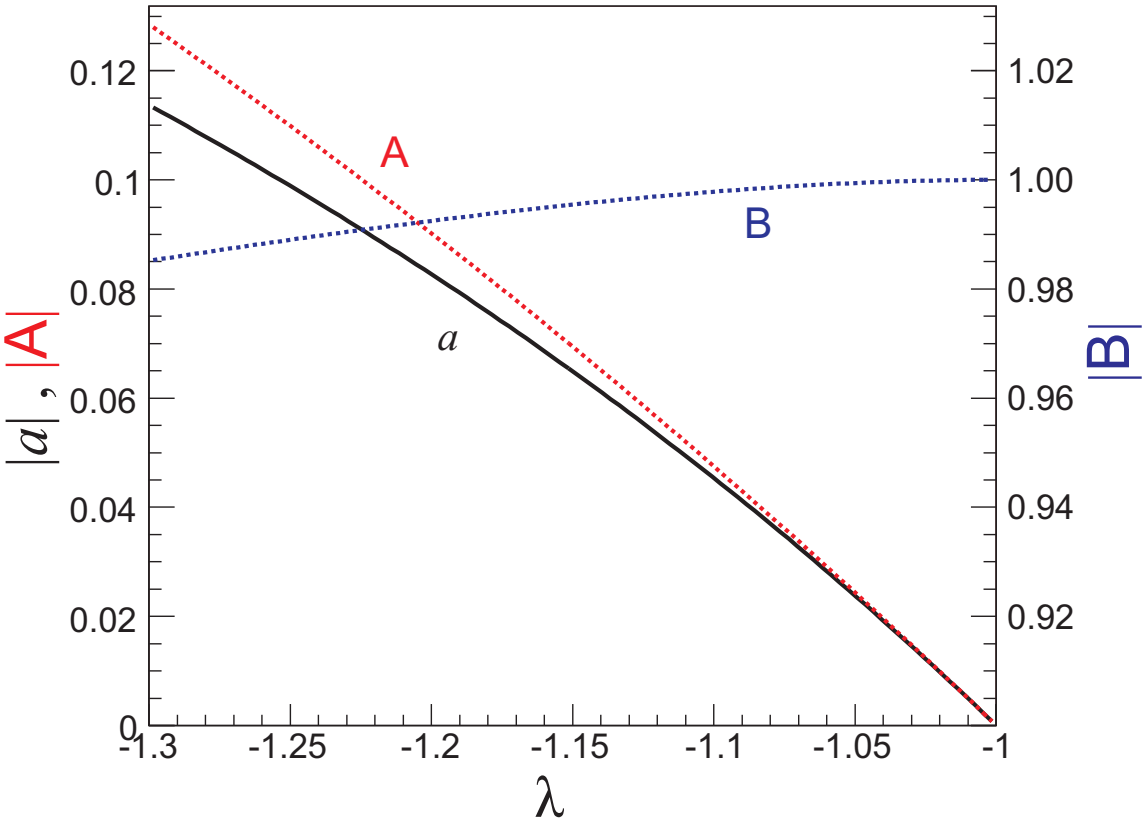

Figure 1.7: Angular correlation coefficients plotted as a function of λ.

1.4.3 Neutron Lifetime

Another observable of the free neutron decay is the neutron lifetime τ_n. It depends on λ and the matrix element V_{ud} as follows:

$$\tau_n = \frac{K}{|V_{ud}|^2 G_F^2 (1+3|\lambda|^2)(1+\Delta_R) f^R} \tag{1.50}$$

where f^R is the phase-space factor, K is a constant and the factor Δ_R is the nucleus-independent radiative correction. Apart from the Coulomb correction, also radiative corrections are involved in neutron decay. Radiative corrections take into account additional processes besides the W-boson exchange shown in Fig. 1.4, for instance the additional exchange of virtual particles or the coupling to real particles. One can distinguish between two types of radiative corrections: the *outer* and the *inner* ones. Inner (or model-dependent) radiative corrections are due to nucleon's structure, whereas outer (or model-independent) radiative corrections depend on the nucleon's charge and size and are described by higher order QED loop corrections. Unlike to the nuclear beta decay, in the free neutron decay no nuclear structure corrections have to be applied [Tow02].

It is possible to determine V_{ud} by combining two independent measurements: the neutron lifetime and any angular correlation coefficient sensitive to the parameter λ. Eq. 1.50 can be rewritten to derive V_{ud} [Ams08]:

$$|V_{ud}|^2 = \frac{4908.7(1.9) sec}{\tau_n (1+3\lambda^2)} \tag{1.51}$$

In section 1.5.1 a further discussion about the unitarity of the CKM matrix as a function of the input parameters λ and τ_n can be found.

1.4.4 The electron-antineutrino correlation coefficient

From Eq. 1.46, the differential transition probability dw for a fixed electron energy E_e in beta decay of unpolarized neutrons can be expressed as

$$dw \propto 1 + a\frac{\vec{p_e}\cdot\vec{p_\bar{\nu}}}{E_e E_\bar{\nu}} = 1 + a\frac{|\vec{p_e}||\vec{p_\bar{\nu}}|}{E_e E_\bar{\nu}} cos(\Theta_{\vec{p_e},\vec{p_\bar{\nu}}}) \tag{1.52}$$

where a is the angular correlation coefficient between the electron and antineutrino momenta, $\Theta_{\vec{p_e},\vec{p_\bar{\nu}}}$ is the angle between the electron and the antineutrino momenta, and $\vec{p}$ and E indicate the momenta and energies of both particles. The coefficient a indicates the preferred relative orientation of the electron and antineutrino momenta.

To estimate the range of possible values for a, one has to consider that the probability density in Eq. 1.52 is always positive and, since $\frac{|\vec{p_\bar{\nu}}|}{E_\bar{\nu}} \sim 1$, the following relation has to be fulfilled:

$$1 + a\frac{|\vec{p_e}|}{E_e} cos(\Theta_{\vec{p_e},\vec{p_\nu}}) > 0 \tag{1.53}$$

The inequation 1.53 has to hold for $0 \leq \frac{|\vec{p_e}|}{E_e} \leq 1$ and $-1 \leq cos(\Theta_{\vec{p_e},\vec{p_\nu}}) \leq 1$. Then, two extreme cases can be considered:

a) a is positive and $cos(\Theta_{\vec{p_e},\vec{p_\nu}}) = -1$:

$$a < \frac{E_e}{|\vec{p_e}|} \tag{1.54}$$

b) a is negative and $cos(\Theta_{\vec{p_e},\vec{p_\nu}}) = 1$:

$$a > -\frac{E_e}{|\vec{p_e}|} \tag{1.55}$$

From Eqs. 1.54 and 1.55 it is inferred that the value of a take values between $\pm\frac{E_e}{|\vec{p_e}|}$. The value of this fraction can be estimated from the relativistic energy-momentum equation, entering the maximum electron kinetic energy in free neutron decay ($\approx$ 780 keV), which gives $\frac{E_e}{|\vec{p_e}|} = \frac{1291}{1185}$. Consequently, in first approximation, the value of a is constrained between ± 1.089. If in nature there were no preferred configuration, a would be equal to zero.

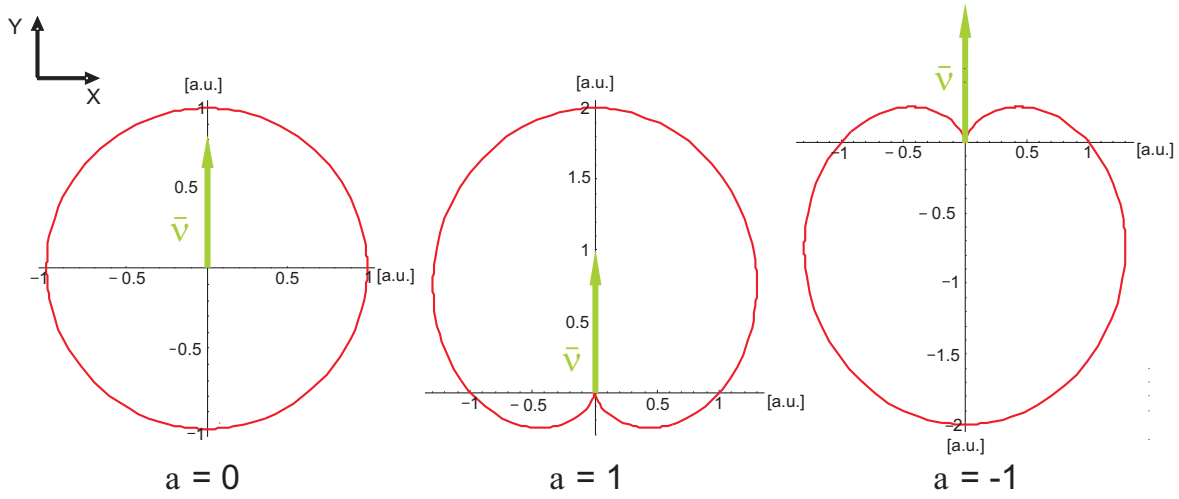

Figure 1.8: Angular dependence of the differential decay probability (in arbitrary units) of the free neutron decay for three different values of a. In the plot the direction of the antineutrino momentum is pointing upwards (green arrow) and the electron energy is fixed. The distance of each point of the red curve from the origin gives the probability $\sqrt{x^2+y^2}$ that in neutron decay, the antineutrino and electron momenta have an angle $\Theta_{\vec{p_e},\vec{p_\nu}}$. For $a = 0$, electron and antineutrino momenta have no preferred angle $\Theta_{\vec{p_e},\vec{p_\nu}}$. But for $a = 1$ and $a = -1$ parallel and antiparallel configurations have respectively higher probability to occur.

In Fig. 1.8 the angular dependence of the differential decay probability in the free neutron decay is plotted for different values of a. When fixing the direction of the antineutrino momentum, one can see that for $a = 1$ the probability density that the momenta of electron and antineutrino are parallel is higher than any other configuration. But for $a = -1$ it is more probable that electron and antineutrino have antiparallel momenta.

Free neutrons have three possible decay modes: one Fermi transition and two modes from Gamow-Teller transitions, see Fig. 1.9. In Fermi decays the produced leptons are in a spin singlet state (total spin is 0) and their decay probability is given by the coupling constant C_V. In Gamow-Teller decays the final lepton state is a triplet[15] (total lepton spin is 1) and are governed by the axial-vector coupling constant C_A.

From the spin state and the chirality of the leptons follows that in Fermi decays, electron and antineutrino have parallel momenta, implying $a = 1$. For the same reasons one Gamow-Teller transition has $a = 1$ and the other one has $a = -1$. Therefore, a measurement of a gives the relative strength between the coupling constants C_A and C_V since a depends on their ratio (Eq. 1.47). In the V-A theory, for a pure Fermi decay, a is 1; for a pure Gamow-Teller decay, it is $-\frac{1}{3}$ [Döh90].

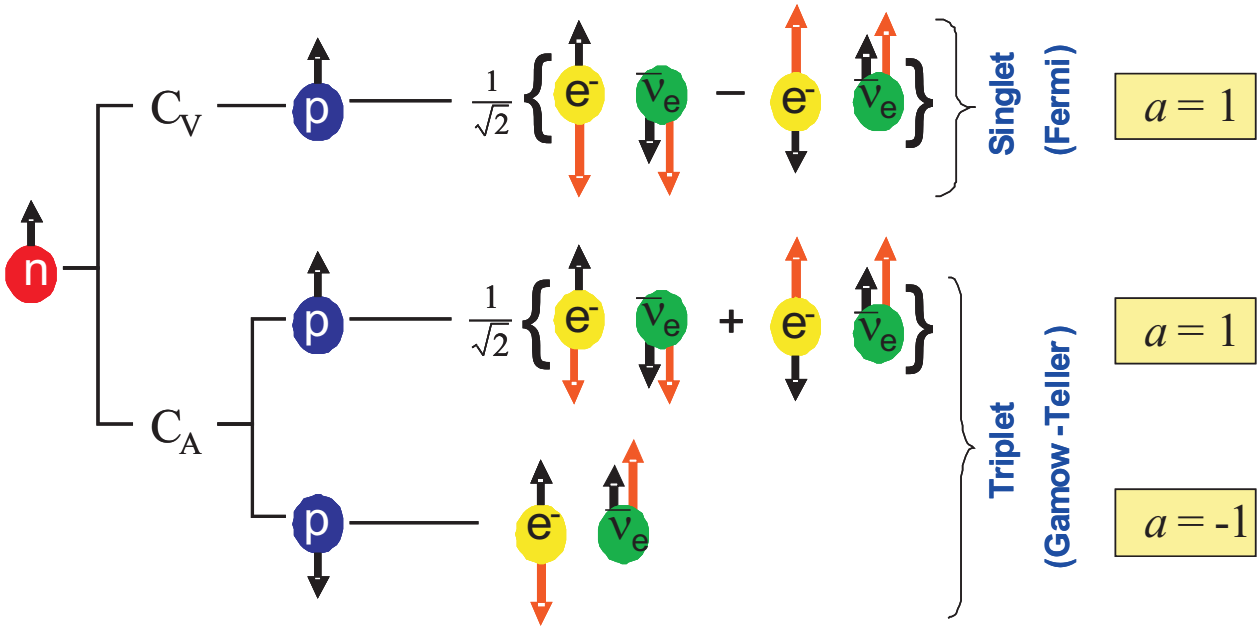

Figure 1.9: Fermi and Gamow-Teller decay modes of the free neutron and their dependence on the value of the coefficient a. Black and red arrows indicate the direction of the spin and momentum of the particles, respectively.

[15] Only two of the three triplet states are allowed. The third state corresponds to the spin z-component -1, which can not be created in the final lepton state.

1.4.5 Proton spectrum

In Ref. [Nac68], the differential proton energy spectrum from neutron beta decay has been calculated in a relativistic framework. Neglecting Coulomb and radiative corrections, Nachtmann's formula[16] for the differential proton energy spectrum as a function of the proton kinetic energy T, can be written as:

$$dw_p(T) = \frac{\Sigma\Delta^3 G_V^2}{2^4\pi^3(1+2\delta)}\Big(\frac{\sigma-x^2}{\sigma}\Big)^2\sqrt{1-\sigma}\Bigg\{\Big(1+\frac{x^2}{\sigma}-\sigma\Big)-\frac{1}{3}\Big(\frac{\sigma-x^2}{\sigma}\Big)(1-\sigma)+ \\ +\lambda^2\Bigg[\Big(1+\frac{x^2}{\sigma}+\sigma\Big)-\frac{1}{3}\Big(\frac{\sigma-x^2}{\sigma}\Big)(1-\sigma)\Bigg\}\Bigg]dT \quad (1.56)$$

where

$$\sigma = 1-\frac{2Tm_n}{\Delta^2}, \quad x=\frac{m_e}{\Delta}, \quad \Delta = m_n - m_p, \quad \Sigma = m_n + m_p, \quad \delta = \frac{\Delta}{\Sigma} \quad (1.57)$$

m_n, m_p and m_e are the masses of the neutron, proton and electron, respectively.

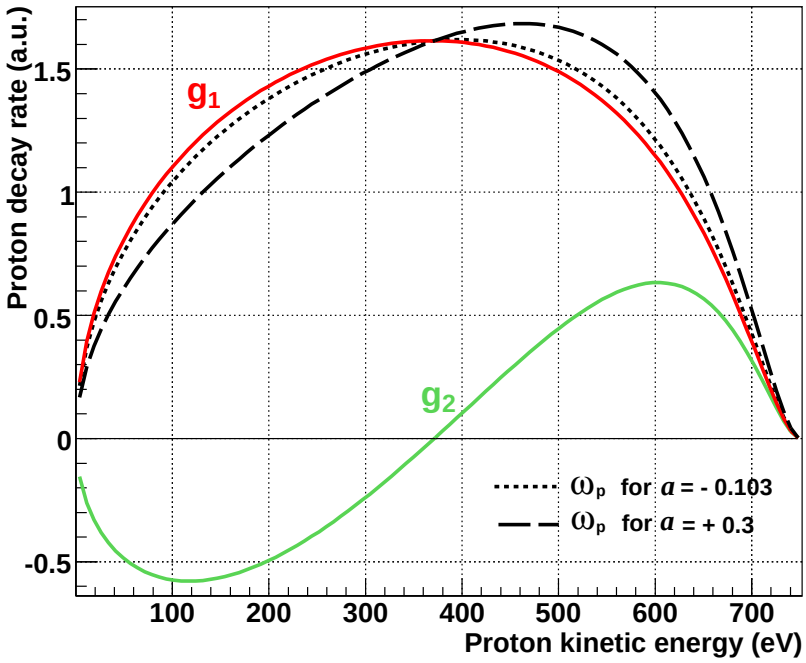

Figure 1.10: Representation of functions g_1 and g_2 (see Eqs. 1.59 and 1.60). Also, the proton decay rate $d\omega_p(T)$ is plotted for different values of a.

Eq. 1.56 can be parameterized as a function of the angular correlation coefficient a in the way:

[16] A sign error in this formula was found by C. Habeck [Hab97].

$$dw_p(T) \propto g_1(T) + a g_2(T) \tag{1.58}$$

where g_1 and g_2 are known functions of the kinetic energy of the proton, T. They are given by:

$$g_1 = \Big(\frac{\sigma - x^2}{\sigma}\Big)^2 \sqrt{1-\sigma}\left[4\Big(1 + \frac{x^2}{\sigma}\Big) - \frac{4}{3}\frac{\sigma - x^2}{\sigma}(1-\sigma)\right] \tag{1.59}$$

$$g_2 = \Big(\frac{\sigma - x^2}{\sigma}\Big)^2 \sqrt{1-\sigma}\left[4\Big(1 + \frac{x^2}{\sigma} - 2\sigma\Big) - \frac{4}{3}\frac{\sigma - x^2}{\sigma}(1-\sigma)\right] \tag{1.60}$$

Both functions are plotted in Fig. 1.10. Further, a comparison of the proton decay rate $d\omega_p$ for different values of a shows the influence of a over the proton spectra shape. A theoretical proton recoil spectrum $w_p(T)$ including recoil-order, Coulomb and model-independent radiative corrections, can be found in [Glü93].

1.5 Standard Model tests

1.5.1 CKM unitarity

The standard model of particle physics predicts the Cabibbo-Kobayashi-Maskawa matrix (CKM matrix) to be unitary (see Section 1.1.2 for more detail).

The possibility that the unitary test does not hold true on a 3-σ level has been a reality during the last two decades. For that reason the interest in testing the unitarity of the CKM matrix has increased, leading to an increment of new experimental data and more accurate theoretical corrections. The unitary consistency check in 2008 according to the Particle Data Group [Ams08] leads to:

$$V_{ud}^2 + V_{us}^2 + V_{ub}^2 = 0.9999(5)(9) \tag{1.61}$$

where the first error is the uncertainty from $|V_{ud}|^2$ and the second error is the uncertainty from $|V_{us}|^2$. The result is in good agreement with unitarity.

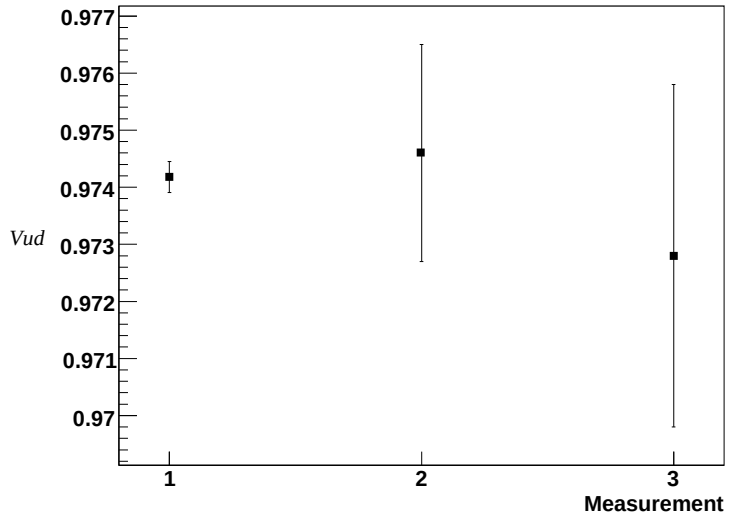

Figure 1.11: Recommended Particle Data Group $|V_{ud}|$ values [Ams08]. Measurement 1: obtained from: $0^+ \rightarrow 0^+$ superallowed Fermi beta decays. Measurement 2: obtained from neutron beta decays. Measurement 3: obtained from pion beta decays.

There are mainly three independent experimental methods from which the V_{ud} element can be deduced: superallowed $0^+ \rightarrow 0^+$ pure Fermi transitions, free neutron decay and pion beta decay. The element V_{us} is usually determined from charged and neutral kaon decays, hyperon decay and hadronic τ decay data. V_{ub} is obtained from B-meson decays although its value is so small that at the present level of precision it does not contribute to the unitarity test.

The highest weight within the unitary condition (see Eq. 1.13) falls on the element V_{ud}, so an accurate determination of it is most important. The values of V_{ud} derived by three different β-decay experiments are shown in Fig. 1.11. The averaged value obtained

for V_{ud} from superallowed Fermi decays (and recommended value by the PDG) is the most accurate. But its error is dominated by theoretical uncertainties due to nuclear Coulomb distortions and radiative corrections.

Experiments using the beta decay of the free neutron are an alternative experimental approach which allows a determination of V_{ud} free from the nuclear structure effects of superallowed beta decays. This kind of experiments (together with pion beta decay) have smaller theoretical uncertainties and although their accuracies are so far limited from the experimental side, may in the long term be a better way to obtain V_{ud}.

As it was seen in Eq. 1.51, one can determine V_{ud} by combining two independent measurements: the neutron lifetime and any angular correlation coefficient sensitive to the parameter λ.

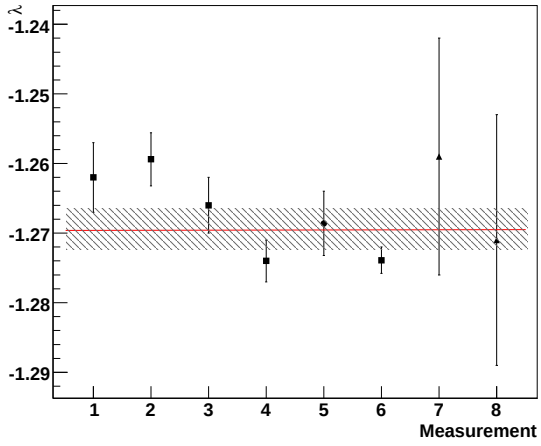

Figure 1.12: Determination of λ from neutron decay experiments. The λ value recommended by the Particle Data Group [Ams08] is represented with the band. Most data points were obtained from measurements of the parameter A: 1 [Bop86]; 2 [Yer97]; 3 [Lia97]; 4 [Abe97]; 6 [Abe02]). Measurements 7 [Str78] and 8 [Byr02] were obtained by measuring the angular correlation coefficient a, whereas measurement 5 [Mos01] was obtained from a simultaneous measurement of A and a.

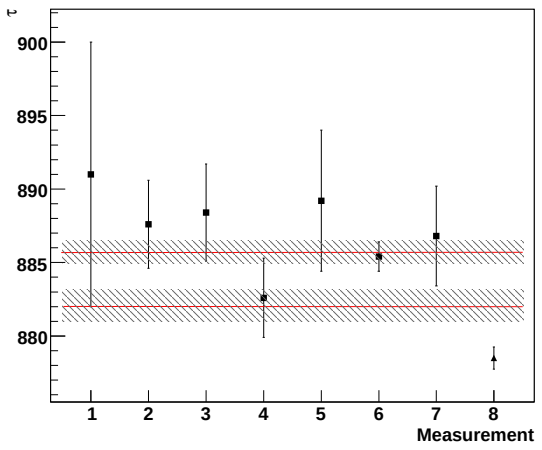

Figure 1.13: Different neutron lifetime measurements are plotted: 1 [Spi88]; 2 [Mam89]; 3 [Nes92]; 4 [Mam93]; 5 [Byr96]; 6 [Arz00]; 7 [Dew03]; 8 [Ser05]. The upper band refers to the weighted average of the first seven values and recommended by the Particle Data Group [Ams08], setting $\tau_n = 885.7(8)$ s. The lower band shows the weighted average of all values, obtaining $\tau_n = 882(1.1)$ s.

Nowadays, the most precise λ determination from free neutron decay comes from parameter A experiments yielding, $\lambda = -1.2739(19)$ [Abe02]. However, the recommended value by the Particle Data Group [Ams08] is:

$$\lambda = -1.2695(29) \tag{1.62}$$

In Fig. 1.12 (measurement 1 to 6) one can notice a variation among the different data points of λ determined from beta asymmetry experiments. By improving the accuracy of the measurement, a reduction of the λ value is observed. This variation can be an

indication that unknown systematic errors are strongly entering A measurements [Gar01]. To check this hypothesis an accurate measurement of the angular correlation coefficient a would be needed because it can determine λ with different systematic errors. But the most accurate experiment of parameter a performed up to now determines a λ value with an error almost one order of magnitude worse than parameter A (see in Fig. 1.12 measurements 7 and 8). For that reason, the construction of new instruments with the aim to improve the accuracy of a and A measurements has been increased during the last years [Wie05] [Jon09] [You02].

Among the several neutron lifetime measurements there exist also discrepancies. In Fig. 1.13, measurements 1 to 7 show some input data used to extract the world average value of τ_n (mainly dominated by measurement 6, the value reported by Arzumanov *et al.*, [Arz00]):

$$\tau_n = 885.7(8)s \tag{1.63}$$

This compilation does not include yet the value reported by Serebrov *et al.* in 2005 (see [Ser05] and measurement 8 from Fig. 1.13) which differs by 6.5 standard deviations from the world average value. In case we would take also this measurement into account, the world average neutron lifetime would be $\tau_n = 882(1.1)$ seconds. Such a change in the neutron lifetime would have a very significant effect on the CKM unitarity condition 1.13.

Concerning the element V_{us}, new measurements involving semileptonic branching fractions, semileptonic form factors and kaon lifetimes have introduced significant changes to the previous values (see references [Blu05], [Ams08]). The value adopted by the Particle Data Group in 2008 is:

$$V_{us} = 0.2255 \pm 0.0019 \tag{1.64}$$

Still, alternative calculations of the form factors determine values of $|V_{us}|$ that differ by as much as 2 per cent from the PDG result [Jam04].

As it has been presented above, inconsistencies in the various V_{ud} and V_{us} determinations are problematic when testing the CKM unitarity. For the V_{ud} determination case, new experimental data from neutron beta decay experiments would be very welcome, like for example, new lifetime experiments, in order to solve the unsatisfactory situation of having two inconsistent lifetime values. But also there are needed more precise measurements of the correlation coefficient a competitive with measurements of the A parameter to determine λ with entirely different systematic errors.

1.5.2 CVC

Nuclear β-decay experiments are the most accurate tests of the CVC hypothesis, checked to a level of 5% of uncertainty [Sev06]. In this kind of tests, the CVC hypothesis is tested assuming Second Class Currents to be zero. Alternatively, the nonexistence of Second Class Currents can be tested if the CVC hypothesis is assumed to be zero.

Combining measurements of the angular correlation coefficients a and A from neutron decay to a level of accuracy of at least 1%, tests of the CVC and the existence of Second Class Currents are possible [Gard01]. However, in order to reach a result which confirms the CVC hypothesis to an accuracy of 10%, precise measurements of a and A to the order of 0.1% are needed. This challenge seems quite feasible in the case of A measurements but not yet for the coefficient a.

1.5.3 Right-handed currents

The beta decay Hamiltonian with right-handed current contributions can be parameterized in terms of the quantities r_V and r_A [Beg77]:

$$r_V = \frac{1+\eta_{VA}}{1-\eta_{VA}}, \qquad r_A = \frac{\eta_{AA}+\eta_{VA}}{\eta_{AA}-\eta_{VA}} \tag{1.65}$$

The coefficients η_{AA} and η_{VA} are related to the mass parameter δ and the mixing angle ζ of the $U(1) \times SU(2)_R \times SU(2)_L$ model by (see Section **??**):

$$\eta_{AA} = \frac{\epsilon^2+\delta}{\epsilon^2\delta+1}, \qquad \eta_{VA} = -\epsilon\frac{1-\delta}{\epsilon^2\delta+1} \tag{1.66}$$

where $\epsilon = (1+\tan\zeta)/(1-\tan\zeta)$. In the $V-A$ theory both δ and ϵ are 0.

The correlation coefficients a, A and B are also sensitive to parity violation. Their expressions in the left-right symmetric model are the following [Sch07]:

$$a = \frac{(1+r_V^2)-\lambda'^2(1+r_A^2)}{(1+r_V^2)+3\lambda'^2(1+r_A^2)} \tag{1.67}$$

$$A = -2\frac{\lambda'(\lambda'+1)-r_A\lambda'(r_A\lambda'+r_V)}{(1+r_V^2)+3\lambda'^2(1+r_A^2)} \tag{1.68}$$

$$B = 2\frac{\lambda'(\lambda'-1)-r_A\lambda'(r_A\lambda'-r_V)}{(1+r_V^2)+3\lambda'^2(1+r_A^2)} \tag{1.69}$$

where the parameter λ' is defined as:

$$\lambda' = \frac{g'_A}{g'_V} = \frac{\eta_{AA}-\eta_{VA}}{1-\eta_{VA}} \tag{1.70}$$

Notice that for $r_V = r_A = 0$ the correlation coefficients 1.67 to 1.69 are the same as the ones in the Standard Model case, Eq. 1.47.

In principle, a more precise measurement of a could help to discriminate between the Standard Model scenario and a scenario with additional right-handed currents. For

example, it has been calculated[17] (see [Kon11] [Kon10a]) that the limits for δ and ζ values, in the 95% CL, are about 2 times more constrained using the currently recommended PDG values when a is measured with an accuracy of 0.3%. However, in this calculation there is also a strong dependency of the constraint on the values and precision of all the parameters involved in the calculation.

1.5.4 Scalar and Tensor contributions

In [Jac57] one can find the general derivation of the expressions of the correlation coefficients as functions of the coupling constants and nuclear matrix elements of the Hamiltonian in Eq. 1.8. Applying the relations of Eq. 1.38, the expressions of the correlation coefficients a, A, B in neutron decay as a function of the coupling constants are the following:

$$a = \frac{-|C_S|^2 + |C_V|^2 + |C_T|^2 - |C_A|^2}{|C_S|^2 + |C_V|^2 + 3|C_T|^2 + 3|C_A|^2} = \frac{1 - x^2 + y^2\lambda^2 - \lambda^2}{x^2 + 1 + 3\lambda^2 y^2 + 3\lambda^2} \tag{1.71}$$

$$A = -2\frac{|C_A|^2 + C_A C_V + C_S C_T + |C_T|^2}{|C_S|^2 + |C_V|^2 + 3|C_T|^2 + 3|C_A|^2} = -2\frac{\lambda^2 + \lambda + \lambda xy + \lambda^2 y^2}{x^2 + 1 + 3\lambda^2 y^2 + 3\lambda^2} \tag{1.72}$$

$$B = 2\frac{|C_A|^2 - C_A C_V + C_S C_T - |C_T|^2}{|C_S|^2 + |C_V|^2 + 3|C_T|^2 + 3|C_A|^2} = 2\frac{\lambda^2 - \lambda + \lambda xy - \lambda^2 y^2}{x^2 + 1 + 3\lambda^2 y^2 + 3\lambda^2} \tag{1.73}$$

The correlation coefficients can be written in terms of three parameters:

$$\lambda = \frac{C_A}{C_V}, \qquad x = \frac{C_S}{C_V}, \qquad y = \frac{C_T}{C_A} \tag{1.74}$$

To determine limits on right-handed scalar and tensor contributions to the weak interaction, are at least necessary three measured quantities as input values (for example, a, A, B) for a system of three unknown parameters (x, y, λ). Note that the $V - A$ limit corresponds to $x = y = 0$.

The current limits using a as input parameter give not very precise constrains [Sch07] since the accuracy of the current value of a is still too low.

It has been calculated that by improving the accuracy of the current value of a in one order of magnitude, the limits for x and y, within the 95% CL, are a factor 7 more constrained [Kon11] [Kon10a]. The input parameters entering this example (including the neutron lifetime) have been extracted from the PDG tables. But, like in the case of right-handed current constraints calculations, these results are strongly dependent on the input values used.

[17] The input parameters include also the neutron lifetime.

1.6 Previous measurements of a

The measurement of the coefficient a is not trivial. It can not be measured directly since there are no neutrino detectors with high efficiency. The solution is the measurement of an experimentally accessible parameter sensitive to a, of which are basically three [Byr82]:

- Measurement of the distribution of decay events as a function of the angle between electron and recoiling proton.
- Measurement of the momentum spectrum of electrons emitted into a given range of angles referred to the proton momentum.
- Measurement of the spectrum of recoiling protons either in coincidence with selected electrons or not.

The most accurate result of a published so far has been obtained by measuring the proton recoil spectrum. The current world average is $a = -0.103(4)$ [Ams08].

First determinations of a were performed during the late fifties [Rob58] [Vla61] but the results extracted were so inaccurate that a values were compatible with zero. The first sophisticated measurement of a was carried out by Stratowa *et al.* in 1978 [Str78]. They measured with high precision the proton energy spectrum from neutron decays occurring in an evacuated through-tube near the core of the reactor ASTRA, in Austria. The experimental setup used is shown in Fig. 1.14.

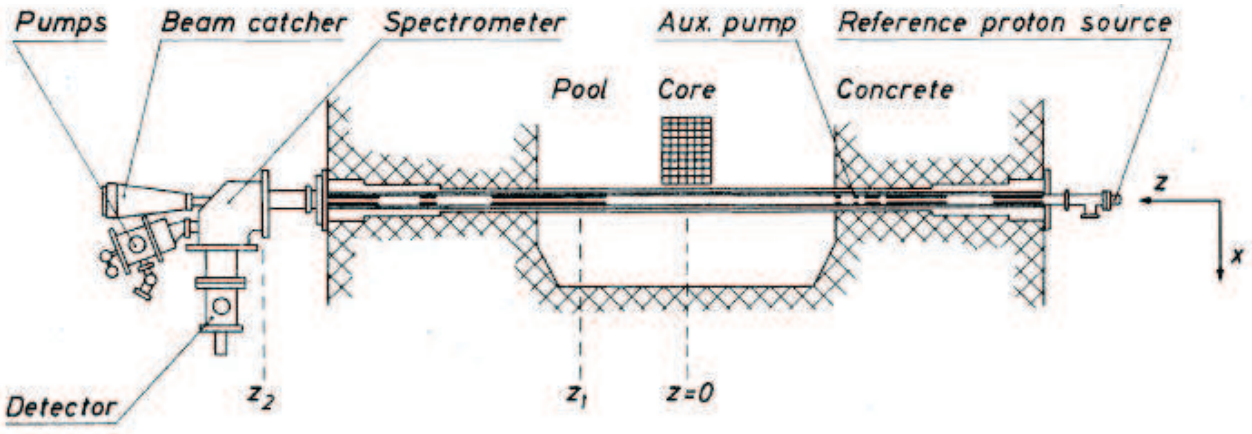

Figure 1.14: Experimental setup for determining the electron-neutrino angular correlation coefficient from the proton energy spectrum by Stratowa *et al.* in 1978 (image taken from Ref. [Str78]).

In this experiment the decay protons are energetically selected by a 90 degrees spherical condenser, created by the small solid angle defined by the apertures z_1 and z_2. The particles passing the exit aperture of the condenser are accelerated through a potential difference of -25 kV, and focused onto a thin aluminum foil, inclined by 45 degrees with

respect to the proton beam. The secondary electrons ejected from both sides of this foil are accelerated and focused onto two plastic scintillators and are counted in coincidence in order to suppress the background. The calibration of the neutron decay proton spectrum was carried out using a proton source mounted at the opposite end of the tangential beam tube.

The main source of errors during the experiment came from energy-dependent factors in the transmission of the spectrometer and from the detection efficiency. The result of the experiment was $a = -0.1017(51)$

Since 1978 there has been one further experiment measuring a with similar accuracy to the one of Stratowa *et al.* It was performed about twenty years later by Byrne *et al.* [Byr02] at the Institut Laue Langevin, in France. In Fig. 1.15 the experimental setup is shown. A collimated beam of cold neutrons is passing through a quasi-Penning trap, created by superpositioning a coaxial system of electrodes on an axially symmetric magnetic field whose strength can be varied from 0.6 T to 4.3 T. The closest electrode to the detector is designated as the "gate" while the far end is designated as the "mirror" electrode. In the simplest method, the potential on the gate electrode is kept constant (at about 0.85 kV) while the mirror electrode is set at different potentials V_0 in order to measure the number $N(V_0)$ of protons trapped behind a barrier of variable height V_0. A non-uniform magnetic field is used to transfer the proton kinetic energy from the transverse to the longitudinal mode[18], so that at the postion of the mirror electrode the energy in the longitudinal mode is maximum. After a trapping time of 1 ms, $N(V_0)$ is measured by "opening" the gate electrode, allowing the trapped protons to reach the detector.

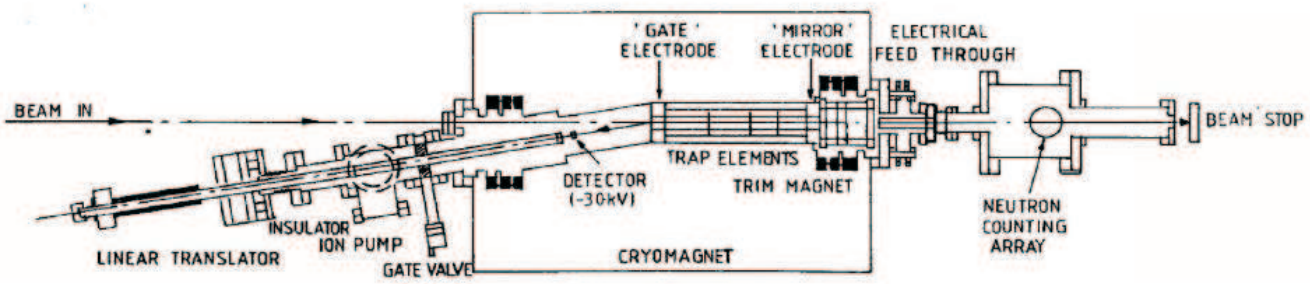

Figure 1.15: Experimental setup for determining the electron-neutrino angular correlation coefficient from the proton energy spectrum by Byrne et al. in 2002.

However, it was found that the energy transfer to the longitudinal mode was not properly fulfilled and that the adiabatic conditions were not fully accomplished. Therefore systematic corrections were needed which, together with low statistical power, limited the accuracy. Nevertheless, the result of $a = -0.1054(55)$ is in good agreement with the previous measurement and of comparable precision.

[18]This effect is described as inverse magnetic mirror effect.

Chapter 2

The *a*SPECT spectrometer

The proton spectrometer *a*SPECT started its operation in summer 2005, at the neutron beam-line MEPHISTO at the Forschungsneutronenquelle Heinz Maier-Leibnitz (FRM-II) in Munich. *a*SPECT measures the integral proton spectrum from the free neutron decay in order to extract the correlation coefficient a. It is an improved version of the Stratowa *et al.* experiment [Str78], designed to measure the coefficient a with an accuracy better than 3×10^{-4}. In this chapter, the design, working principle and setup of the spectrometer at the FRM-II are presented in detail.

2.1 Measurement principle

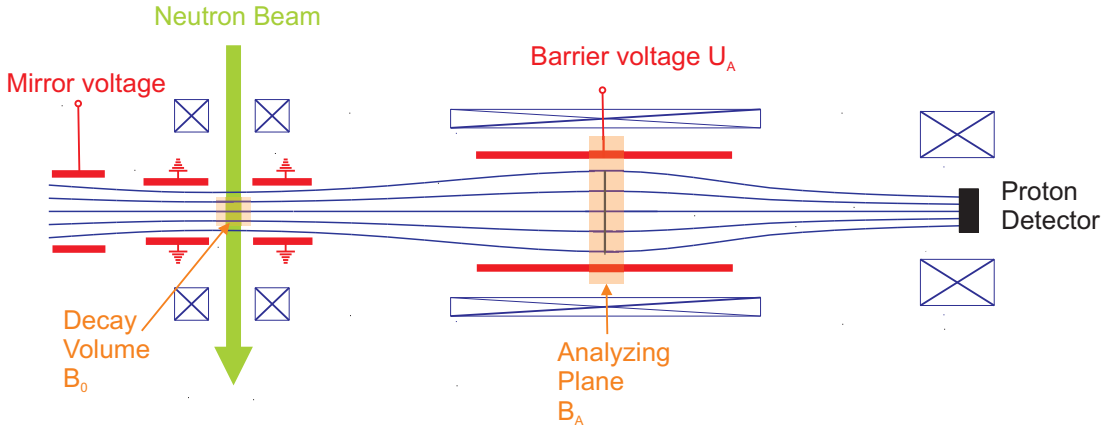

Figure 2.1: Simplified scheme of the *a*SPECT spectrometer. Electrodes are indicated in red whereas crosses show the coils position. Protons created in the decay volume are guided towards the detector by magnetic fields, whose magnetic field lines are plotted in blue. Only those protons with enough energy to pass the barrier voltage applied at the analyzing plane will reach the detector, where they will be counted.

The design of the *a*SPECT spectrometer is based on the so-called Magnetic Adiabatic Collimation followed by an Electrostatic Filter (MAC-E-Filter) and consists of a set of

electrodes and superconducting coils. In Fig. 2.1 a sketch of the spectrometer is shown. A cold unpolarized neutron beam is guided through the spectrometer to the **Decay Volume** (DV), where a strong magnetic field B_0 is applied. A fraction of about 10^{-8} of the neutrons decay in this region. The decay protons are guided by the strong magnetic field towards the proton detector, placed on top of the spectrometer. About one half of the protons are initially emitted opposite to the detector's direction. An electrostatic **Mirror Electrode** placed below the decay volume is used to reflect these protons back. The spectrometer achieves therefore a 4π acceptance for protons created in the decay volume.

On their way to the detector the protons are adiabatically collimated by crossing a region of weaker magnetic field. This means, their perpendicular kinetic energy component is transferred, to some extent, into the longitudinal component. At the **Analyzing Plane** (AP) region with a magnetic field B_A, an electrostatic potential barrier is applied. Only protons with sufficient energy will overcome the barrier and subsequently will be accelerated towards the detector where they will be counted. The analyzing plane is set to different voltages U_A in order to obtain information on the shape of the complete proton spectrum. The action of the potential barrier can be described by a transmission function (Eq. 2.23), which represents the probability that a proton with a given starting kinetic energy passes the analyzing plane. Keeping the motion of the decay protons adiabatic, the transmission function is known analytically, and only depends on the settings of U_A, B_0 and B_A.

2.2 MAC-E-Filter Spectrometer

*a*SPECT was designed in a way that the motion of the decay protons fulfills the *adiabatic approximation* [Jac75]. This approximation is valid when the relative changes of the electromagnetic fields are small during one gyration of the proton, i.e., if $\Delta B/B \ll 1$ and $\Delta E/E \ll 1$. In this approximation, it turns out that most of perpendicular proton kinetic energy can be transferred to the parallel component, without changes on the total kinetic energy. This effect, called **Magnetic Adiabatic Collimation** (or *Inverse Magnetic Mirror effect*) is fundamental for the *a*SPECT spectrometer since the potential barrier applied at the analyzing plane is only sensitive to the longitudinal momentum component of the proton.

The helical motion of a charged particle[1] in electromagnetic fields arise from the magnetic-force term $q(\vec{v} \times \vec{B})$ in the Lorentz force equation:

$$\vec{F} = q(\vec{v} \times \vec{B}) + q\vec{E} \tag{2.1}$$

where $\vec{v}$ and q are the velocity and the charge of the particle, while $\vec{B}$ and $\vec{E}$ are the magnetic and electric fields, respectively. The motion of a charged particle in a spatially slowly varying magnetic field can be split in first approximation into a longitudinal and a tangential motion, with respective momenta $p_{||}$ and $p_{\perp}$. If the magnetic field changes slowly enough in space or time, the magnetic flux through the particle's orbit (with

[1] In our case decay protons and electrons from neutron beta decay.

gyration radius r) $B\pi r^2$ remains constant [Jac75]. Observables related to this quantity, like the transverse momentum and the magnetic moment of the charged particle lead to the following *adiabatic invariants*:

$$\begin{gathered} Br^2 \\ p_\perp^2/B \\ \gamma\mu \end{gathered}$$

where $\gamma = 1/\sqrt{1 - v^2/c^2}$ is the relativistic factor and μ the magnetic moment of the current loop of the charged particle, defined by

$$\mu = \frac{e\omega r^2}{2} \tag{2.2}$$

where the gyration frequency of cyclotron motion ω is given by

$$\omega = \frac{qB}{\gamma m} \tag{2.3}$$

The Magnetic Adiabatic Collimation combined with an Electrostatic Filter (the so-called MAC-E Filter) was first applied in electron spectroscopy [Hsu76] [Bea80] [Kru83]. This principle was successfully used on neutrino mass measurements which determine the tritium beta spectrum [Lob85] with experiments performed at Troitsk and at Mainz. A next generation of tritium beta decay experiment, the Karlsruhe Tritium Neutrino (KATRIN) experiment, is under construction [Kra05] [Ang04] [Ott08]. The new experiment consists of a huge MAC-E Filter which provides a higher sensitivity.

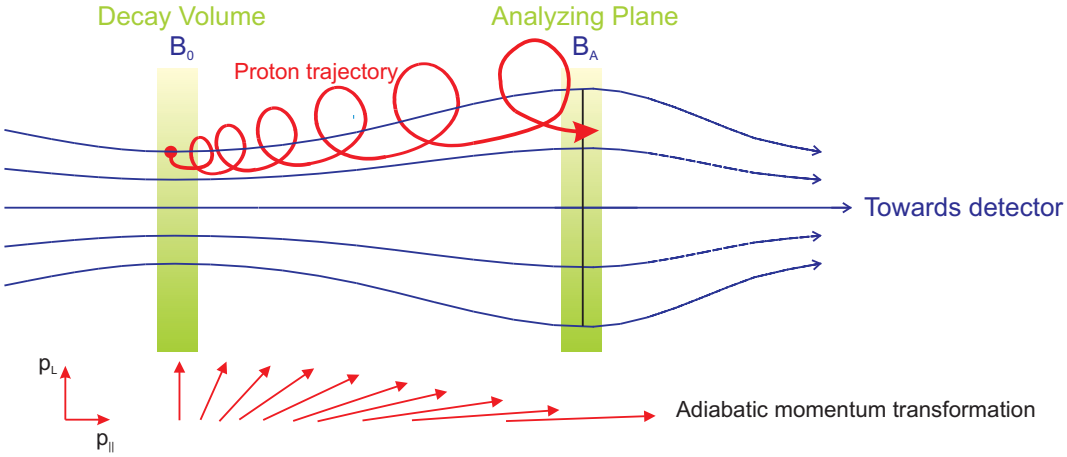

Figure 2.2: Scheme of the aSPECT MAC-E-Filter spectrometer. Notice the adiabatic proton momentum transformation between the decay volume and the analyzing plane.

The main features of the MAC-E-Filter of the aSPECT spectrometer are illustrated in Fig. 2.2. It comprises the region between the decay volume and the detector and consists of a set of cylindrical electrodes plus a set of superconducting coils which produce a guiding magnetic field. The neutrons decay isotropically in the decay volume, where a strong

magnetic field B_0 is applied, and are magnetically guided on a helical motion along the spectrometer. The magnetic field at the analyzing plane, B_A, is much lower than in the decay volume. During this process, due to magnetic gradient forces, most of the cyclotron (gyration) momentum $p_\perp$ transforms into longitudinal momentum $p_{||}$, to an extent that depends on the ratio

$$r_B = \frac{B_A}{B_0} \tag{2.4}$$

Since the spatial variations of the electromagnetic fields are small, we apply the adiabatic approximation, in which the magnetic moment μ is considered to be constant:

$$\mu = \frac{p_\perp^2}{2m_p B} = \text{constant} \tag{2.5}$$

where m_p is the proton mass and γ has been set to 1, because proton energies from neutron decay are very low. When the almost parallel proton beam reaches the analyzing plane an electrostatic potential U_A is applied. Only protons with enough energy to pass the electrostatic barrier are electrically accelerated and focused by a higher magnetic field on to the detector.

For small r_B values the perpendicular proton momentum $p_\perp$ conversion into the longitudinal momentum $p_{||}$ is more complete, and therefore, the resolution of the spectrometer increases. When $r_B \to 0$, the momentum conversion is fully achieved and the transmission function becomes a step function. However, this implies the use of a huge spectrometer, impossible to handle. In order to keep at the same time a reasonable spectrometer size and to not loose too much resolution, the value of r_B in *a*SPECT was chosen to be about 0.2. With this ratio, deviations from the adiabatic approximation can be neglected [Glü05], and the loss of sensitivity of the spectrometer is less than 10% compared to a configuration with $r_B \approx 0$ [Zim00].

To check if the adiabatic approximation is fulfilled along the spectrometer, trajectory calculations for given field maps of the electric potential and the magnetic field are needed. Charged particle trajectories in the electric and magnetic field of the spectrometer were computed using an 8^{th} order Runge-Kutta algorithm. The calculations show that the value of μ in the analyzing plane is close to its value at the decay volume. But in the regions with high electric and magnetic field gradients, the value of μ oscillates with a period equal to the local gyration period and the oscillation amplitude increases with the field gradients (see [Glü05] and references therein).

2.3 The Transmission function

The transmission function $F_{tr}(T_0)$ gives the probability that a proton with a given starting kinetic energy T_0 passes the barrier voltage U_A applied at the analyzing plane[2]. For the operation of the spectrometer aSPECT, the knowledge of the transmission function is essential. For this it is necessary to keep the motion of the decay protons adiabatic. Under this requirement, the transmission function can be calculated analytically and has enough resolution to lead to a measurement of the coefficient a with an accuracy of $\delta a = 3 \times 10^{-4}$.

The kinetic energy of the protons can be decomposed into parallel and perpendicular components with respect to the z-axis[3] (direction of the magnetic field lines):

$$T_\perp = T \sin^2 \theta \tag{2.6}$$

$$T_{||} = T \cos^2 \theta \tag{2.7}$$

where θ is the angle between the momentum of the proton and the z-axis. In the adiabatic approximation the magnetic moment μ of the proton is an invariant (see Eq. 2.5),

$$\mu = \frac{p_\perp^2}{2 m_p B} = \frac{T \sin^2 \theta}{B} = \text{constant} \tag{2.8}$$

which is valid for a proton of mass m_p at any point of the trajectory with magnetic field B. Let's equal the magnetic moment μ of a proton at any point of the trajectory with the magnetic moment μ_0 at the point where it was created:

$$\frac{T_0 \sin^2 \theta_0}{B_0} = \frac{T \sin^2 \theta}{B} \tag{2.9}$$

The index 0 indicates the initial position of the trajectory where the proton is generated (in the decay volume). No index indicates any other point of the trajectory. From Eq. 2.9 we obtain:

$$\sin^2 \theta = \frac{B}{B_0} \frac{T_0}{T} \sin^2 \theta_0 \tag{2.10}$$

Combining Eqs. 2.7 and 2.10 the longitudinal proton kinetic energy can be expressed at any point of the trajectory:

$$T_{||} = T(1 - \sin^2 \theta) = T - \frac{B}{B_0} T_0 \sin^2 \theta_0 \tag{2.11}$$

The total energy E of the proton at any point of its trajectory consists of a kinetic energy contribution T and a potential energy contribution V, i.e., $E = T + V$. The total energy of the proton when is generated at the decay volume is fully kinetic because $V_0 = eU_0 = 0$, and therefore $E_0 = T_0$. At any other point of its trajectory, the proton has kinetic energy

[2]In this context we assume that all protons which cross the analyzing plane reach the detector.

[3]The derivation of the transmission function follows the references [Glü05] and [Aya05].

T and potential energy $V = e(U - U_0)$, implying $E = T + e(U - U_0)$. Since the total proton energy is conserved, $E_0 = E$, and therefore:

$$T_0 = T + e(U - U_0) \quad \rightarrow \quad T = T_0 - e(U - U_0) \tag{2.12}$$

Using Eqs. 2.11 and 2.12 the longitudinal kinetic energy of the proton can be rewritten at any point of its trajectory:

$$T_{||} = T_0 - e(U - U_0) - \frac{B}{B_0} T_0 \sin^2 \theta_0 \tag{2.13}$$

It is important to notice that for a proton to be transmitted, $T_{||}$ has to be positive at each point of its trajectory. Otherwise the proton is reflected. In the *a*SPECT spectrometer protons reach the minimum of longitudinal kinetic energy at the analyzing plane, where a barrier voltage U_A is applied. Protons that will overcome the barrier voltage are those with initial kinetic energy of at least T_{tr} (see Fig. 2.3), that is the initial kinetic energy for which $T_{||,A} = 0$, given by:

$$T_{tr}(\theta_0) = \frac{e(U_A - U_0)}{1 - \frac{B_A}{B_0} \sin^2 \theta_0} \tag{2.14}$$

T_{tr} is a function of θ_0, the angle between the proton momentum at the decay volume and the z-axis. θ_0 takes values from 0° to 180°. For a fixed emission angle θ_0, the transmission function $F_{tr}(T_0, \theta_0)$ can be written as:

$$F_{tr}(T_0, \theta_0) = \begin{cases} 1 & \text{if } T_0 > \frac{e(U_A - U_0)}{1 - \frac{B_A}{B_0} \sin^2 \theta_0} \\ 0 & \text{otherwise} \end{cases} \tag{2.15}$$

The transmission energy T_{tr} is minimal for $\theta_0 = 0$ and $\theta_0 = \pi$, and has a maximum for $\theta_0 = \frac{\pi}{2}$ (see Fig. 2.3). T_{tr}^{min} and T_{tr}^{max} are written as :

$$T_{tr}^{min} = e(U_A - U_0), \qquad T_{tr}^{max} = \frac{T_{tr}^{min}}{1 - \frac{B_A}{B_0}} \tag{2.16}$$

Protons with initial kinetic energy T_0 smaller than T_{tr}^{min} will be reflected and protons with energies bigger than T_{tr}^{max} will pass the barrier voltage. The ratio of transmitted protons with initial kinetic energies within the range $T_{tr}^{min} < T_0 < T_{tr}^{max}$ will depend on the initial angle θ_0.

The number of transmitted protons $\rho_{tr}(T_0)$ and the total number of protons emitted in the same hemisphere pointing towards the detector[4] $\rho_{total}(T_0)$ for a given initial kinetic energy T_0 are, respectively:

[4]The protons emitted into the other hemisphere are reflected by the mirror electrode. For symmetry reasons, the transmission function for those protons obeys the same dependence.

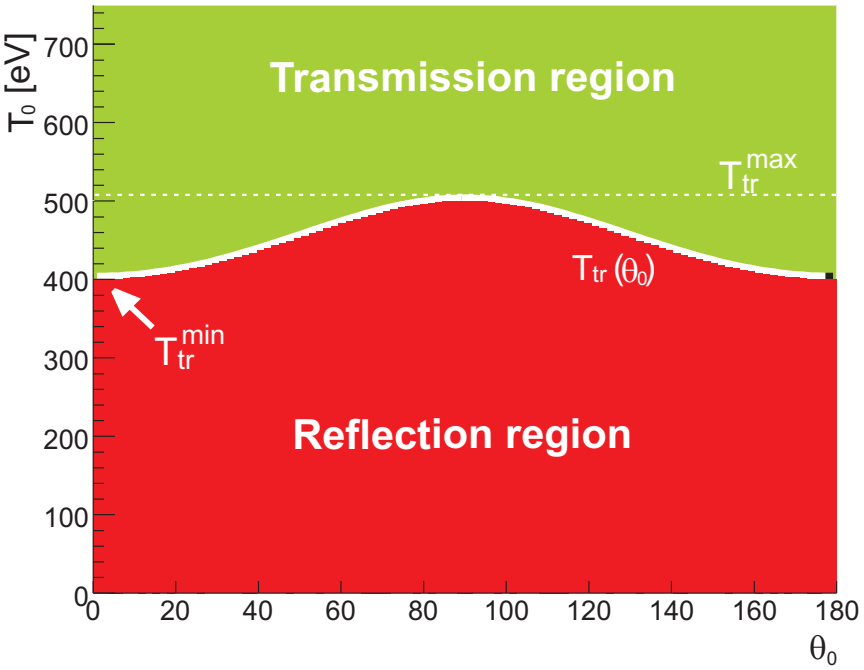

Figure 2.3: Angular dependence of the transmission kinetic energy $T_{tr}(\theta_0)$ shown for a potential barrier $U_A - U_0 = 400V$. T_{tr} is defined in Eq. 2.14. Only protons with initial kinetic energy $T_0 > T_{tr}(\theta_0)$ will be transmitted. Notice that if the adiabatic transmission condition is fulfilled for $\theta_0 = 90°$, it is also fulfilled for any other value of θ_0.

$$\rho_{tr}(T_0) = \int_0^{2\pi} d\phi \int_0^{\theta_0^{max}} \sin\theta_0 d\theta_0 \omega_p(T_0) \tag{2.17}$$

and

$$\rho_{total}(T_0) = \int_0^{2\pi} d\phi \int_0^{\pi/2} \sin\theta_0 d\theta_0 \omega_p(T_0) \tag{2.18}$$

where θ_0^{max} is the maximum initial angle that a transmitted proton with initial kinetic energy T_0 has to have to pass the barrier. Please note that θ_0^{max} is derived from Eq. 2.14 assuming $T_{tr} = T_0$ and therefore depends on T_0, B_A, B_0, U_A and U_0. $\omega_p(T_0)$ is the proton recoil spectrum (introduced in Section 1.4.5) which is not angular dependent. Thus, the integral can be evaluated, resulting in

$$\rho_{tr}(T_0) = 2\pi\omega_p(T_0)(1 - \cos\theta_0^{max}) \tag{2.19}$$

$$\rho_{total}(T_0) = 2\pi\omega_p(T_0) \tag{2.20}$$

Consequently, for $T_{tr}^{min} < T_0 < T_{tr}^{max}$ the transmission probability is given by:

$$\frac{\rho_{tr}(T_0)}{\rho_{total}(T_0)} = 1 - \cos\theta_0^{max} \tag{2.21}$$

The transmission cosine function $c_{tr}(T_0)$ is introduced by combining Eqs. 2.14 and 2.16:

$$c_{tr}(T_0) = \cos\theta_0^{max} = \sqrt{1 - \frac{B_0}{B_A}(1 - \frac{T_{tr}^{min}}{T_0})} \tag{2.22}$$

Finally, the adiabatic transmission function $F_{tr}(T_0)$, which is represented in Fig. 2.4 reads as follows:

$$F_{tr}(T_0) = \begin{cases} 0 & \text{if } T_0 \leq T_{tr}^{min} \\ 1 - c_{tr}(T_0) & \text{if } T_{tr}^{min} < T_0 < T_{tr}^{max} \\ 1 & \text{if } T_0 \geq T_{tr}^{max} \end{cases} \tag{2.23}$$

Please note that in Eq. 2.23 the transmission function depends only on the electrostatic potential and magnetic field values at the decay volume and at the analyzing plane. As long as the adiabatic approximation holds, it is independent of the detailed shape of the electromagnetic field. For a measurement of the angular correlation coefficient a with an accuracy of $\delta a \approx 3 \times 10^{-4}$, the magnetic field ratio B_A/B_0 has to be known with an accuracy of 10^{-4}. On the other hand, electric field inhomogeneities in the decay volume could result in the reflection of protons and/or proton trapping in this region. These effects are difficult to calculate, but it has been estimated that already a potential difference $U_A - U_0$ of 2 mV introduces an error in a of about 2×10^{-3} [Kon11]. The extreme sensitivity of a to small variations of the electrostatic potential in the decay volume is a crucial factor for the overall accuracy of the aSPECT experiment.

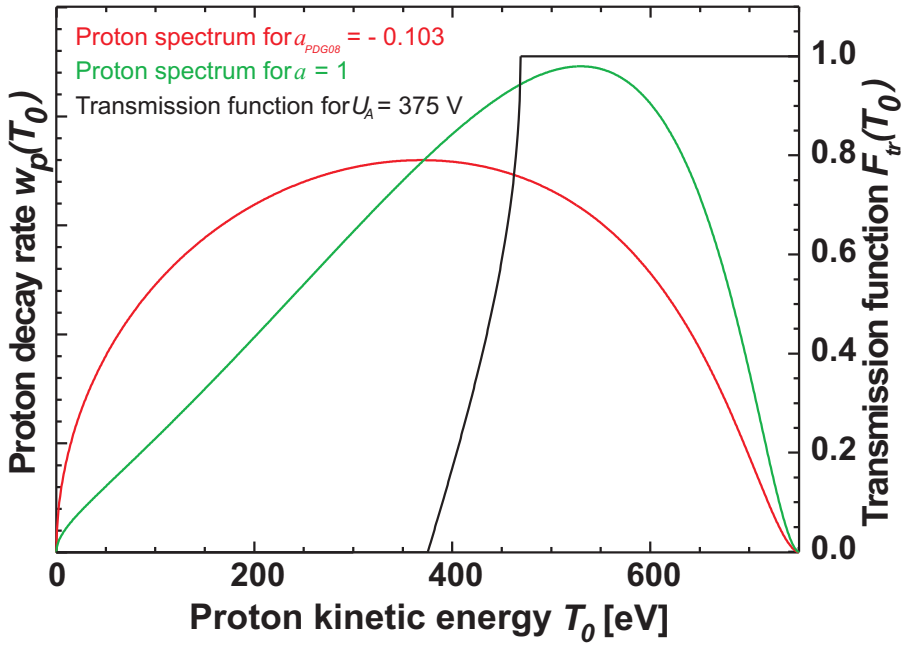

Figure 2.4: The black curve represents the adiabatic transmission function defined in Eq. 2.23 when applying 375 V at the barrier voltage. Two calculated proton spectra are as well shown for different a values.

2.4 Experimental setup

2.4.1 Neutron beam and collimation system

To measure the proton spectrum from free unpolarized neutrons, a cold neutron beam is most suitable. It offers the best compromise between probability of decay neutrons inside the decay volume and the need of high counting statistics. At the FRM-II, the cold neutron source is moderated with liquid deuterium which generates low-energy neutrons with a Maxwell distribution centered around 5 meV, corresponding to a wavelength of 4 Å. The neutron flux during our beam time was about 2×10^{10} cm^{-2}s^{-1}. This was the most intense cold neutron beam in the world at that time. The whole setup is shown in Fig. 2.5.

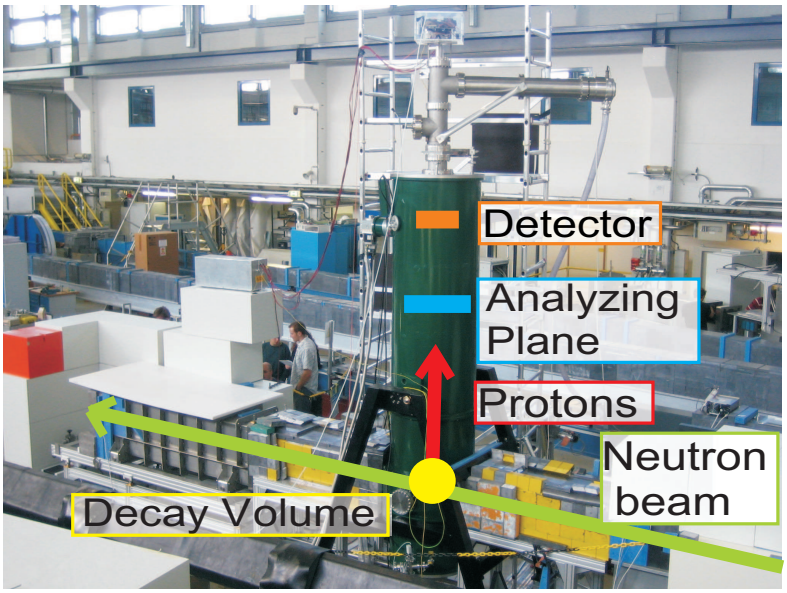

Figure 2.5: The aSPECT spectrometer placed at the reactor hall of the FRM-II, in Munich, Germany. The nuclear reactor sits on the right side of the picture, from where the collimated neutron beam crosses the spectrometer perpendicularly with respect to the magnetic field lines at the height of the decay volume. Decay protons originated in this volume with enough kinetic energy to cross the analyzing plane voltage U_A will be focused onto the detector, placed on top of the spectrometer.

The spectrometer was attached to the neutron guide NL3a of the reactor via two CF-200 bellows interconnected by a 65 cm long CF-200 stainless steel tube. This system provides some freedom for a fine alignment between the spectrometer beam axis and the neutron guide.

The adiabatic transmission function assumes that all protons produced at the decay volume experience the same magnetic field B_0, meaning that a homogeneous distribution of the neutron beam over the decay volume is needed. However, since the magnetic field within the decay volume and the analyzing plane regions are not perfectly uniform, it is necessary to measure with a certain accuracy[5] the spacial distribution of the neutron

[5] A less homogeneous magnetic field B_0 would require a more accurate neutron density measurement.

density n (see Section 3.2.6 for further discussion). Then, its weighting will be included into the transmission function.

Because of its divergence and rather large cross section, the neutron beam has to be collimated. The collimation system has to be designed in a way that it minimizes the probability of neutrons to hit the walls of the collimation system and of the rest of the experimental setup, in order to reduce the background, and to do not activate the spectrometer material.

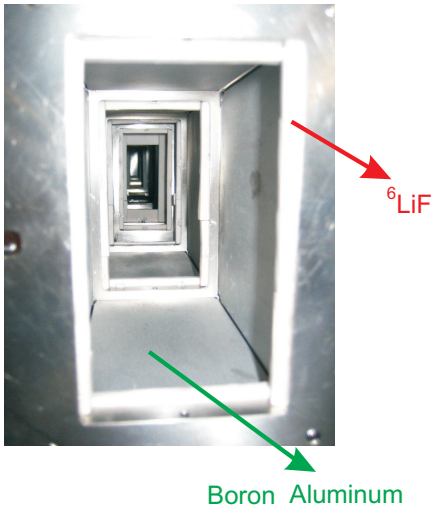

Figure 2.6: Several apertures of ^6LiF placed inside the spectrometer.

A Monte Carlo simulation was performed to find the best collimation configuration. The number of simulated neutrons was about 10^6, assuming in a first order approximation, that no backscattering processes took place. A detailed schema of the whole collimation system implemented in the neutron beam line can be seen in Fig. 2.9.

The first part of the neutron beam collimation system consists of two apertures installed inside the beam line. They are made of several layers of boron loaded plastic glued onto two semicircular lead pieces with a thickness of 50 mm. Biological shielding is provided by tubes of boron-silicate glass and boron-aluminum installed into the beam line. The second part of the collimation consists of five apertures made from isotopically enriched lithium fluoride. Four of them are installed at the entrance of the decay volume and the other one at the exit. They can be seen in Fig. 2.6.

The neutron beam is guided through the spectrometer to a beam stop, placed about 3.5 meters downstream from the decay volume. The beam stop consists of a vacuum tank shielded with several layers of boron loaded plastic and lead. At the entrance and exit of the spectrometer beam line a magnesium alloy (MgAl3Zn1) windows with a thickness of 250 μm are used to separate the vacuum of the collimation system, of about 10^{-2} mbar, from the spectrometer main vacuum, of about 2×10^{-8} mbar. Both, the entrance and exit collimator tubes are surrounded by roughly 5 cm of boron loaded plastic and 5 to 10 cm of lead. The stability of the neutron beam intensity is continuously monitored by means of a fission chamber, placed at the beam stop.

During the data-taking periods (typically several hours), the neutron count rates,

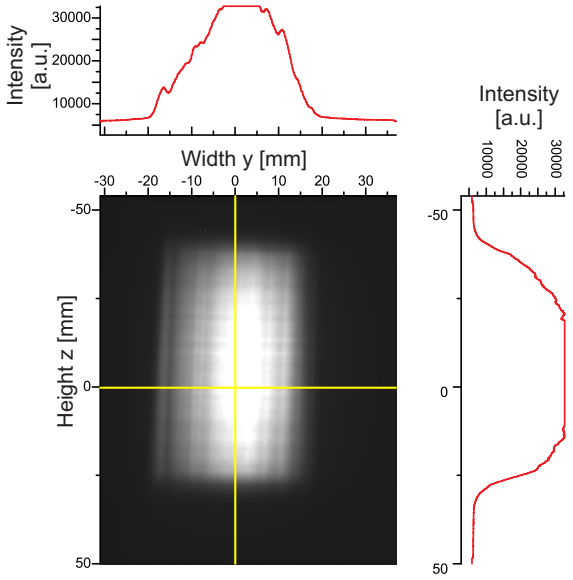

Figure 2.7: Neutron beam image taken at the exit of the spectrometer with a neutron camera.

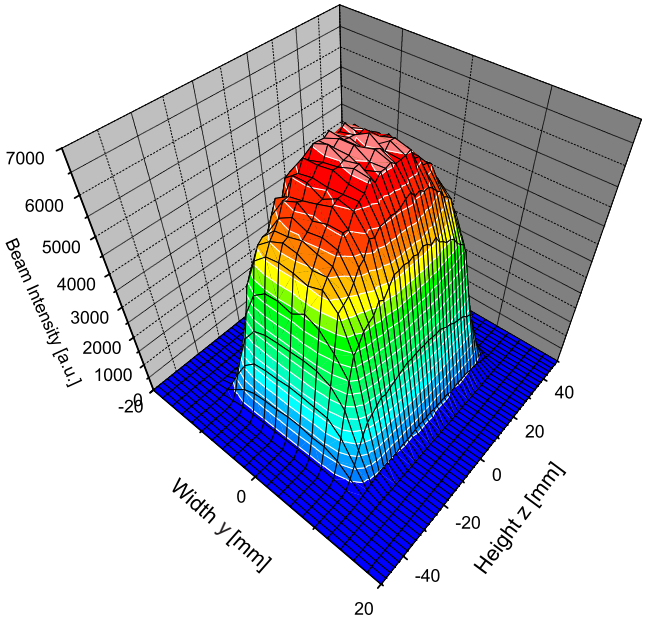

Figure 2.8: Simulated neutron beam profile in the decay volume.

averaged over intervals of 30 s, had a relative standard deviation of 3×10^{-3}. In addition, the neutron beam profile was measured at the exit window of the spectrometer with a neutron camera [Mue05] (see Fig. 2.7). A reasonable agreement with the simulated profile of the neutron beam in the decay volume was found (see Fig. 2.8).

2.4.2 Magnetic field design

In aSPECT, the magnetic field is used for two reasons: to guide the decay protons longitudinally to the detector and to convert (within the adiabatic approximation) the transversal into the longitudinal proton momentum component before the proton reaches the analyzing plane. To accomplish these purposes, a coil system has been designed, which provides variable magnetic field strengths along the spectrometer, while being axially symmetric. The position of the coils is shown in Fig. 2.11 (page 48). Details about the magnetic field calculations and coil design can be found in [Glü05].

The magnet was manufactured by Cryogenics Inc. and consists of a set of nine superconducting coils of NbTi. The number of windings differs from one coil to another. The coils are placed inside a cylindrical cryostat of three meters heigth and seventy centimeters of diameter (see Fig. 2.10). This cylinder contains a twenty centimeter diameter axially centered bore and is kept at a temperature of about 50 K. The coils are placed on the outer side of the bore tube, which is thermally insulated and kept at about 5 K. The insulation vacuum in the same cavity is of about 10^{-4} mbar. The pressure in the main vacuum chamber, located in the inner part of the bore tube is of about 10^{-9} mbar in operating conditions.

There are six openings providing access to the main vacuum chamber (see Fig 2.10).

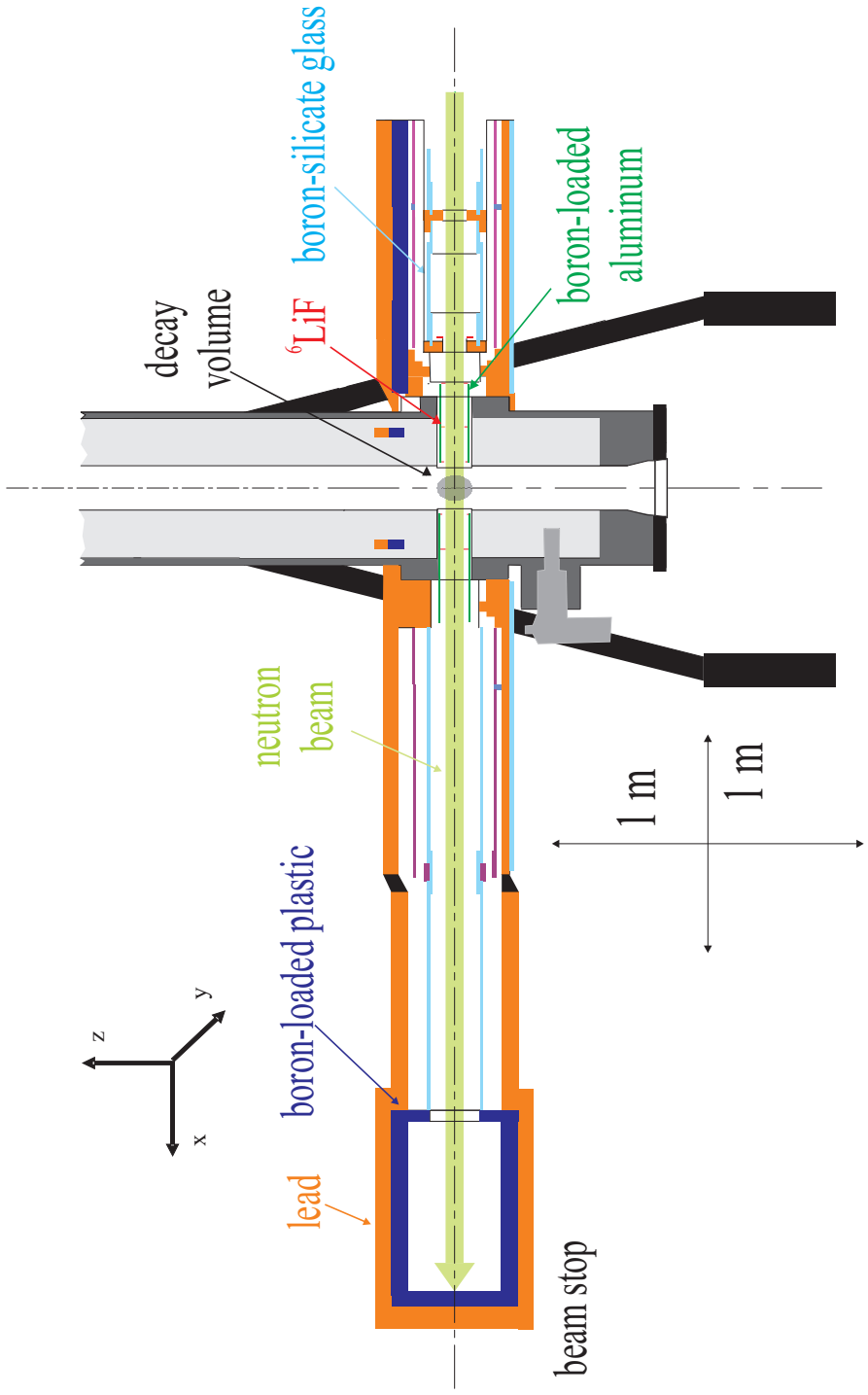

Figure 2.9: Schema of the neutron beam line mounted across the *a*SPECT spectrometer. Details of the collimation system are shown.

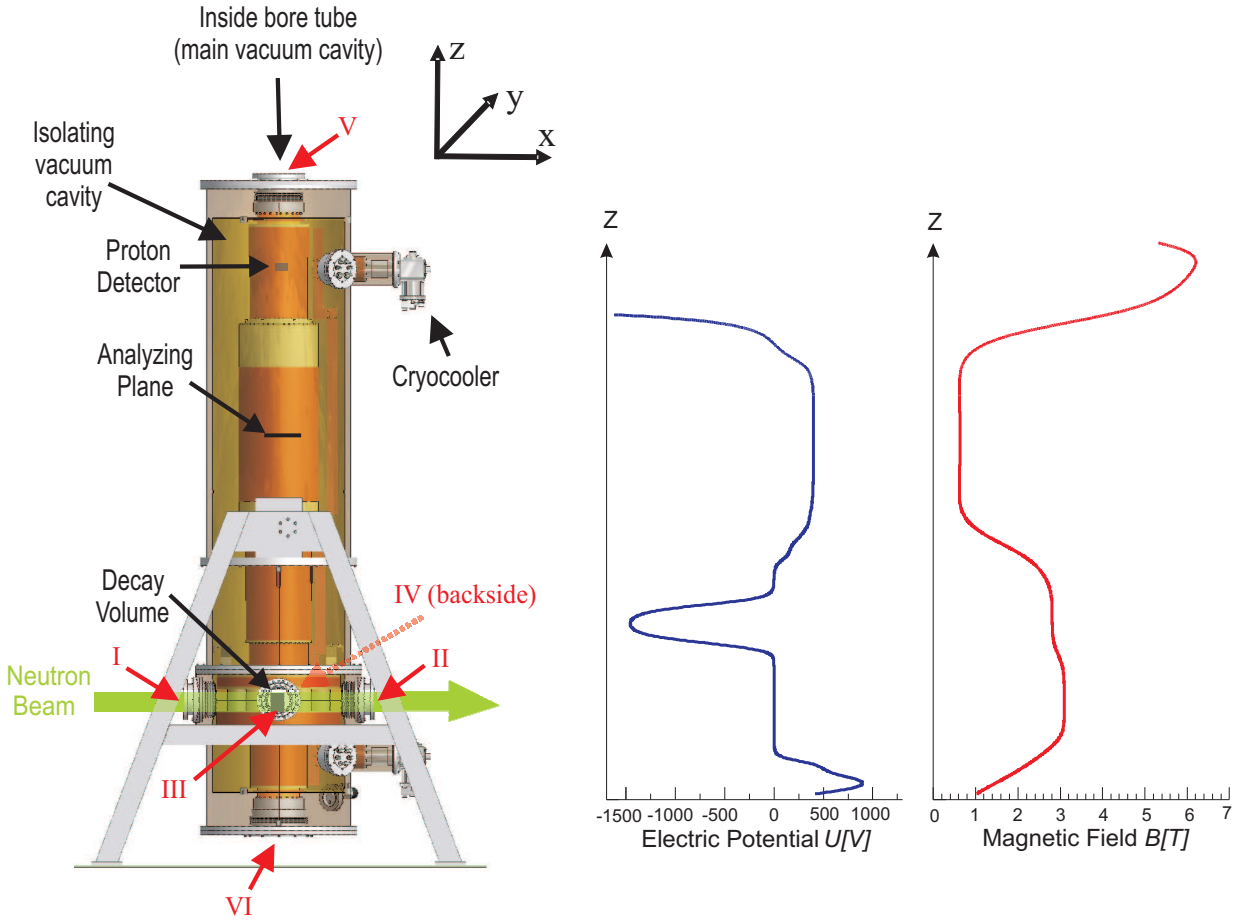

Figure 2.10: Sketch of the aSPECT spectrometer together with a calculation of the magnetic and electric field profiles at the axis. The six openings to access inside the bore tube are indicated.

Four of them are at the decay volume height (I to IV) and are used for the vacuum pumping system and as entrance and exit for the neutron beam. The other two accesses to the main vacuum are on both ends of the cylinder. The upper entrance (V) is used to introduce the proton detector into the spectrometer whereas the electrode system is placed into the main vacuum through the lower entrance (VI).

The cryostat is cooled down by two cryocoolers of type Sumitomo RDK408D. Each cryocooler has a cooling power of 35 W at the first stage (of about 70 K) and of 1 W at the second stage (of about 4 K). The temperature at the coils and bore tube is continously controlled by 20 temperature sensors located along the spectrometer.

Before to ramp the magnetic field, the insulating vacuum has to reach a pressure of about 10^{-4} mbar and the main vacuum to a pressure of at least 1×10^{-7} mbar. This process requires about 6 days of vacuum pumping. Once the main vacuum has reached the suitable pressure, the system can be cooled down. The cooling process takes about 120 hours. Using liquid nitrogen for pre-cooling, the overall cooldown time can be reduced to less than 80 hours. Once the cooling down process is completed, about 1.5 hours are needed to ramp up the coil current to 50 A. The process of warming up takes approximately 3 days. In an emergency case, this period can be reduced to 2 days by inserting nitrogen gas.

Except coils $c5$ and $c6$ which have different power supplies, the rest of the superconducting coils are connected in series to keep a constant magnetic field ratio between the different regions of the spectrometer by avoiding possible current fluctuations. This is important because the transmission function depends on the ratio B_A/B_0 (see Eq. 2.23).

The coil wire has a cross-section of 0.39 mm^2 and allows a maximum current of 100 A. Setting the maximum current to the coil system (i.e. applying 100 A) applies a magnetic field of about 3 Tesla in the decay volume region, about 0.6 T in the analyzing plane and about 6 T in the detector region (see Fig. 2.10). However, during our measurements the applied current was never set beyond 70 A. First, because the systematic effect due to non-adiabatic proton motion is negligible above 50 A [Glü05]. Second, to provide a secure operation temperature of the spectrometer[6].

The volume created by the magnetic field lines connecting the effective decay volume and the proton detector is called *flux tube*. However, the dimensions of the detector and of the diaphragm placed on top of the decay volume electrode $e3 - e6$ (see Fig. 2.11) limit the flux tube size on the directions parallel and perpendicular to the neutron beam.

For assuring the same magnetic field ratio B_A/B_0 (i.e., a unique transmission function) to all decay protons, a homogeneity of the magnetic fields of about 10^{-4} is necessary in the decay volume and analyzing plane regions [Glü05]. Otherwise, the probability that a proton overcomes the barrier potential would depend, besides on the proton energy, as well on the neutron decay position at the decay volume and on the proton position at the analyzing plane. Furthermore, the magnetic field homogeneity in the region of the dipole electrode $e8$ (see Fig. 2.11) must be also high enough to keep the proton trajectory adiabatic even when applying a large potential difference.

Between the decay volume and the analyzing plane, the magnetic field has been designed to have a maximum at $z = 0$, and to decrease monotonically and continously towards the analyzing plane without presenting any local minima. However, some decay protons with momenta almost perpendicular to the magnetic field originated between the maximum magnetic field B_0 and the mirror electrode can not reach the analyzing plane region due to magnetic mirror effect at $z = 0$. The superconducting correction coils $c5$ and $c6$ are used for a fine positioning of the maximum of the magnetic field in the decay volume, B_0. They can produce a magnetic field gradient along the symmetry axis of up to 1% of the main field and are powered independently from the rest of the coils. This gradient provides also a shift of the magnetic field maximum towards the bottom of the electric mirror electrode in order to avoid the magnetic mirror effect mentioned before.

The magnetic field at the analyzing plane region has been designed to have a local maximum at the center of the electrode $e14$, where the electrostatic potential applied U_A is almost uniform. Within the adiabatic approximation, this local maximum defines more accurately the position of the analyzing plane, maximizing in this way the resolution of the transmission function [Glü05]. However, during magnetic field measurements it was observed a shift of this local maximum of about 9 cm from the position where the potential barrier is applied towards the detector. To shift the maximum to its required position, an

[6] A slightly increment of the coil temperature was observed when increasing the magnetic field applied. The probability that the coil wire switches from the superconductive to the resistive state is then bigger.

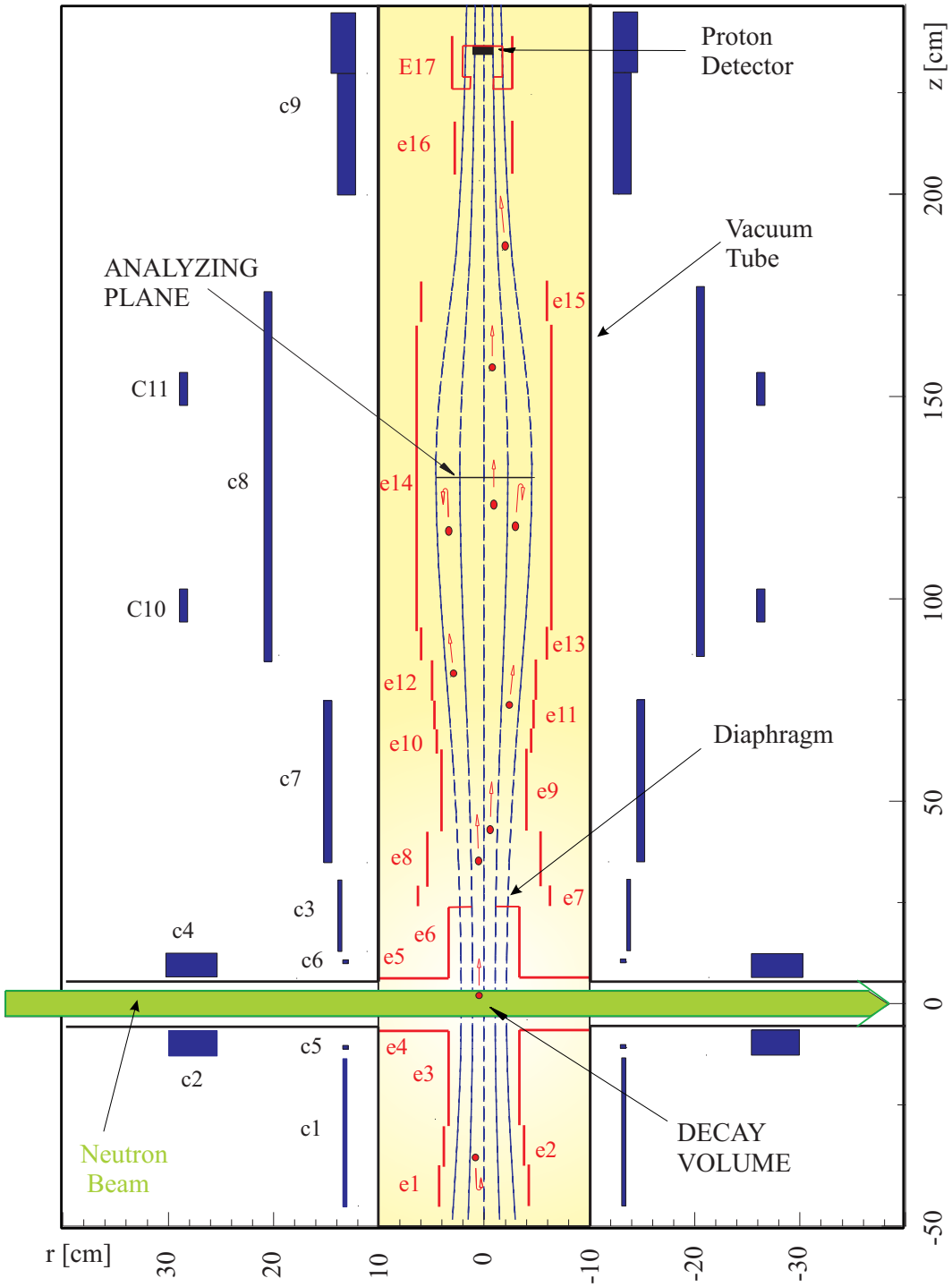

Figure 2.11: Scheme of the electrodes and magnetic coils in aSPECT. Many different coils and electrodes are necessary to keep the changes of the electromagnetic fields sufficiently small in order to apply the adiabatic approximation.

additional pair of non-superconducting correction coils, $c10$ and $c11$, are placed outside of the cryostat, at the height of the analyzing plane.

Magnetic field measurements

The coil system was designed with the aim to deliver a magnetic field that allows the measurement of the angular correlation coefficient a with an accuracy of $\delta a \approx 3 \times 10^{-4}$. In order to check if the shape of the magnetic field fulfills the expected design properties, a measurement of the magnetic field along the spectrometer axis is required, including a detailed study of the magnetic field homogeneity at the decay volume and analyzing plane regions.

At the required level of precision, also the influence of the environmental conditions on the magnetic field shape can be significant, e.g. the effect of an external magnetic field produced by magnetic materials around the experiment. So, for each apparatus location new magnetic field measurements are needed, as well as after a quench[7], when the superconducting coils might be damaged and/or moved due to large mechanical forces. However, on-line magnetic field measurements during data-taking would be most suitable in order to detect changes in the environmental conditions[8].

Measurements of the magnetic field were performed before starting the data acquisition during our beam times at the FRM-II in Munich. To carry out those measurements an inverted non-magnetic dewar is placed inside the cold bore tube after removing the electrode system. The dewar provides a suitable room temperature environment for a Hall probe, used for the magnetic field measurements.

A Hall probe manufactured by Group 3 Technologies, model MPT-141, was used. The working principle of the probe is based on the Hall effect and the measurement is temperature sensitive, since the charge carrier density in the semiconductor is temperature dependent. However, within its temperature operation range (from 0 to 50 °C) the output reading is temperature corrected. A detailed description of the Hall probe and its use in aSPECT can be found in [Aya05].

The Hall probe is mounted in a cylindrical plastic holder which is attached to a stainless steel rod with a length of 3 m. The diameter of the plastic cylinder fits into an aluminum tube mounted inside the dewar on the spectrometer axis. In order to get radial stability, the aluminum tube is fixed at three positions of the dewar tube: at the bottom, at the center, and at the top. The aluminum tube can be mounted on axis but also parallel to the axis, at a distance of 1.5 cm and 3.5 cm from the axis. The Hall probe, together with the holder, is positioned along the aluminum tube by means of the 3 m rod. Typically, magnetic field measurements are performed in steps of one centimeter. In addition, the probe's holder can be rotated, allowing a study of the spatial homogeneity of the magnetic field in 3-dimensions.

[7] A quench occurs when a part (and finally all) of the superconducting coil enters the normal conducting state.

[8] A NMR online system is under way. Its development and first tests will be included in the PhD thesis of Fidel Ayala Guardia [Aya11].

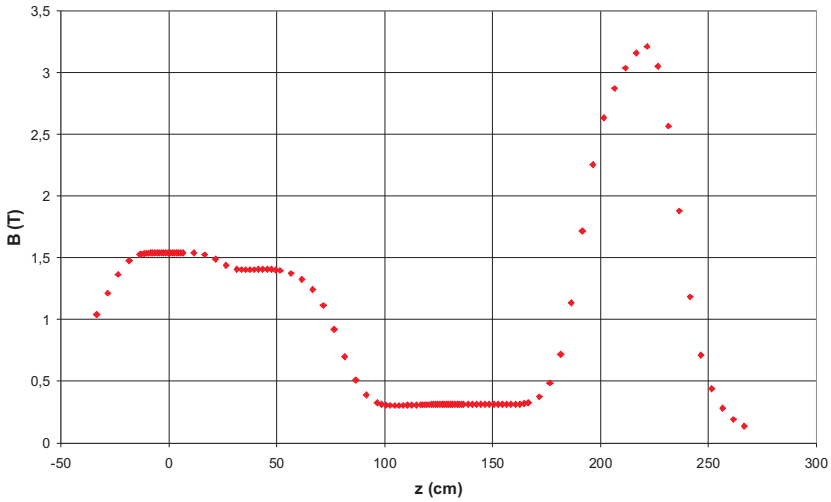

Figure 2.12: Magnetic field profile measured along the z-axis at 50 A. Please note that the Hall probe calibration ends at 2.2 T.

To minimize environmental magnetic field variations in the probe, the magnetic field measurements were carried out consecutively, during the smallest possible period of time. As well, series of magnetic field measurements were repeated at different times and in different order with the coils in the persistent current mode.

In Fig. 2.12 is shown the result of the magnetic field measurements along the spectrometer axis for a coil current of 50 A. All magnetic field gradients were found to be as expected from the calculations, ensuring an adiabatic proton motion.

Fig. 2.13 and 2.14 show in detail the results of the measurements performed in the decay volume and analyzing plane regions, on-axis and off-axis, respectively. The off-axis measurements are averaged over the azimuthal angle. The variation of the magnetic field values in the analyzing plane is found to be:

$$\frac{\Delta B_{A,max} - \Delta B_{A,min}}{B_A} = 1.7 \times 10^{-4} \tag{2.24}$$

while the variation in the decay volume is:

$$\frac{\Delta B_{0,max} - \Delta B_{0,min}}{B_0} = 2 \times 10^{-3} \tag{2.25}$$

The average magnetic field in the decay volume at 50 A is $B_0 = 1.5420(5)$ T, when averaging over the magnetic field profile in this volume and weighting it with the neutron beam profile. The average magnetic field in the analyzing plane is $B_A = 0.31272(10)$ T. The main contributions to the uncertainties of these magnetic field values are the uncertainty in the knowledge of the neutron beam profile and the uncertainty in the calibration of the Hall probe. The average magnetic field ratio obtained is $\mathrm{r}_B = B_A/B_0 = 0.20280(9)$.

Once the magnetic field measurements were over, it was found out that the super-

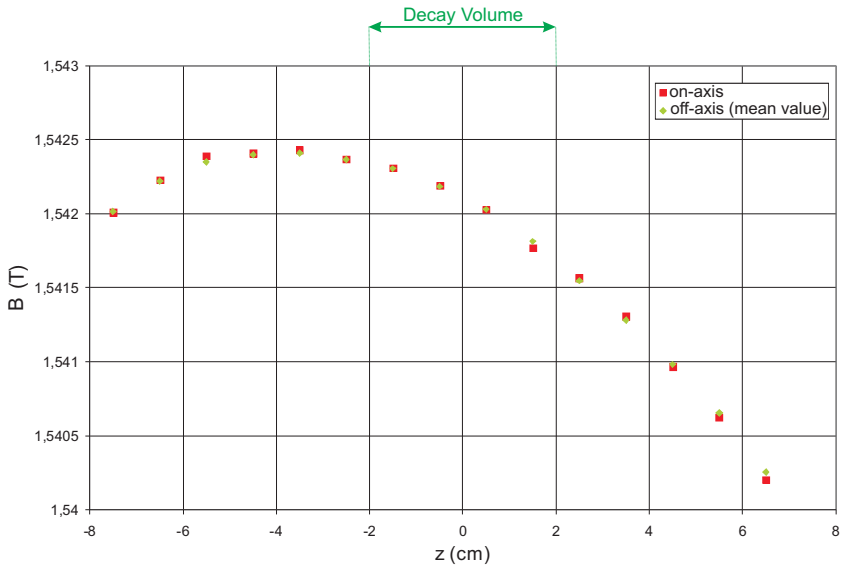

Figure 2.13: Magnetic field profile zoomed at the decay volume region measured on and off axis with a coil current of 50 A. Off axis values are averaged over the azimuthal angle.

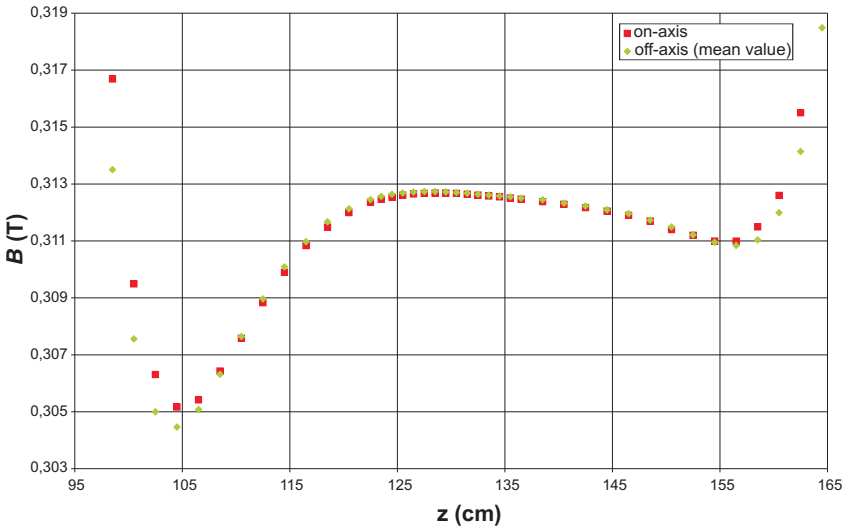

Figure 2.14: Magnetic field profile zoomed at the analyzing plane region measured on and off axis with a coil current of 50 A.

conducting magnet shows a hysteresis in its current-field characteristic, which is a known effect, especially in magnets employing niobium-titanium (NbTi) superconducting coils (see [Sco68]). Persisting currents in the superconducting coils even at zero nominal current cause a small magnetic field once they were switched on before. This remaining field is not homogeneous. It has an average strength of 0.3 mT in the decay volume and in the analyzing plane. When warming up the coils above their critical temperature ($T_{crit} \approx 9$ K) the remaining field disappears. Therefore, an extra uncertainty must be introduced to take into account the possible difference between the off-line magnetic field measurements and the magnetic field during the data-taking process. Besides the hysteresis, this extra error includes as well uncertainties due to changes in the environment and to the non-reproducibilities in settings and position of the correction coils. Taking into account these corrections, the definitive value of r_B reads:

$$r_B = 0.2028(3) \tag{2.26}$$

2.4.3 Electric field design

In the scheme of Fig. 2.11 the position and the length of the electrodes along the z-axis are shown. A photograph of the whole electrode system is shown in Fig. 2.15. Most of the electrodes are cylinders made from OFHC copper, a high conductivity material suitable to work under ultra high vacuum conditions. They are electrolytically coated with a 2 μm layer of silver, followed by a 1 μm layer of gold to assure constant work functions on their surfaces. The high number of electrodes used follows from the need to keep electric field changes small in order to use the adiabatic approximation [Glü05]. The characteristics and functionalities of some of the electrodes are the following:

- **Mirror electrode (*e1* and *e2*):** Electrodes $e1$ and $e2$ are used to reflect, within the adiabatic approximation, all decay protons emitted in the lower hemisphere. Typically, electrode $e2$ is set at +500 V and $e1$ at +1 kV.

- **Decay volume electrode (*e3* to *e6*):** The shape of these three electrodes can be seen in Fig. 2.16. This electrode is one piece made of three different shaped electrodes. All three parts together form a cylinder of 60 cm height and 3 cm diameter with four rectangular apertures perpendicular to the z-axis. The *decay volume* defines the active volume of decay protons that reach the detector when the barrier voltage U_A is set at 0 Volt. This volume is found at the center of the decay volume electrode with dimensions $8 \times 2.8 \times 3.5$ cm^3. These dimensions are defined by the collimation system and by the diaphragm placed on top of the electrode $e6$, consisting of two aluminum foils with a thickness of 12 μm, mounted 2.5 cm apart. The electrodes $e3 - e6$ are kept at ground potential to shield the decay volume from the electric fields of the other electrodes. Within the decay volume the electrostatic potential has been calculated to be smaller than 1 mV [Glü05], which is well within the tolerance to measure the parameter a with an accuracy of 3×10^{-4}. However,

in these calculations the possibility of proton reflection and proton trapping processes in the decay volume were not taken into account (see Pag. 41 for more detail).

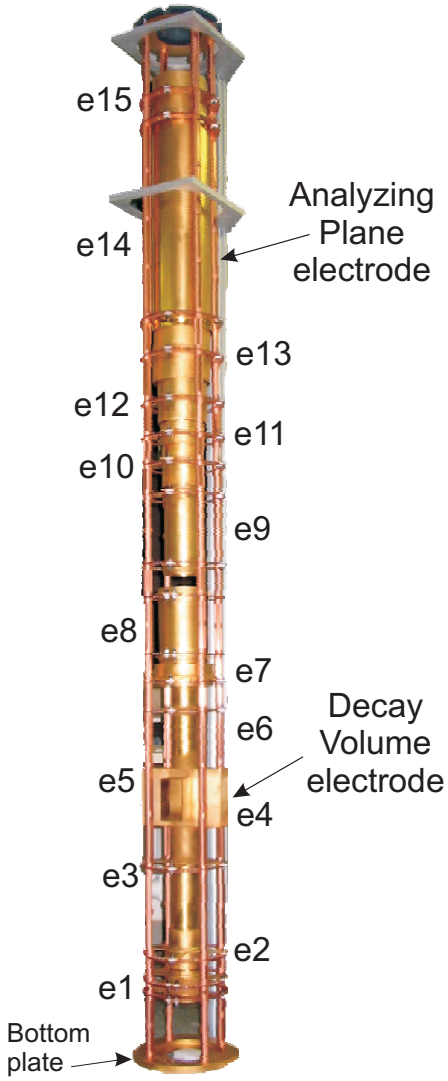

Figure 2.15:
The electrode system.

- **Lower $E \times B$ (*e8*):** This is a dipole electrode manufactured by two half-cylinders held at different negative potentials which produce an electric field perpendicular to the neutron beam. Consequently charged particles traveling through it are shifted, in first approximation, along the neutron beam direction. Its main function is to remove the protons that can not pass the analyzing plane and instead remain trapped between the electrostatic mirror and the analyzing plane. The effect of the $E \times B$ drift is independent of the direction of the proton motion through the dipole electrode. After several passages through the electrode they will be removed. Applying a higher voltage the number of passages needed to remove the protons decreases. In this way, protons can be removed faster, reducing the probability that they collide with the residual gas molecules. However, calculations show that to keep proton trajectories to an acceptable adiabatic limit, the potential difference between both dipole sides must not exceed -3 kV [Glü05]. A picture of the lower E×B electrode is shown in Figure 2.17.

- **Analyzing plane electrode (*e14*):** It is the largest electrode of the whole electrode system and the only one with electro-polished surface. This electrode defines the value of the potential barrier, where a voltage U_A between 0 and +800 V is applied. In order to keep the changes of the electric field adiabatic, additional electrodes $e10$ to $e13$ and $e15$ are used, which are held at a constant fraction of the applied analyzing plane voltage.

- **Upper $E \times B$ (*e16*):** It consist of two parallel stainless steel plates with a surface of 10×10 cm^2 separated 4 cm apart. This dipole electrode produces an electric field along the neutron beam axis. Its potential difference causes a drift to the proton trajectory perpendicular to the neutron beam axis. This shift is

used to center the proton beam onto the detector in order to minimize edge effects (see Chapter 3). But the main function of this electrode is to accelerate the protons in order to overcome the high magnetic field applied at the detector region. Typical voltage values used on the dipole during the beam time were -2 kV / -4 kV.

- **High voltage electrode (*e17*):** This electrode is placed just before the proton detector and is held at -30 kV in order to get a detectable proton signal. It consist of a stainless steel cup-like shape with 40 mm inner diameter. Its walls are filled with lead to reduce gamma radiation background on the detector signal.

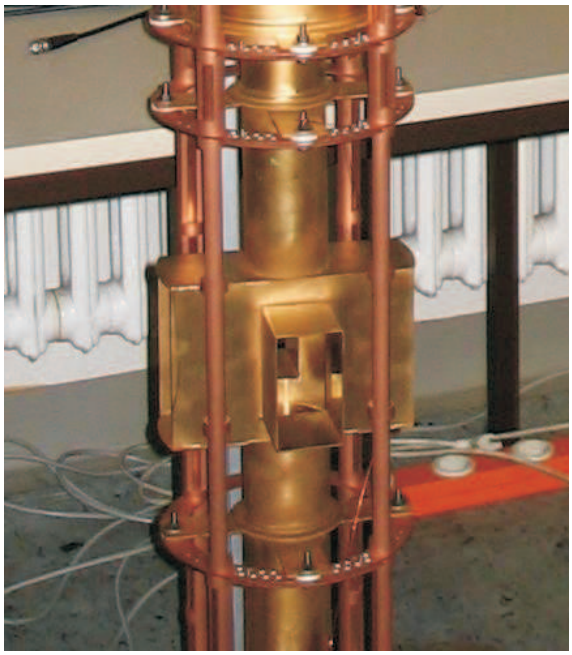

Figure 2.16: Decay volume electrode, *e3-e6*

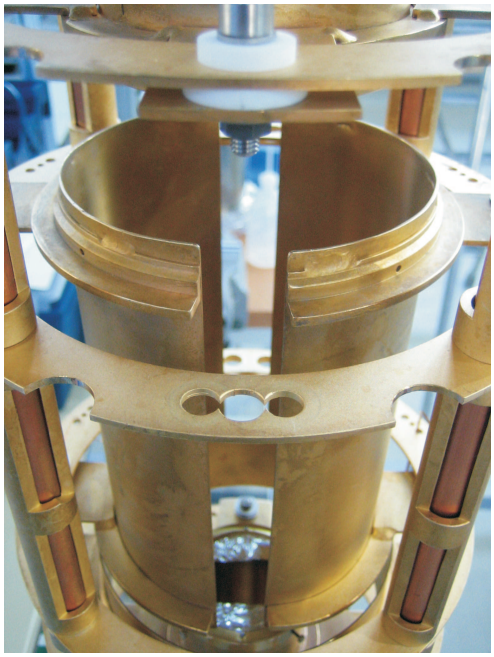

Figure 2.17: Lower E×B electrode, *e8*

2.4.4 Mounting of the electrode system

The set of electrodes forming the electrode system are held together by 4 rods, at the time fixed to the bottom flange of the electrode system (see Fig. 2.15). Dedicated rings with holes hold the electrodes along the rodes. These rings are separated by hollow cylinders (see Fig. 2.18). All 4 rods, the rings and the cylinders have been as well manufactured from OFHC copper and are held at ground potential. Additionally, the rings have been, like the electrodes, first silver- and then gold- coated. The whole system stands in the laboratory in vertical position to avoid bending of the 4 rods due to the weight of the electrode system itself. However, for transportation or storage a wooden box has been used that keeps the electrode system in horizontal position while supporting its weight in several points.

Before mounting, the whole electrode system has been cleaned piece by piece in an ultrasonic bath. First with normal soap and afterwards with isopropanol.

The wiring of the whole system is a delicate issue. In case of failure of only one wire the potential applied to the affected electrode is not defined. Then the adiabaticity can be lost and reparation is needed. If this occurs during an *a*SPECT beam time it implies the dismounting of the complete experiment, resulting in a delay of several weeks. Electrodes at low voltages (i.e. up to 1 kV) have been connected through pure OFHC copper wire, whereas Kapton-insulated wire has been used to connect electrodes held at higher voltages, like the lower E×B electrode. Pure OFHC copper wire connects each electrode to the bottom flange following a quite straight path. The wire crosses the rest of the rings through little holes protected and surrounded by Macor insulators. These wires are connected to the same section of the bottom flange in order to have them safely grouped and controlled when introducing the electrode system into the cryostat. The connection from the bottom flange of the electrode system to the bottom flange of the cryostat is done by Kapton-insulated wires which are connected to an in-vacuum 19-pin feed-through.

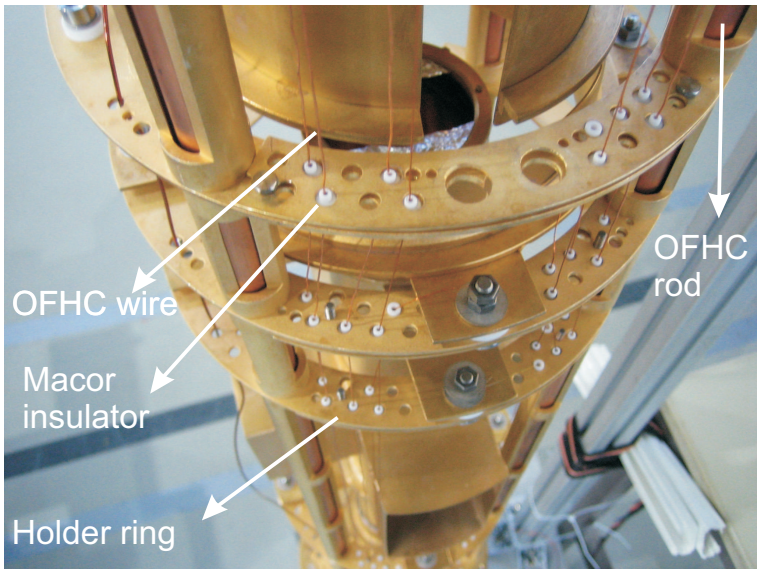

Figure 2.18: OFHC copper rings that fix the electrodes in place. The wires that connect to the electrodes cross the dedicated holes in the rings.

Each electrode has been connected by means of one wire except for the decay volume electrode and the analyzing plane electrode which had two connections in order to measure their voltages precisely.

During the *a*SPECT beam times performed at the FMR-II in Munich only one cabling incident occurred. It took place during the first beam time, when a short-cut between two electrodes was produced due to mechanical instabilities of their wires in the in-vacuum 19-pin feed-through connections. After repairing it, the wiring system worked perfectly during the rest of *a*SPECT beam times. However, from the experience gained during the wiring procedure of the electrode system, it has been found out that its risk of failure can be reduced introducing some changes. One of them is the exchange of the pure OFHC copper wires for Kapton-insulated wires since it has been checked that such exchange does not reduce the quality of the vacuum. One advantage is that insulated wire needs to use less Macor insulators, which turned out to break easily when applying some force on them, for example when introducing the electrode system into the cryostat. In addition, in

case an insulated wire disconnects or breaks inside the cryostat the probability to produce a short-cut is strongly reduced compared with the use of non-insulated wires. Another improvement can be achieved by installing two wires for each connection instead of one. Then, in case one of the wires fails due to bad contact with the electrode (e.g. due to contraction of the copper wire because of low temperatures) a second wire can be used.

2.4.5 Electrode system: calibration issues

The barrier voltage applied to the protons at the analyzing plane, $U_A - U_0$, was measured with a precise multimeter Agilent 3458A, which has a temporal stability better than 5 mV in the 1000 V scale. After the beam time, it was found that the multimeter was not perfectly calibrated, being off by $\Delta U_A/U_A = 3 \times 10^{-5}$. However, the accuracy of the experiment is not limited by this uncalibration.

The voltages at the decay volume, U_0, and at the analyzing plane, U_A, are monitored at the surface of these electrodes by means of a cable connection. Variations of the work function within one electrode, or between different electrodes would render the voltage difference $U_A - U_0$ uncertain despite the multimeter measurement.

One way of eliminating this uncertainty would be the implementation of a monochromatic particle source with which the potential difference $U_A - U_0$ can be directly measured. However, the development of a precise monochromatic electron source (maximum energy spread of 10 meV) showed to be difficult since it has to operate in strong magnetic fields as well as in ultra high vacuum. The electron source was based on the idea that the energy of photo-electrons is given by the energy of the photons minus the work function, which turned out to be not suitable due to the difficulty of obtaining gold surfaces with a sufficiently homogeneous work function.

To estimate the homogeneity of the work function in our electrode system, after the beam time a measurement in cooperation with KP Technologies Inc. was performed. The homogeneity of the work function in one cylindrical sample electrode was measured with a Kelvin Probe[9]. With such a Kelvin Probe, changes in the contact potential difference between a reference material and a sample can be measured to less than 5 mV accuracy. The result of this study showed a spatial variation of about 100 mV over a distance of several cm on the same electrode, see Fig. 2.19. If we assume this deviation of the measured voltage at the analyzing plane we would extract a value of the coefficient a with an error of about 1% [Glü05]. Although it does not constitute a problem for the level of accuracy achieved during the beam times analyzed in this thesis (see Chapter 4), this deviation is significantly bigger than the goal of the aSPECT experiment and has to be improved for future measurements of the coefficient a.

[9]The Kelvin Probe used was similar to the one discussed in [Bai98]

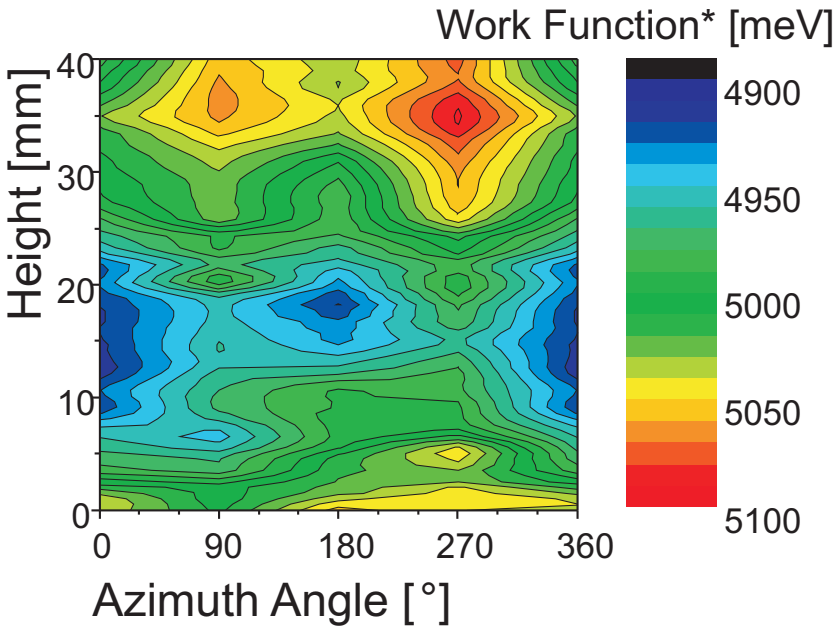

Figure 2.19: Spatial variation of the work function from one cylindrical sample electrode measured with a Kelvin Probe. Over a distance of several centimeteres, a variation of about 100 mV is observed.

2.5 Proton detector

The proton detector used in *a*SPECT at the FRM-II is a segmented PIN diode, custom built by Detection Technology Inc., Finland. Each detector is divided into 25 stripes with a surface area of 25 × 0.8 mm^2. A non-active region of 0.2 mm width fills the space between the stripes. In total, the detector has a size of 25.8 × 25.95 × 0.4 mm^3. In Fig. 2.20, a photograph of the detector and a detailed sketch of one corner of the detector are shown. The detector development was carried out by our collaborators from the Technische Universität München. For a detailed description of the *a*SPECT detection system References [Sim06] and [Pet07] are available.

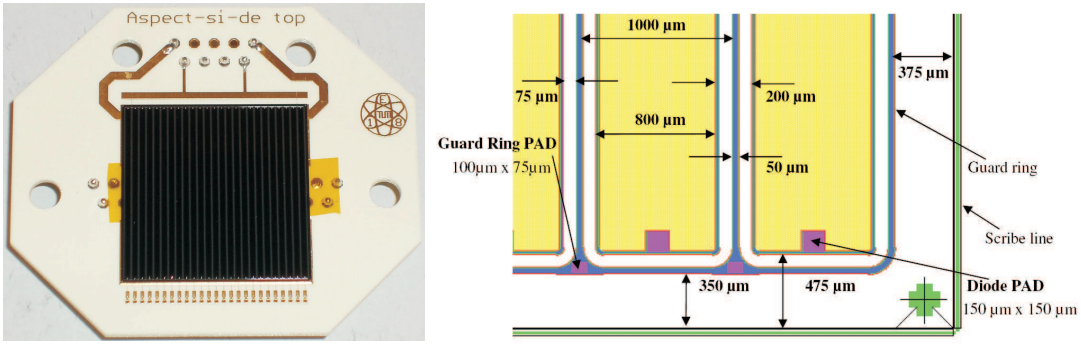

Figure 2.20: On the left side, a photograph of the detector mounted on a special gold printed circuit board is shown. On the right side, a scheme of one edge of the detector. The dimensions of the stripes and their separation are indicated. The guard ring prevents electrical breakthroughs once the detector is biased. Small aluminum pads at the end of the stripes are used to contact each strip individually.

The detector surface layer is a protective window with a thickness of 67 nm, consisting of 40 nm Si_3N_4 and 27 nm of SiO_2. Below there are three active layers (a total of 381 μm) in the following order: a p-doped layer of 0.5 μm thickness, an intrinsic layer of low n^--doped silicon with a thickness of 380 μm and a high doped n^+-layer of 0.5 μm. To contact the last layer, the backplane of the detector is covered with 0.7 μm of aluminum.

The detector is glued on a special gold printed circuit board (also shown in Fig. 2.20) suitable for ultra-high-vacuum (UHV), on which each stripe is separately connected by wire bonding to the board. For the read out we used one single standard 25 pin connector, while a 9 pin connector on the top of the board was used to provide the bias voltage.

A mechanical system allows the positioning of the detector inside the bore tube of the aSPECT spectrometer. An UHV gate valve allows an easy access to the bore tube[10]. The detector can be retracted behind the valve in case that maintenance is needed. The proton detector is mounted on a vacuum feed-through, on the bottom of a warm insert stainless steel tube which can be lowered into the magnet bore tube from the top.

A preamplifier board is placed inside the tube, close to the detector in order to reduce the pick-up noise. All, the detector, the electronics and the tube are held at high voltage. To isolate the high voltage parts from the rest of the experiment, a CF-35 ceramic insulator is used. A stainless steel cup around the detector (set as well at high voltage) is filled with lead to shield the detector from external background. The digital part of the electronics is placed outside, mounted on top of the whole setup. The cables to connect the preamplifier with the rest of the electronics are inside an acrylic glass tube (suitable for high voltage shielding purposes), which goes through the insulator. In addition, a flow of compressed air is introduced via a flexible tube to cool down the preamplifier region, and to assure that no water condenses on the inner surface of the insulator to avoid high voltage breakthroughs.

The whole detection setup is mounted inside two CF-160 T-pieces to which also the pumping system is connected (see Fig. 2.21). With the help of a crane the T-pieces can be placed on top of the spectrometer. Once the vacuum within this cavity is good enough (better than 1×10^{-7} mbar) the UHV gate valve can be opened in order to introduce the detector into the spectrometer using a little wagon running on three rods mounted inside the T-pieces.

The readout of the aSPECT detector consists of an analog and a digital part. The analog part is basically composed of a preamplifier/shaper combination plus line driver chips that transfer the signals via twisted-pair cables (of about 2 m length) to the digital part of the electronics, placed on top of the setup. The readout working principle is shown in Fig. 2.22. The signal from each detector-stripe (in the following called detector-channel) is digitized by an analog to digital converter (ADC) with a resolution of 12 bits. From the 32 ADCs, 25 are used to process the detector-channels and two more to process temperature sensors. The rest of ADCs are not used. The sampling frequency of each ADC is 20 MHz, which results in a time resolution of 50 ns. Directly connected to the ADCs outputs are two field programmable gate arrays (FPGAs) which are used to analyze

[10]If the detector installation would be fixed inside the spectrometer, in case of reparation, the experiment should be stopped for about two weeks. That is the time needed to warm up and cool down the cryostat.

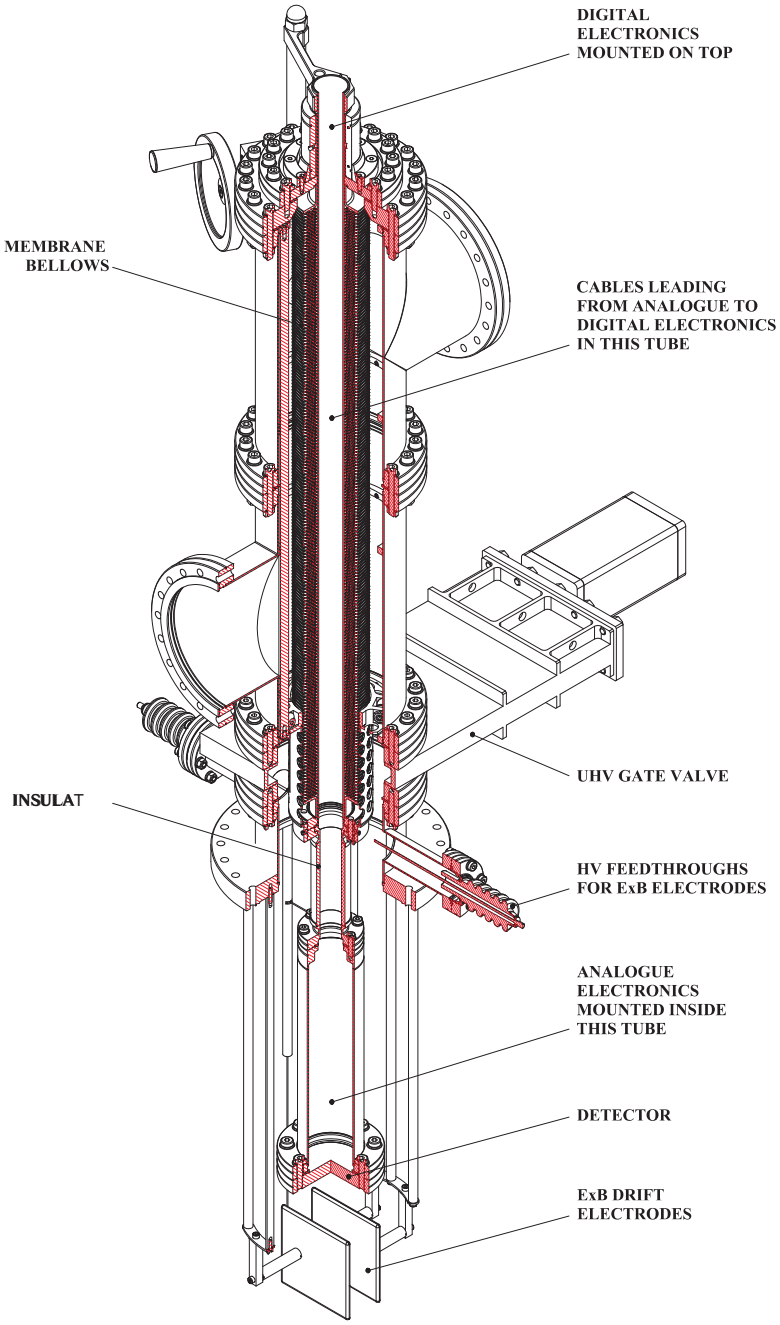

Figure 2.21: Mechanics used to place the *a*SPECT detector inside the cryostat.

and preselect the raw data sent to the computer. The FPGAs are sampling all the time and the signals are shifted through time-bins of 50 ns.

Data from each detector-channel is stored in the FIFO-memory, which has a total storage capacity of 1024 words. The length of one word corresponds to 12 bits, i.e., the length of one data word from the ADC. This means that in the FIFO-memory between 7 and 12 events can be saved, depending on the chosen event length. During the beam time we used event lengths of 100 bins (5 μs) and of 128 bins (6.4 μs). A multiplexer running with the same clock as the ADCs, pulls events from each ADC output in turn. The time needed to cycle through the outputs of all ADCs is maximum when each detector-channel has data to be processed, which at the same time depends on the event length. Meanwhile the data rate is less than 20 kHz per ADC, no event will be lost. In FMR-II, the expected data rate taken with *a*SPECT is in the order of 1-2 kHz for all detector-channels (including the detection of protons and electrons).

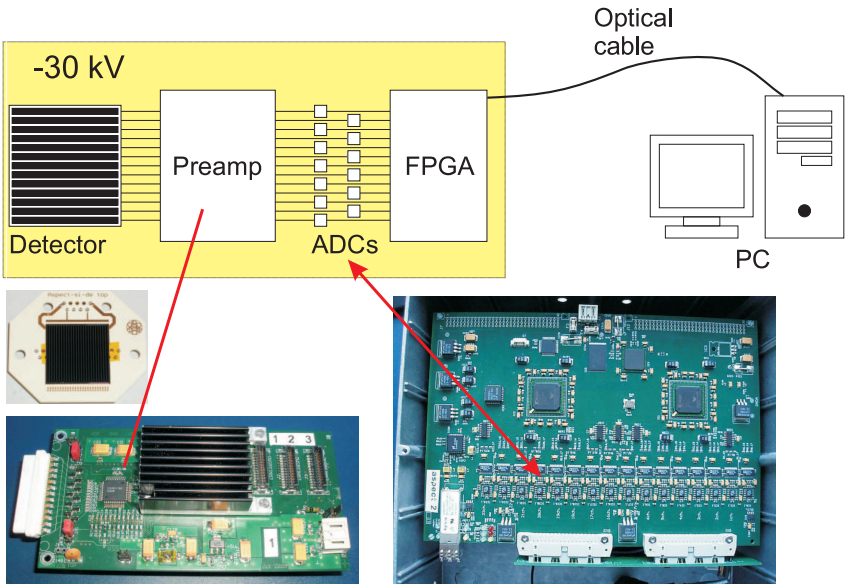

Figure 2.22: Sketch of the detection readout. The yellow box indicates all parts set at high voltage during the operation of *a*SPECT. However, only the detector and the preamplifier box are situated inside the cryostat. The board containing the ADCs and FPGAs is mounted outside.

To discriminate event-pulses, the stored signals are analyzed with an algorithm illustrated in Fig. 2.23. The FPGA determines the mean value of the signal height (i.e., the ADC reading) within two time windows, *window 1* (W1) and *window 2* (W2). Window 1 has a length of about 25 μs, much longer than a typical event length, whereas window 2 is shorter than the length of one event. We used W2 sizes of 0.8 and 1.6 μs. The starting point of W2 is always 16 bins (0.8 μs) later than W1. The ADC data is shifted continuously through the time-bins and discarded at the end if no pulse was detected. During this process, the average of the ADC reading on W1 and W2 is continuously updated. When the difference (in ADC channels) between the average reading of W2 and W1 is higher

than a programmed *threshold* during a defined number of bins in a row (known as *delay*, usually set to 3 bins), the event-pulse is recorded. In order to obtain the full shape of the event-pulse, a few bins before the position where the pulse was detected (known as *buffer*) are saved too. Once a pulse has been detected in one detector-channel it is not possible to trigger another pulse in the same detector-channel within the time interval of the event. Thus, the minimum time needed to detect another event in this detector-channel is the length of one event.

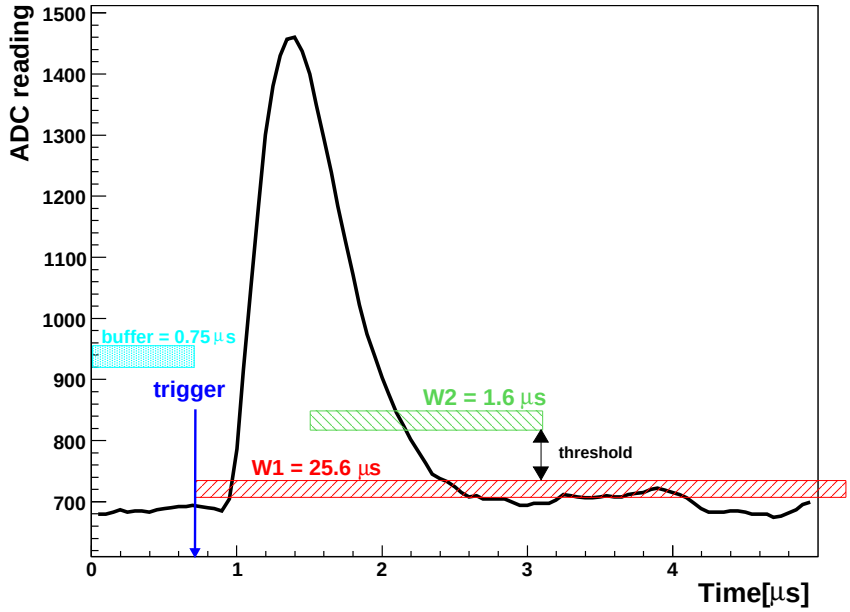

Figure 2.23: Example of event-pulse detected with the used trigger algorithm. The averaged ADC-reading of window 1 (W1) and window 2 (W2) is continously taken. At each new measurement both windows are shifted one time-bin (50 ns). If the reading difference between W2 and W1 is higher than a programmed threshold during three bin positions in a row, the event-pulse is recorded. The recorded signal contains 0.8 μs before the trigger position.

Besides pulse detection, the system can be additionally programmed to send out data in regular intervals, the so-called *heartbeats*. These events are used to obtain information from temperature sensors installed in the detector setup. The read-out of the detector as well as the control of the detector parameters is done via optical cables to a DAQ-computer, from which LabView programs permit bi-directional communication. Both boards, the one containing the preamplifier and the one containing the ADCs and FPGAs, are put on the same high voltage. The latter board is mounted inside a metal box (to prevent discharges) which then is installed into a larger Plexiglas box for isolation.

During the main data-taking period two of the segmented PIN diodes were used. Both were energy calibrated in order to obtain the relation between the pulse height of the signal (the electronic output) and the energy deposited in the active layer of the detector. For this purpose radioactive γ sources were used. Pulse height spectra were taken from ^{133}Ba (81 keV), ^{241}Am (60 keV), and ^{57}Co (122 keV) calibration sources. A linear relation between the pulse height and deposited energy was found [Sim06]:

$$Pulseheight = (-2.2 \pm 2.4) + (3.32 \pm 0.07) E_{dep} \tag{2.27}$$

where E_{dep} is the energy in keV deposited in the active layer of the detector. From Eq. 2.27 the energy E_{dep} can be inferred for any given pulse height. Therefore, since the initial energy of the decay protons is known, the energy loss in the entrance window can be calculated. For protons with an impact energy of 30.4 keV (that is, the average energy of a proton from free neutron decay plus 30 kV from the applied acceleration voltage) the energy loss in the dead layer was measured to be 5.8 keV. With a standard deviation due to energy straggling[11] of 0.9 keV. This value is a bit smaller than the energy loss predicted by simulations performed with the SRIM-2006 program [Zie06], which gave a value of 7.5 $\pm$ 0.4 keV for 30 keV protons. One possible explanation for this deviation is that the dead-layer of the detector is thinner than specified by the company.

When the proton detector is set at -30 keV, the protons that reach the detector have energies between 30 and 30.75 keV. If the detection efficiency would differ within this energy range, the count rates for different analyzing plane voltages would contain a systematic error. To study the energy dependence of the detector, simulations with SRIM-2006 showed that the relative difference in the detection probabilities of protons with initial energy of 30 keV and another with 30.8 keV is of about 3 $\times 10^{-4}$ [Pet07]. According to the simulations, only 0.3% of the protons are backscattered before they deposit enough energy in the detector to produce a signal. A possible effect due to energy dependent backscattering on the detector was also studied [Pet07]. The difference in backscattering probability between 30 and 30.8 keV was of about 8 $\times 10^{-5}$.

[11] The number of collisions required to bring a proton to rest inside the detector layers varies slightly for each proton within a range known as straggling.

Chapter 3

Data analysis

From July 2005 to May 2006, the spectrometer *a*SPECT was set up at the MEPHISTO beam-line at the FRM-II reactor in Munich, for a total duration of four beam times. It was the first time that the whole *a*SPECT setup was mounted together to perform measurements with neutron beam. Consequently, a big part of this period was spent sorting out different problems that could only be detected when the complete setup was tested at once.

In the first beam time the main problems arising were due to instabilities of the power supply system. As a consequence of this, only a little amount of data was taken. In addition, high voltage instabilities occurred at the detector system with sporadic breakdowns, which led to further complications.

Before the start of the second beam time, magnetic field measurements were performed in situ (see Section 2.4.2 for details) and the upper $E \times B$ electrode (electrode $e16$) was installed in the cryostat, which until this point had been missing.

During the second and third beam times a big amount of data was taken, although high voltage instabilities persisted with stronger and more frequent breakdowns. They were produced randomly, causing damage to the detector electronics (mainly to the preamplifier and/or the ADC-board) which sometimes (typically once per week) required reparation of up to three days. Nevertheless, the enhancement and adaption of the Data Acquisition software (DAQ) to the voltage power supplies, as well as the better automatization of the data acquisition procedure, allowed a slower and more controlled voltage application to the system, which reduced the probability of high voltage breakdowns to occur.

Even though the high voltage problems could not be solved completely, during the fourth beam time at FRM-II a reasonable amount of data was obtained, providing enough statistics to extract the coefficient a with a relative accuracy better than 5%.

This Chapter starts with the explanation of the data analysis procedure that is followed to extract the electron neutrino angular correlation coefficient a from raw data measured with the *a*SPECT spectrometer. First, the DAQ system and the data taking process is described. Thereafter, the different steps of the data analysis, from event pulses to the final integral proton spectrum, are discussed in detail.

3.1 DAQ system and data structure

The data acquisition (DAQ) system used in *a*SPECT is schematically represented in Fig. 3.1.

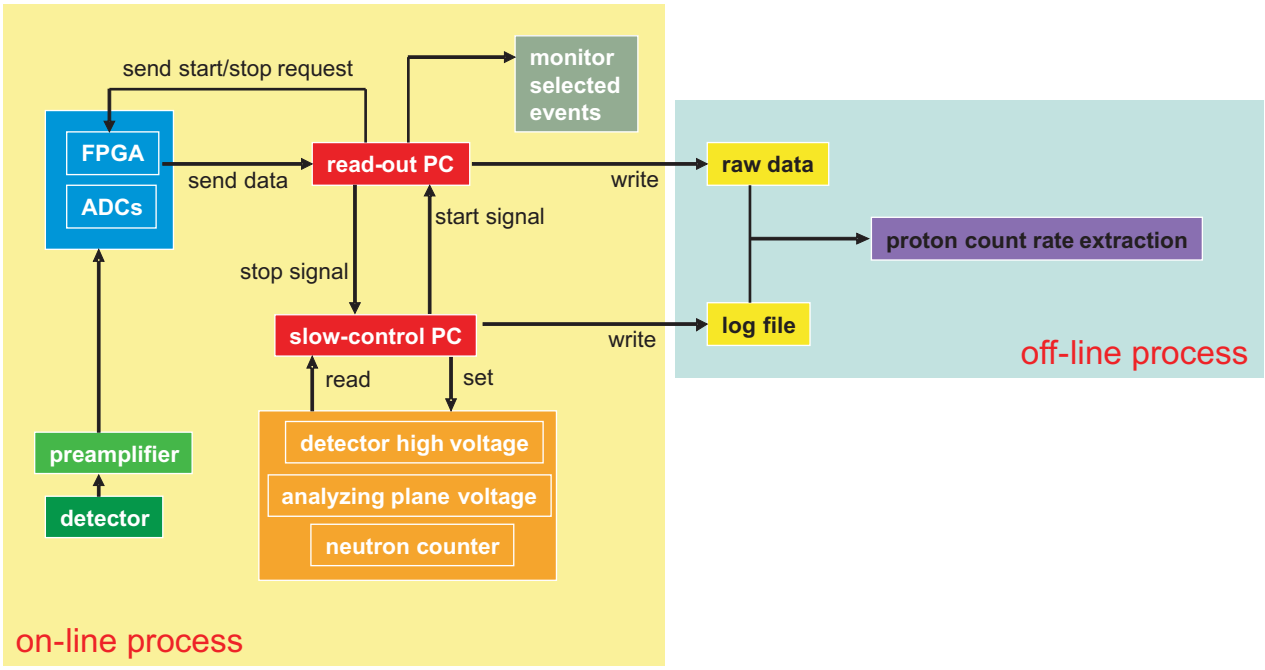

Figure 3.1: Scheme of the data acquisition system used in *a*SPECT. See text for details.

The measurement is controlled by means of two computers. The trigger algorithm (described in Page 60) can be configured with the *read-out PC* which will be applied to the data stored in the FIFO memory from the FPGA. All events detected are written in a raw data file with the following structural form:

SLINK header 1 (32 bits)		
SLINK header 2 (32 bits)		
SLINK header 3 (32 bits)		
ADC header (32 bits)		
timestamp (32 bits)		
unused (8 bits)	ADC data (12 bits)	ADC data (12 bits)
.		
.		
.		
unused (8 bits)	ADC data (12 bits)	ADC data (12 bits)
footer (32 bits)		

The sequences *SLINK header 1* (marked in orange) and *ADC header* (in blue) contain information about the event length, event type and detector-channel (a detailed structure of both sequences is shown in Table 3.1), whereas *ADC data* sequences give the ADC-reading information (in green).

INFORMATION SAVED	NUMBER OF BITS
1	1
type of event	5
id	10
event size	16

(a) Detailed structure of the first 32 bits saved from one event. They correspond to the *SLINK header 1* sequence

INFORMATION SAVED	NUMBER OF BITS
1	1
0000	4
1	1
1	1
overflow	1
000	3
detector-channel	5
00	2
10	2
event size	12

(b) Structure from the sequence *ADC header*, of 32 bits

Table 3.1: Detailed contents of the sequences *SLINK header 1* in a) and of *ADC header* in b).

The *slow control PC* monitors the start and several settings of the measurement cycles like the voltages applied to the analyzing plane, the detector and the upper $E \times B$ electrode. In addition, at the end of each measurement-cycle a log-file containing the filename of the raw data, the measurement time, the analyzing plane voltage, the high voltage and the reading of the neutron counter is written in one line.

The raw data needs to be decoded into a processable format. For that purpose, a single file containing all events taken in one measurement cycle is created. Each event is processed by means of a decode program[1] which stores several parameters characteristic of each event into a ROOT[2] tree: the timestamp, absolute time, detector-channel, maximum ADC value, baseline value, and an array with the ADC values of each event bin.

The timestamp provides the time for each event and has a length of 30 bits with respect to the start of the measurement cycle. Since 1 bit corresponds to 50 ns, the timestamp overflows every 53.7 seconds. To take this fact into account, during the decode process we store an array of events in memory and sort them in the right time order before they are written into the ROOT file. This sorting algorithm prevents that one event from one detector-channel with slightly higher timestamp can be written to disk before one event from a different detector-channel with slightly lower timestamp. In principle, the multiplexing nature in which the data is sent out by the digital electronics allows such a case.

On the other hand, during the data-taking it was observed that a big amount of the detected events occurred within an interval time of 1 μs. Considering that the expected neutron decay count rate in the decay volume is of about 1 kHz and that the minimum time for a proton to reach the detector is 5.2 μs, points that these extra events were produced

[1]This program is based on a program originally written by L. Schmitt for the readout of COMPASS.

[2]ROOT is an object-oriented data analysis framework developed by CERN

due to crosstalk between different detector-channels. To avoid counting the same event twice, the decode program checks if several of these events are grouped together. If so, all the events belonging to the group except the earliest are rejected. This cut affects typically around 4 % of the total detected events. As a consequence of this, a dead time correction has been implemented in the decode program (see subsection 3.2.4).

3.2 Events analysis

The energy of a single event is contained in the height of the event pulse. To extract the pulse height information, we subtract the baseline signal (defined in Section 3.2.1) of the corresponding detector-channel from the pulse shape maximum of the event (see Fig. 3.2). Then a histogram with the pulse height information is filled including all events recorded during a measurement cycle, which lasts between 30 and 300 seconds. Fig. 3.3 shows one pulse height spectrum from a measurement cycle with 50 V applied at the analyzing plane. The peak centered at about 35 ADC-channels corresponds to thermal noise from the detector electronics, whereas the protons are found in the right peak, which is centered at about 80 ADC-channels. The uncertainty of each point of the spectrum with N counts is only statistical, given by $\sqrt{N}$ (Poisson distribution).

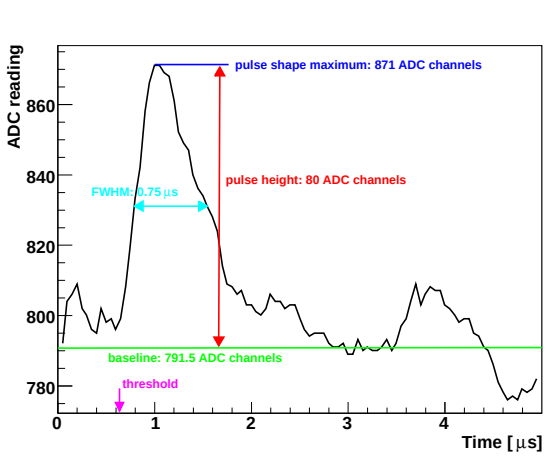

Figure 3.2: A typical proton event. The maximum of the pulse shape minus the baseline (previously fixed for each detector-channel, see text) is extracted to get information about the energy of the proton, in ADC-channels.

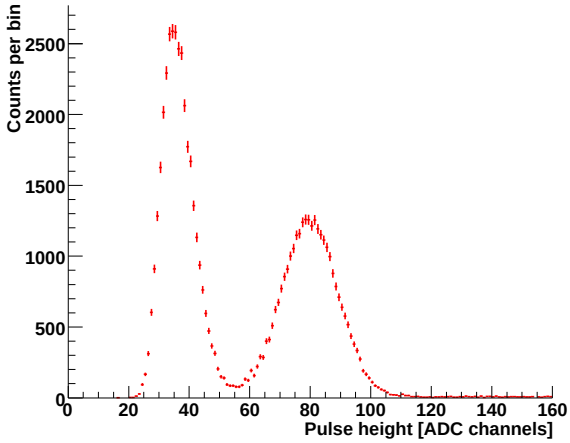

Figure 3.3: Pulse height for a measurement cycle at $U_A = 50$ V. Two peaks are distinguished. The left one corresponds to thermal noise from the detector. Decay protons are found in the peak on the right.

3.2.1 Baseline

Each detector-channel has a different baseline because the amplification of the ADC reading is provided independently for each of them. The baseline shows fluctuations due to noise coming from the detector and the preamplifier. One way to extract the baseline value for one event consists in simply taking the mean value of the last 1 μs of the event shape, which includes 20 samples. The extracted baseline mean value typically amounts to several hundreds of ADC-channels with a standard deviation of 6.5 ± 2.7 ADC-channels. In Fig. 3.4 a typical pulse height spectrum is shown in black, where the baseline has been extracted individually for each event.

However, it was found that the time-dependence of the baseline of each detector-channel had no significant drift during a set of measurement cycles lasting several hours.

Consequently, the baseline value for each detector-channel could be extracted by averaging about 10^6 values, resulting in a more accurate mean value. With this method, the standard deviation of the baseline mean value for one detector-channel is only 0.4 ADC-channels. Fig. 3.4 shows, in red, the pulse height spectrum obtained by fixing each detector-channel's baseline by averaging a set of measurement cycles. The separation between thermal noise peak and proton peak is clearly improved.

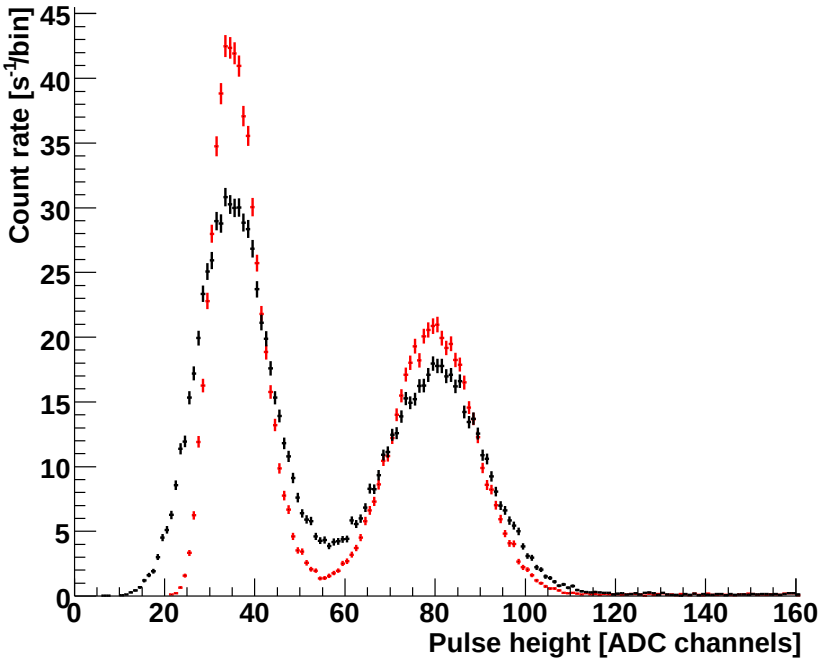

Figure 3.4: Two pulse height histograms extracted from the same data but obtained from two different baseline determination methods. For the black curve the baseline has been obtained individually from each event pulse, whereas for the red curve the baseline has been fixed previously for each detector-channel and set of measurement cycles. As it can be seen, the latter method provides a better separation between thermal noise and proton peak.

The shape of the event pulse signal can be approximately described by a theoretical function, consisting of the product of two exponential functions with amplitude A and different time constants τ_1 and τ_2 (see Fig. 3.5):

$$y(x) = \begin{cases} y_0 & \text{for } x < x_0 \\ y_0 + A\left(e^{-\frac{x-x_0}{\tau_1}}\right)\left(1 - e^{-\frac{x-x_0}{\tau_2}}\right)^p & \text{for } x \geq x_0 \end{cases} \tag{3.1}$$

In this description, the pulse height maximum of the pulse shape depends on the parameters A, p, τ_1, and τ_2. After optimizing the initial values of these parameters, one can determine the height of an event pulse by fitting it (see [Pet07]). The advantage of this method is that it eliminates the influence of noise on the maximum of the event. However, the proton signal is not amplified enough and this method does not improve in separating the protons from the electronic noise. The resulting pulse height spectra also does not show any significant improvement. Since, in addition, the fitting process takes a significant amount of time it was not worth to use it.

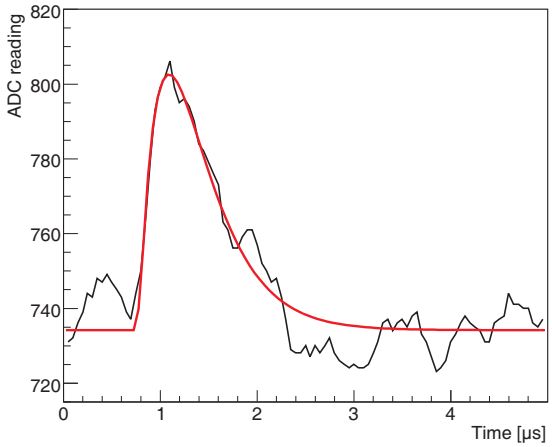

Figure 3.5: Measured event pulse (in black) fitted with the fit function given in Eq. 3.4 (in red). The fitting pulse method does not clearly help in distinguishing good events from electronic noise.

3.2.2 Pulse height spectra

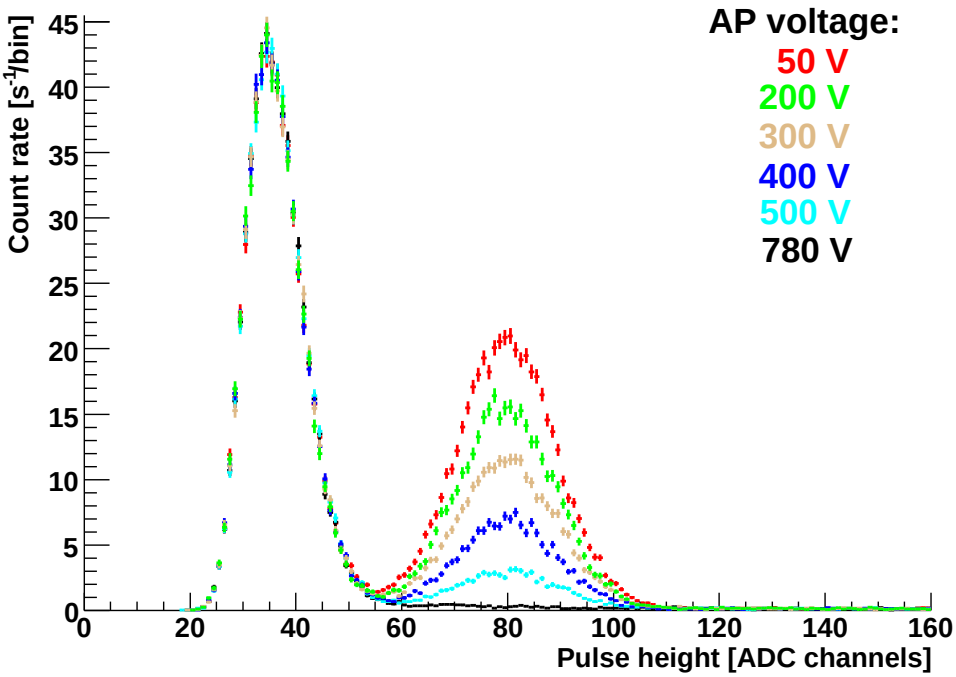

Figure 3.6: Pulse height histograms normalized by the total measurement time of the corresponding measurement cycle. The lower is the analyzing plane voltage U_A, the higher is the proton count rate in the pulse height histogram.

For each individual measurement cycle the total measurement time is inferred, which is the time interval between the first and the last detected event. The total measurement

time can differ a little from measurement cycle to measurement cycle. Hence, to extract the right amount of decay protons per cycle, it is necessary to normalize the pulse height spectrum of each measurement cycle by its measurement time. However, it is not necessary to normalize with respect to the neutron flux. During a set of measurement cycles (i.e. for several hours) the neutron count rate was found to be stable enough and the relative error on a due to fluctuations in the neutron flux is smaller than the statistical error.

In Fig. 3.6 time-normalized pulse height spectra for different applied analyzing plane voltages U_A are shown. Please note that the proton count rate decreases when the analyzing plane voltage is ramped up. Each individual pulse height corresponds to a measurement cycle of 60 seconds and includes all available detector-channels.

Although plotted together, the pulse height analysis for each measurement-cycle has been performed individually for each detector-channel due to the small differences between the used detector-channels, mainly because of different output signal amplification (for further details see Section 3.2.7).

The uncertainty $\Delta N(U_A)$ for each bin of the normalized pulse height histogram with count rate $N(U_A)$ is given by:

$$\Delta N(U_A) = \frac{\sqrt{N(U_A)}}{t} \tag{3.2}$$

where t is the total measurement time of the measurement cycle.

To extract the coefficient a with an accuracy of $\Delta a/a = 5\%$, the proton count rate, at $U_A = 50$ V, has to be measured with an accuracy of $\Delta N/N < 2 \times 10^{-4}$.

3.2.3 Background-free pulse height spectra

No protons should be detected in measurement cycles with $U_A = 780$ V, which therefore, are used as background measurements. By subtracting the closest measurement cycle in time at $U_A = 780$ V from a measurement cycle at another analyzing plane voltage, the background-free pulse height spectrum is obtained (see Fig. 3.7). Background measurements contain basically thermal noise of the detector, beam-related background (mainly electrons) and environmental background[3]. Thus, background subtraction is complete only when the background is stable enough in time and is independent of the analyzing plane voltage. The fluctuations seen in Fig. 3.7 at the position of the thermal noise (at about 40-ADC channels) are an indication that the thermal noise is not stable in time.

Studies on the shape of the proton peak can be found in [Pet07], where it was shown that the proton peak is well fitted by a Gaussian function. In principle, the center of the proton peak is expected to move slightly to higher ADC-channel values when increasing the analyzing plane voltage, since also the mean energy of the protons that can pass the analyzing plane is higher. However, the width and the position of the gaussian functions that fit the proton peaks for different analyzing plane voltages are almost constant. The

[3] A more detailed background study is given in Chapter 4.

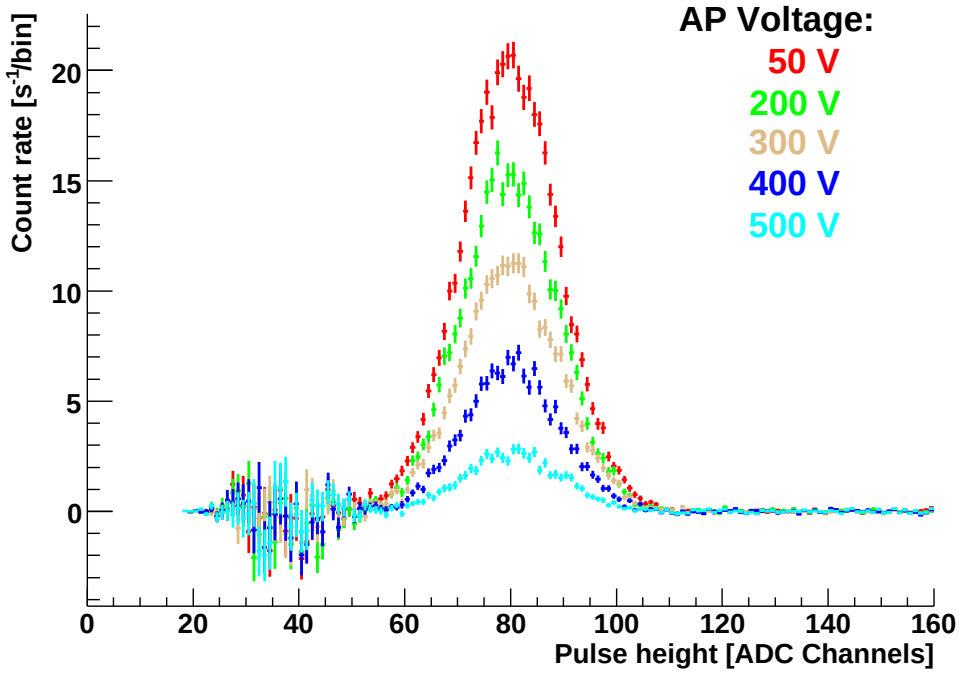

Figure 3.7: Pulse height histograms for different analyzing plane voltages U_A where the closest background measurement in time for $U_A = 780$ V have been subtracted. The fluctuating count rate at lower ADC channels is due to electronic noise instabilities and to the bad separation between the thermal noise of the detector and the proton signal.

reasoning of that is that the width of the proton peak is mainly dominated by baseline fluctuations. Baseline fluctuations due to detector and preamplifier noise add as well fluctuations to the maximum of the event shape. Hence, the measured pulse height maximum consists of the event shape maximum plus baseline fluctuations.

There is no straightforward way to isolate each individual event shape from its fluctuations, but the contribution of the baseline fluctuations on the signal can be estimated.

Let's assume that the real event shape maximum is flat for about 0.5 μs and that the measured maximum of the event contains 2σ error. Here σ is the fluctuation width of the maximum of the baseline within 0.5 μs, which is of about 7.5 ADC-channels. Thus, in this estimation the pulse height maximum fluctuates within 15 ADC channels. The width of this fluctuation is comparable to the width of the proton peak at FWHM, which has been measured to be of about 11 ADC channels.

3.2.4 Proton extraction

For each measurement cycle and detector-channel, the proton count rate $N(U_A)$ at analyzing plane voltage U_A is determined by summing up the number of events from the background-free pulse height histogram in the so-called **Proton Counting Window** (PCW). Assuming a Gaussian shaped proton peak, the PCW contains at least the 99.95%

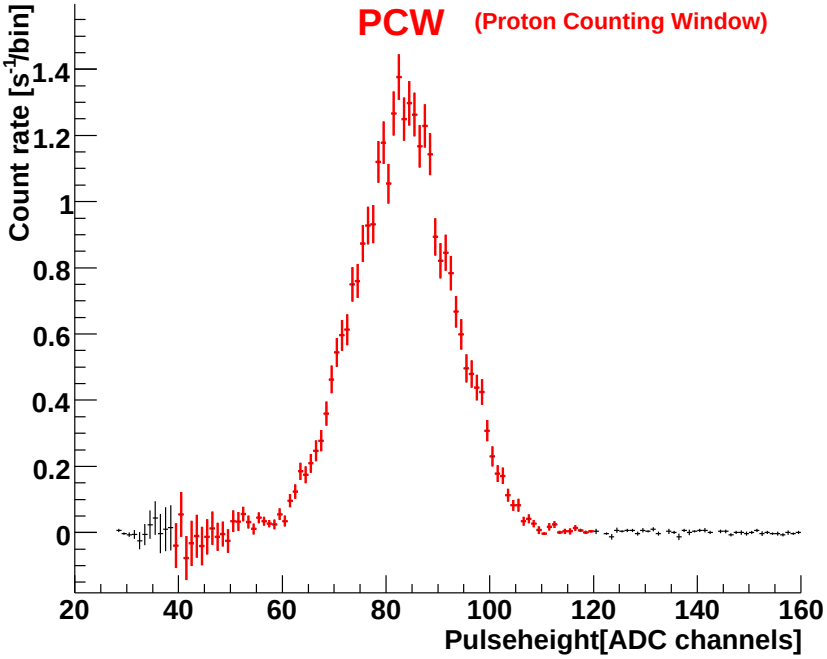

Figure 3.8: The red part of the pulse height histogram shows the interval of the Proton Counting Window (PCW) for events from one single detector-channel.

of the Gaussian area[4], from where $N(U_A)$ is obtained with a relative error of $\Delta N/N \approx 5 \times 10^{-4}$. The PCW extends from the pulse height channels 40 to 120.

The position of the proton peak within the PCW window is shifted when the high voltage applied to the detector is modified (as can be deduced from Equation 2.27). By increasing the high voltage applied to the detector, the proton peak shifts to higher ADC-channels, while the electronic noise peak remains at the same position. A proton peak shift can as well be caused by the characteristics of the detector used, like the dead layer thickness. Small differences on the dead layer thickness were observed among the different PIN-diode detectors used during the beam time at FRM-II.

The same PCW is used for all sets of measurement cycles obtained with the same detector and high voltage in order to avoid analyzing plane voltage dependencies on the proton count rate. During the data-taking period, for the analyzing plane set at $U_A = 50$ V, the proton count rate on the entire detector (using all available detector-channels) was about[5] 500 s^{-1}.

The integration of the proton count rate in the PCW of the pulse height histogram for one measurement cycle is performed individually for every detector-channel. Due to

[4]This is accomplished by fixing the lower and upper limits of the Proton Counting Window $\pm$ 3.5 σ away from the maximum position of the Gaussian fit over the proton peak.

[5]In Section 3.2.7 will be explained that a rebinning process on the data will take place before to extract the protons in the PCW.

the dead time of each detector-channel[6], a dead time correction has to be applied to the obtained proton count rate to take into account events not detected during this period of time. The corrected proton count rate N_{Real} is related to the measured proton count rate $N_{Measured}$ and to the dead time τ of the detector-channel (typically of 5 or 6.4 μs) by [Leo94]:

$$N_{Real} = \frac{N_{Measured}}{1 - (N_{Measured} \times \tau)} \tag{3.3}$$

The total proton count rate of each measurement-cycle for a given analyzing plane voltage $N(U_A)$ is obtained considering the count rate of all detector-channels. Finally, an average of the proton count rate $\bar{N}(U_A)$ from all measurement-cycles is extracted for every analyzing plane voltage U_A and for each set of measurement-cycles.

The uncertainty of $\bar{N}(U_A)$ includes the variation of the individual measurement-cycle count rates and the maximum uncertainty due to the Poisson distribution. In our data, the variation of the individual measurement-cycle count rates usually had a higher value than the Poisson distribution. This could mean that the subtracted background count rate was instable or that it had not a normal statistical behaviour.

3.2.5 Extraction of a

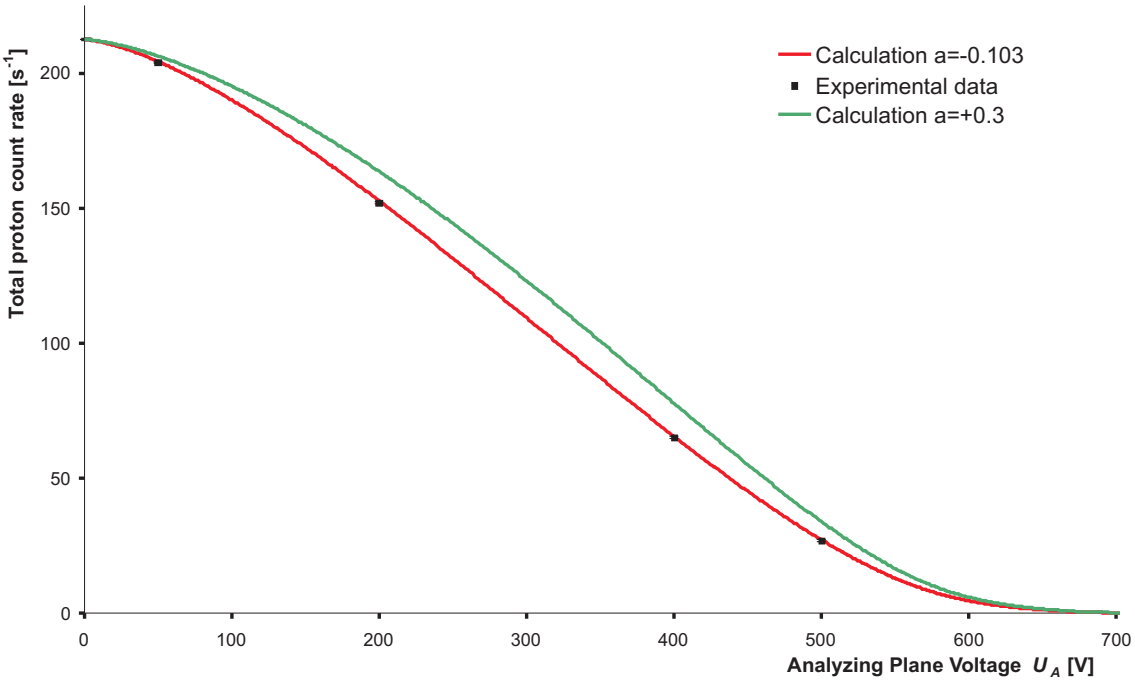

Figure 3.9: Integral proton spectrum calculated for two different values of a. The experimental data shown corresponds to about 12 hours of data-taking. Please note that some error bars are smaller than the symbol size. All error bars are only statistical.

[6]The dead time of each detector-channel is given by the event length (See section 2.5).

The extracted proton count rate averages $\bar{N}(U_A)$ for each analyzing plane voltage U_A and for each set of measurement cycles are fitted with the theoretical function $W(T)$ given in Eq. 3.4, which includes, among others, the coefficient a as a fit parameter. T is the kinetic energy of the decay proton. The form of this function is complex and its derivation can be found in [Glü93]. It is obtained by numerically integration of the product of the transmission function $F_{tr}(T_0)$ (Eq. 2.23) with the differential proton spectrum $w_p(T)$. $w_p(T)$ includes Coulomb, recoil and radiative corrections[7]:

$$W(U_A) = N_0 \int_0^{T_{max}} F_{tr}(T, U_A) w_p(T) dT \tag{3.4}$$

$W(U_A)$ contains several fit parameters, like the intensity of the spectrum and $\Delta(U_A - U_0)$. T_{max} is set at 751.4 eV, which is the end point energy of the decay protons. In Figure 3.9, a set of measured points and two calculated integral proton spectra are plotted, for comparison, for two different values of a.

3.2.6 Edge effect

In Fig. 3.10 the proton count rates per each detector-channel are plotted for one measurement cycle with $U_A = 50$ V. Whereas the central detector-channels have similar proton count rates, in the outer detector-channels a gradually decrease of the proton count rate is observed. This shape is a consequence of the diaphragm placed on top of electrode $e6$ (see Fig. 2.11), which interacts with the helical orbit of the protons in the magnetic field. This diaphragm causes an Edge effect on the flux tube size, which will become dependent on the longitudinal proton kinetic energy.

The gyration radius of a decay proton depends on its energy and on its emission angle between its momentum and the magnetic field lines. As it is shown in Fig. 3.11, for a very thin diaphragm (12 μm), the amount of protons with a determined longitudinal kinetic energy produced outside the flux tube that pass the diaphragm is compensated by those protons with the same energy produced within the flux tube but that hit the diaphragm. Then, the edge effect caused by the diaphragm would canceled out. However, this cancellation is only true if the neutron beam density is homogeneous [Zim00].

In reality, the neutron beam density is not completely homogeneous in the decay volume, see Fig. 3.12. In order to keep the edge effect contribution to the uncertainty of the parameter a smaller than 10^{-4} this density should be determined to a few percent accuracy [Glü05].

Furthermore, the cancellation is not perfect if the detector dimensions are not big enough to fit the flux tube nor in the case that the detector efficiency depends on the detection position. The latter case occurs in our segmented silicon PIN diode, where the detection efficiency is position dependent due to the non-active areas between two detector stripes.

[7]The value of the Coulomb, recoil and radiative correction functions have been extrapolated from the tables calculated in [Glü93].

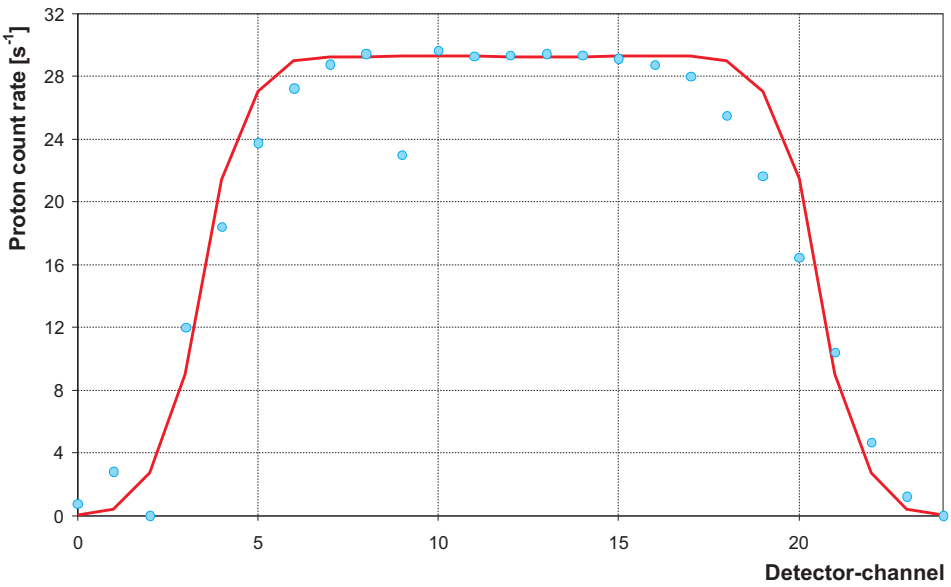

Figure 3.10: The proton count rate is represented per each detector-channel. Detector-channels 2, 9 and 23 were not working properly. In this example, due to the edge effect caused by the diaphragm (see text), only detector-channels 8 to 15 (but no 9) are used for the analysis. The diaphragm has an aperture of 2.5 cm. The curve line shows the calculation of the edge effect, although the effect of both $E \times B$ drifts is not included in the calculation.

In the measurement shown in Fig. 3.10, detector-channels 2, 9, and 23 were not working properly and it is difficult to know with enough accuracy if there are tails of the proton beam profile that did not reach the detector. Therefore, these detector-channels have to be omitted of the analysis, which implies either to calculate the edge effect or to remove all outer detector-channels. Edge effect calculations become very complicate when the drift produced on the proton beam profile by the lower E×B is included. Thus, the data analysis was done by taking only central detector-channels where the count rate is constant. For the measurement shown in Fig. 3.10 only detector-channels 8 to 15 (omitting channel 9) have been analyzed. Nevertheless, since central detector-channels contain the main amount of the count rate, the total count rate gets reduced only to the half, which is still enough to extract a with an statistical uncertainty of about 5%.

On the other hand, there exists also a transverse edge effect affecting all detector-channels due to the size of the detector in the direction perpendicular to the neutron beam. In this direction, the flux tube at the detector position is bigger than the length of the detector stripes. The shift on the value of the coefficient a due to the systematic effect produced by the not detected protons is of about 1% towards the negative values. This result is given by the difference in the coefficient a extracted from simulations considering and not considering this edge effect [Kon11].

3.2.7 Rebinning

Each detector-channel has an independent signal amplification, which can produce slight amplification gain differences among the detector-channels. These differences result in

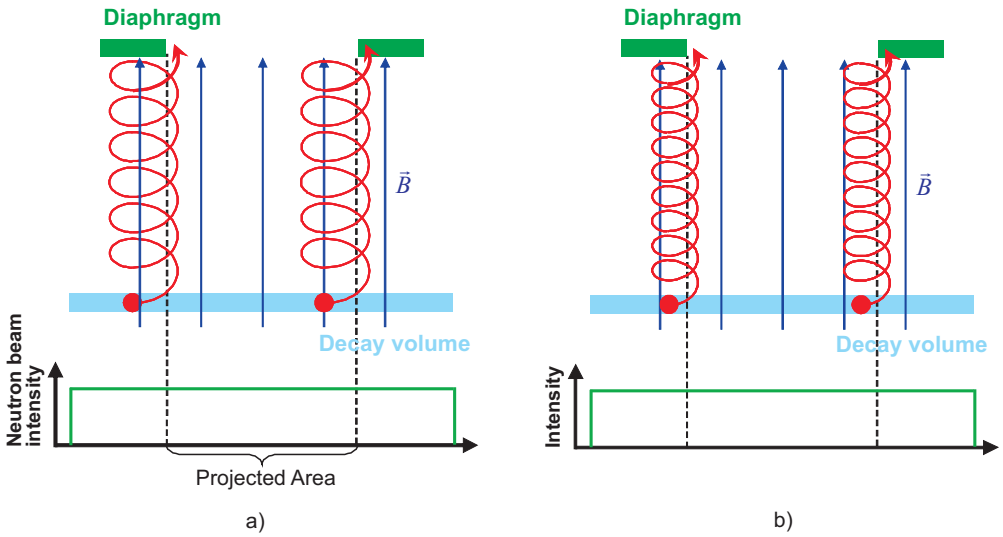

Figure 3.11: Protons produced outside the flux tube can pass the diaphragm and protons produced inside the flux tube can be absorbed by the diaphragm. Then, if the neutron beam intensity is flat, the edge effect produced by the diaphragm is cancelled. In case a) the protons have a bigger gyration radius than in case b).

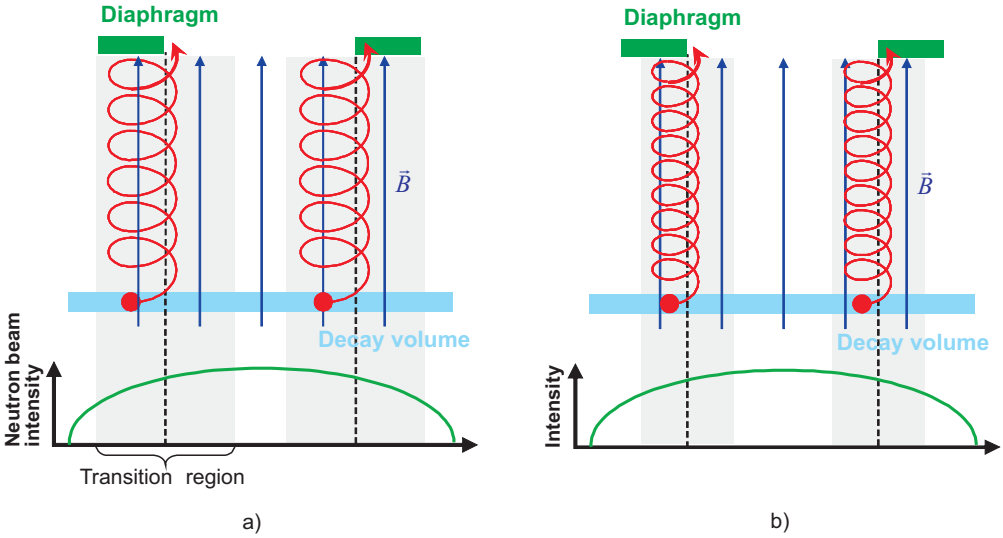

Figure 3.12: Same picture as Fig. 3.11 but here the neutron beam profile is not flat and the edge effect of the diaphragm in not cancelled.

small shifts between the pulse height histograms of the several detector-channels (see Fig 3.13). A pulse height shift due to different signal amplification affects the maximum position and the width of the proton peak shape because the count rate per ADC-channel bin is distributed slightly different.

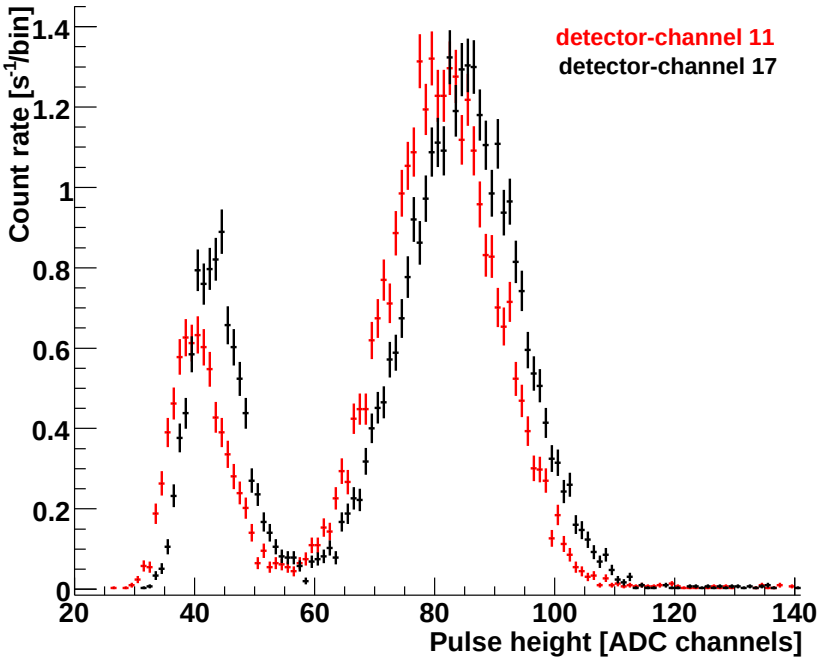

Figure 3.13: Both pulse height histograms belong to the same measurement cycle at $U_A = 50$ V but correspond to two different detector-channels used in the analysis. A shift between them can be observed by eye.

It is necessary that proton count rates from all central detector-channels, C_{ch}, used in the analysis are completely included in the PCW. Hence, to obtain the total proton count rate for each detector-channel i under the same conditions, a rebinning (or normalization) of the pulse height histograms is needed by means of a rebinning factor f_i. However, if f_i is not an integer the bin dimensions will change, distorting as well the dimensions of the ADC-channels from the resulting pulse height.

In the rebinning process each analyzed pulse height signal is additionally multiplied by a random-like generated number which gives the probability that a signal be assigned to one ADC-channel bin. With this method all bins maintain the same dimension avoiding that, for instance, samples with pulse height reading of 50.4 ADC-channels be systematically assigned to the bin 50 ADC-channels. Instead, it is taken into account as well the probability that 50.4 ADC-channels be assigned to the bin 51.

A pulse height reference position for each detector-channel is needed in order to detect the pulse height shifts. The reference is determined by fitting the proton peak of the pulse height histograms from measurement cycles at $U_A = 50$ V with a Gaussian function, and recording the position of its maximum x_{max}. For each set of measurement cycles and for each detector-channel i, the mean value of the Gaussian's maximum position $\bar{x}^i_{max}$ is

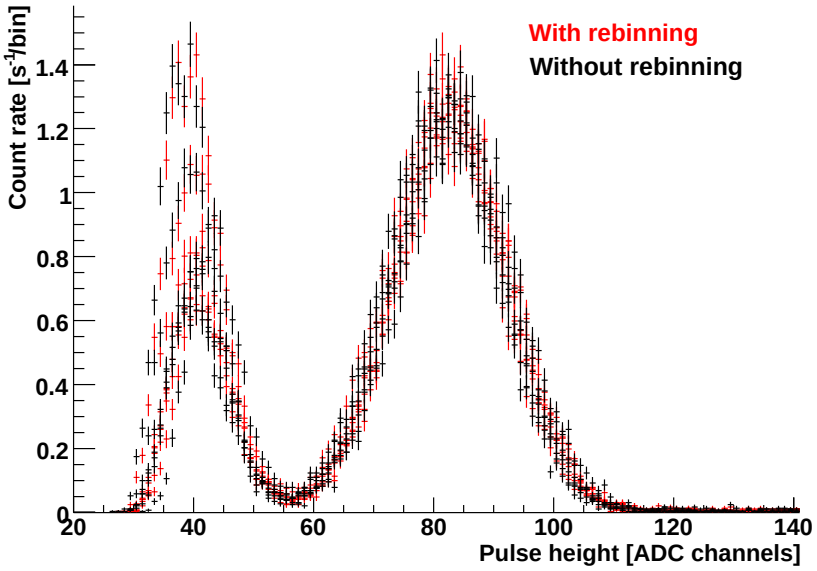

Figure 3.14: All pulse height histograms for a measurement-cycle at $U_A = 50$ taken from central detector-channels plotted before and after applying the rebinning correction. No evident differences can be seen.

obtained.

The normalization factor f_i for detector-channel i and for a determined set of measurement cycles is finally obtained dividing $\bar{x}^i_{max}$ by the average of the Gaussian's maximum position from all detector-channels:

$$f_i = \frac{\bar{x}^i_{max}}{(\frac{\sum_j^N \bar{x}^j_{max}}{C_{ch}})} \tag{3.5}$$

For the determination of the rebinning factors it is necessary to decode the data twice. The first decoding process gives information about the shift of the pulse height histograms from which rebinning factors can be obtained. In the second decoding process, rebinning factors are applied when creating pulse height histograms.

Fig. 3.14 shows pulse height histograms for each detector-channel before and after the rebinning process. In this example, the pulse height histograms after the rebinning process can barely be distinguished from the ones without it. In fact, the change in a due rebinning process is only of 0.5%. Therefore, the contribution in the final a value due to different amplification between the detector-channels is very small.

Chapter 4

Results

In this chapter, the results of the data analysis are presented. First, an overview over the recorded data that can be used to extract the angular correlation coefficient a is given. Beside the measurements devoted to determine a, additional measurements were performed to study the experimental background, since a high precision in the measured proton count rate is needed to obtain a reliable value of a. Investigations of the beam dependent and beam independent background contributions and of the background count rate stabilities are later presented.

The most significant result of these studies is that an unexpected excess background exists within the energy range of the proton peak. Since this excess background is found to be unstable in time, it cannot be correctly subtracted from the measured data, thus hindering the exact determination of a from the measurements taken at FRM-II. However, it is observed that the extracted value of a is closer to the current Particle Data Group value when the excess background in the analyzed data set is smaller.

A more detailed discussion of the excess background is the subject of the following Chapter 5.

4.1 The data

Two main data cycles, *Cycle A* and *Cycle B*, have been analyzed for the extraction of the angular correlation coefficient a as well as for background studies. Each data cycle corresponds to a few days of data acquisition distributed over several sets of measurement-cycles. One set of measurement-cycles consists of a period (0.7 to 14 hours) during which the data acquisition process was not interrupted and the settings were not changed (except for the analyzing plane voltage). One measurement-cycle lasts between 30 and 300 seconds, which is the shortest subset measurement and corresponds to a particular analyzing plane voltage. All measurements contained in one of the two data cycles were performed under equal detection conditions. In particular, during one cycle always, the same preamplifier

and proton detector were used, without changing their position inside the spectrometer[1].

PARAMETERS	*Cycle A*	*Cycle B*
Preamplifier N°	1	2
Detector N°	2	2
Window 1 [μs]	0.8	1.6
Window 2 [μs]	25.6	25.6
Pulse length [bins]	128	100
Detector-channels used for the analysis	11 to 17	8 to 15 (omitting 9)

Table 4.1: Measurement conditions that remained constant during the two data cycles. In addition, during these periods the detector was not retracted from its position. Notice that *Cycle A* and *Cycle B* were not taken with the same preamplifier. Although both are of the same type, they can have slightly differences in their responses. For all beam-times performed at FMR-II, 10 PIN-diode detectors and 2 preamplifiers were available (see [Sim06] for further detail).

Cycle A was taken between the 4th and the 10th of April 2006, whereas *Cycle B* comprises measurements from the 26th to the 30th of April 2006. Both data cycles contain measurements from which the angular correlation coefficient a can be extracted as well as measurements dedicated to background and systematics studies. The general settings that remained unchanged during each data cycle are given in Table 4.1.

DATA SETS / PARAMETERS	0404D	0504D	0604D
Main Coils Current [A]	40	50	50
High Voltage [kV]	-30	-30	-31
Lower E × B [V]	0/-500	0/-500	0/-700
Upper E × B [kV]	-2/-2	-2/-2	-2/-2
Time Meas. Cycle [s]	300	300	300
Number Meas. Cycles	65	141	169
Total duration [hours]	5.4	11.8	14.1
Interval between background measurements [Meas. Cycles]	4/5	7	7
Threshold settings	Thr 1	Thr 2	Thr 2

Table 4.2: Settings of several parameters used for the measurement-cycles of *Cycle A*. Threshold setting values are given in Table 4.5.

For the analysis of the data, only measurement-cycles that show no instabilities in their settings have been taken into account. Thus, for some sets of measurement-cycles, it was necessary to remove individual measurement-cycles which were affected by one or several of the following anomalies: data acquisition mistakes, high voltage instabilities or

[1]Nevertheless, the existence of undetectable effects (e.g. small discharges) that influence the detection conditions can not be excluded.

analyzing plane voltage instabilities. The amount of rejected measurement cycles due to these reasons is below 1%, showing the high reliability of the experimental setup.

Cycle A contains 3 sets of measurement-cycles from which the angular correlation coefficient a can be extracted. The settings of these measurements are given in Table 4.2, while the settings of the 4 sets of measurement-cycles used to extract a from *Cycle B* are shown in Table 4.3.

DATA SETS / PARAMETERS	2604M	2604N	2704N	3004D
Main Coils Current [A]	50	50	50	50
High Voltage [kV]	-30	-30	-30	-30
Lower E × B [V]	0/-150	-1000/-1150	-1000/-1150	-1000/-1150
Upper E × B [kV]	-4/-2	-4/-2	-4/-2	-4/-2
Time Meas. Cycle [s]	180	60	60	60
Number Meas. Cycles	141	648	419	19
Total duration [hours]	7.9	10.8	7.0	0.7
Interval between background measurements [Meas. Cycles]	4	4	4	4
Threshold settings	Thr 3	Thr 3	Thr KG	Thr KG

Table 4.3: Settings of several parameters used for the measurement-cycles of *Cycle B*. Threshold setting values are given in Table 4.5.

During the *Cycle A* data-taking period, the applied analyzing plane voltage U_A followed mainly a sequence where background measurements $U_A = 780$ V were taken every 7 measurement-cycles. Measurement-cycles taken in between two background measurements where chosen randomly among 0, 50, 100, 150, 200, 250, 300, 350, 400, 450, 500, 550 and 600 volts. For *Cycle B*, the sequence chosen was optimized to obtain more detailed information about the background in order to check for systematic effects[2]. The typical order of such sequence is shown in Table 4.4 and consists of four measurement-cycles. It starts with a measurement-cycle at $U_A = 50$ V. Then follows a measurement at an intermediate analyzing plane voltage x, which it is randomly chosen from 100, 200, 400, 500 and 600 volts. Afterwards, a background measurement at $U_A = 780$ V and a measurement at $U_A = 0$ V are taken. The function of this last measurement is to remove particles from the spectrometer which might be trapped between the analyzing plane and the mirror electrode.

Measurement number	1	2	3	4	5	6	7	...
AP voltage (V)	50	x	780	0	50	x	780	...

Table 4.4: Analyzing plane voltage sequence used during the data-acquisition of *Cycle B*. The voltage x is randomly chosen from 100, 200, 400, 500 and 600 volts.

[2]The optimization of the sequence for statistical sensitivity can be found in [Zim00].

Detector-channel	*Cycle A*		*Cycle B*	
	Thr 1	Thr 2	Thr 3	Thr KG
8	not used	not used	13	14
9	out of order	out of order	out of order	out of order
10	not used	not used	14	14
11	20	21	14	14
12	20	21	14	14
13	20	21	14	14
14	20	21	14	14
15	20	21	14	14
16	20	21	not used	not used
17	20	21	not used	not used

Table 4.5: Values of the several threshold settings used in *Cycle A* and *Cycle B*. Only central detector-channels are used for the analysis because of edge effects (described in Section 3.2.6).

In *Cycle A* and *Cycle B* several *threshold* settings have been used (see Page 60 for the trigger algorithm description). The threshold values for each detector-channel are given in Table 4.5.

4.2 Background

The background in *a*SPECT can be divided into a neutron beam correlated and an uncorrelated contribution. The background events correlated to proton events are mostly electrons produced in the same neutron decay but also γ radiation and high energetic electrons created in neutron capture. Uncorrelated events are due to thermal noise from the detection system, to positive ions coming from residual rest gas and to cosmic rays [Glü05] [Zim00].

As explained in Section 3.2.3, background measurements are performed by setting the analyzing plane voltage above 751.4 V, which is the end point energy of the decay protons. They are taken typically at $U_A = 780$ V or $U_A = 800$ V. Afterwards, the background spectrum is directly subtracted from the pulse height spectra at different analyzing plane voltages. Consequently, anomalies in background measurements have a big influence on the extracted proton count rate.

To ensure that the background in *a*SPECT is understood, several systematic checks have been performed. In this section, a background study to check for count rate instabilities is presented.

4.2.1 Background stability

With the aim to measure the sensitivity to the different background contributions, background fluctuations for three different windows of the pulse height histogram (see Fig. 4.1) have been investigated (all, taken at $U_A = 780$ V):

- Background Window 1 **BW1**: 0 to 50 ADC-channels
- Background Window 2 **BW2**: 65 to 120 ADC-channels
- Background Window 3 **BW3**: 120 to 2000 ADC-channels

Each background window isolates a specific background type: *BW1* contains (almost the whole) thermal noise from the detector electronics, the so-called *electronic noise peak*; *BW2* comprises a big part of the background under the proton peak but free of thermal noise; *BW3* contains the background beyond the proton peak, mainly decay electrons.

Figure 4.2 (a), (b) and (c) show for each of the background windows, the respective averaged background count rate per measurement-cycle for one set of measurement-cycles. The two sets of measurement-cycles plotted are, the longest from *Cycle A* (0604D) and the longest from *Cycle B* (2604N). These two sets contain very different amount of background data mainly because their interval between background measurements as well as the duration of each measurement cycle are quite different (see Tables 4.2 and 4.3).

From Fig. 4.2 the following observations can be extracted:

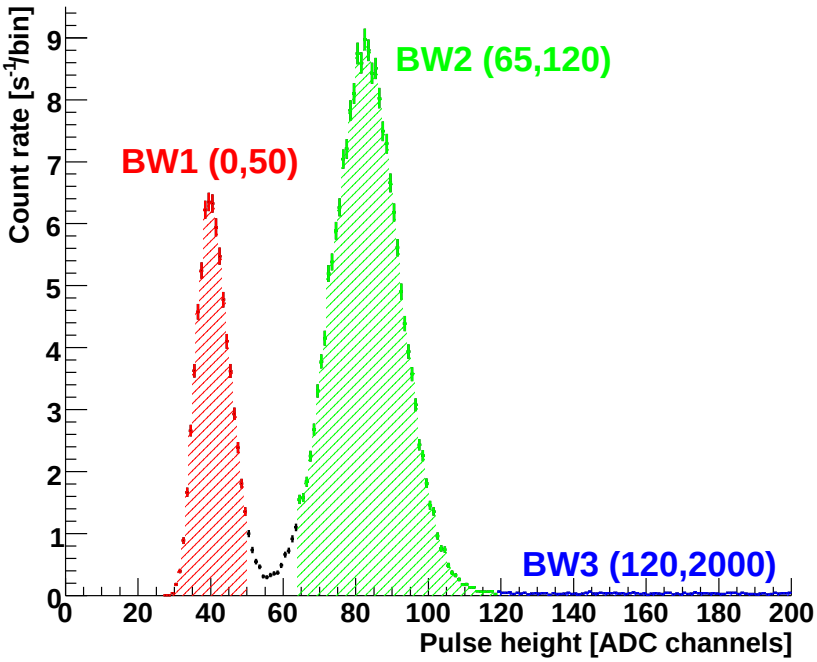

Figure 4.1: Background Windows used to check the stability of background measurement-cycles at $U_A = 780$ V. Please note that in this diagram a pulse height histogram at $U_A = 50$ V is used for a better understanding of the several Background Windows.

- In Fig. 4.2 (a):

  - The absolute count rate level in BW1 (mostly due to thermal noise from the detector) of *Cycle A* and *Cycle B* data is very different. That is because they were taken with different threshold settings.

  - Both plots show a drift of the count rate with time in BW1.

- In Fig. 4.2 (b):

  - The absolute count rate level in BW2 (mostly decay protons) is higher in *Cycle B* than in *Cycle A* data.

  - Both data distributions show non-statistical count rate fluctuations in BW2, but no count rate drift.

- In Fig. 4.2 (c):

  - Both data cycles have similar count rate levels in BW3 (mostly decay electrons), although in *Cycle A* the count rate is slightly higher than in *Cycle B*. That is because the used detector channels are different for the two cycles (see Table 4.1).

  - The count rate fluctuations in BW3 are smaller than in Fig. 4.2 (b). No count rate drift is observed in this background window.

More accurate information concerning the background count rate instabilities has been obtained by estimating the non-statistical fluctuations contained in background count

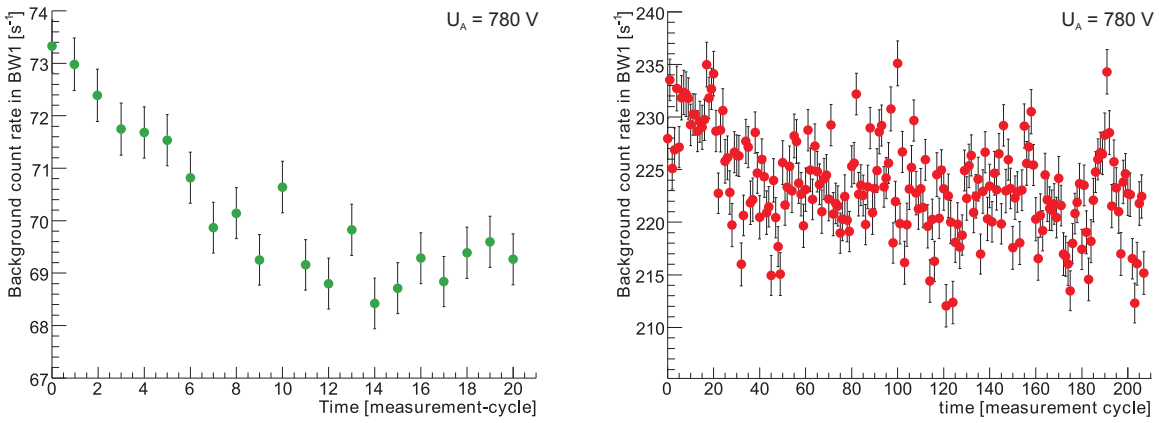

(a) BW1 - Integration from 0 to 50 ADC-channels.

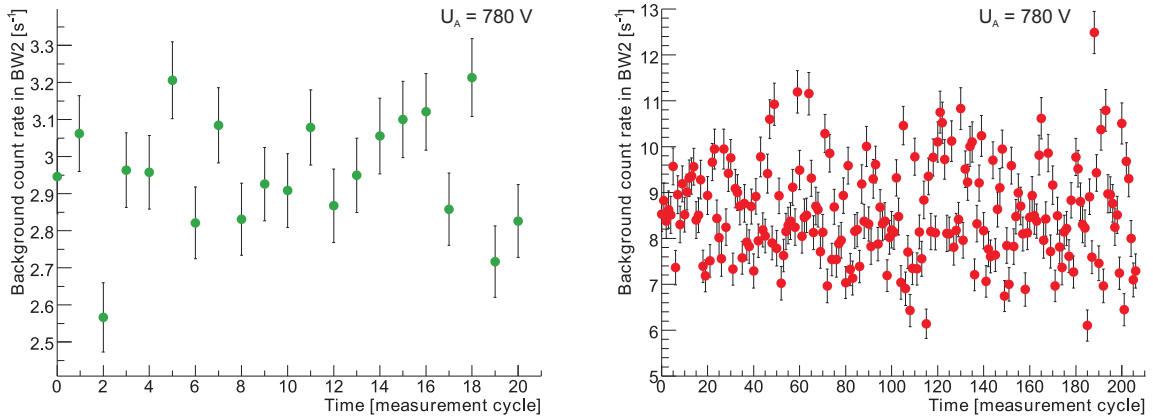

(b) BW2 - Integration from 65 to 120 ADC-channels.

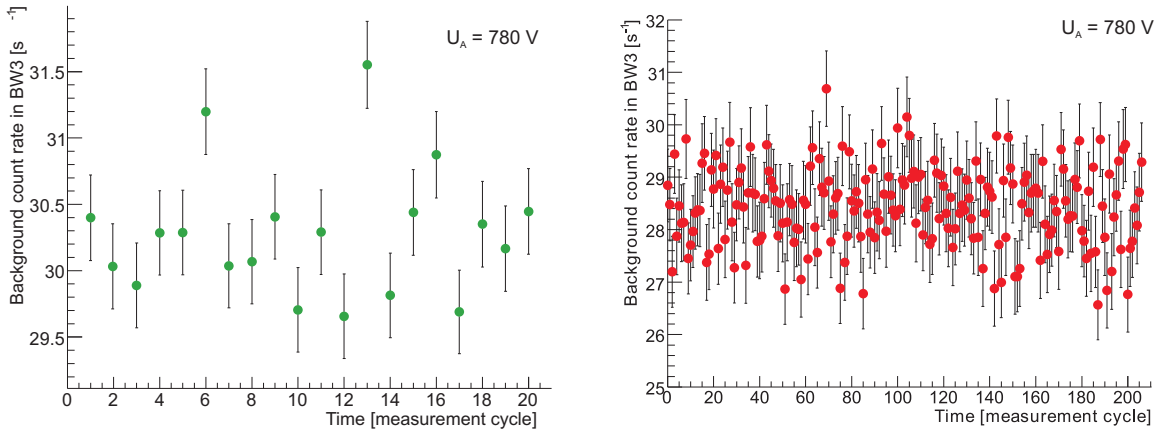

(c) BW3 - Integration from 120 to 2000 ADC-channels.

Figure 4.2: Background count rates of measurement-cycles from *Cycle A(0604D)*, left side, and *Cycle B(2604N)*, right side, for different integration windows.

rates for each window and for each set of measurement-cycles. This is done by estimating the width of the distribution of the non-statistical fluctuations, σ_{NSF}, in the case that chi-square would equal the number of degrees of freedom[3]. Then, chi-square distribution is written as [Ams08]:

$$\chi^2 = \sum_i^n \frac{(\bar{x} - x_i)^2}{\sigma_i^2 + \sigma_{NSF}^2} = n - 2 \tag{4.1}$$

where n is the number of measurement-cycles measured at $U_A = 780$ V, $\bar{x}$ the mean value of the count rate from all measurement-cycles, and x_i and σ_i are the individual count rate value and its corresponding statistical error (given as $\sqrt{x_i}$) of one measurement-cycle. The two parameters, $\bar{x}$ and σ_{NSF} are fit parameters and, therefore, they are subtracted from the number of degrees of freedom.

If the experimental data contains only statistical fluctuations, then σ_{NSF} is expected to be zero.

The estimated value for non-statistical fluctuations σ_{NSF} contained in the background measurements for every set of measurement-cycles as well as its relative value with respect to the total averaged count rate, $\frac{\sigma_{NSF}}{\bar{x}}$, are given in Table 4.6. From the data of the table one extracts that:

- All sets of measurement-cycles of *Cycle A* and *Cycle B* contain relative non-statistical fluctuations of the count rates in window BW1, up to 2%.

- In window BW2, 4 sets of measurement-cycles contain a relative non-statistical count rate fluctuations of 5%. The other 3 sets of measurement-cycles fluctuate a lot more, up to 35%.

- The relative non-statistical fluctuations of the background count rates in window BW3 are below 1.7% in all sets of measurement-cycles.

Set of meas. cycles	**BW1**		**BW2**		**BW3**	
	σ_{NSF} $[s^{-1}]$	$\frac{\sigma_{NSF}}{\bar{x}}$ [%]	σ_{NSF} $[s^{-1}]$	$\frac{\sigma_{NSF}}{\bar{x}}$ [%]	σ_{NSF} $[s^{-1}]$	$\frac{\sigma_{NSF}}{\bar{x}}$ [%]
0404D	0.38	0.24	0.15	6.1	0.06	0.2
0504D	3.5	2	0.18	7.1	0.32	1.05
0604D	1.4	1.9	0.13	4.4	0.37	1.22
2604M	4.2	1.6	0.26	5.6	0.22	0.77
2604N	4.2	1.9	1	11.9	0.38	1.3
2704N	1.8	1.2	0.8	21	0.36	1.3
3004D	1.8	1.3	1.6	35.3	0.5	1.7

Table 4.6: Non-statistical fluctuations, σ_{NSF} of the background count rates in BW1, BW2 and BW3 estimated from Eq. 4.1. Also the relative non-statistical fluctuation with respect to the total averaged count rate, $\frac{\sigma_{NSF}}{\bar{x}}$, is given.

[3]For this purpose, a normal distribution of events is assumed.

The conclusions after the study of the time stability and of the non-statistical fluctuations of the background measurements in the three pulseheight windows BW1, BW2 and BW3 are the following:

- The count rate from thermal noise of the detection system is not stable in time, which could be related to temperature fluctuations of both, detector and pre-amplifier observed during the measurements [Pet07]. Since this noise overlaps to some extent with the proton peak, it introduces a systematic error to the extracted proton count rate, which a priori was unexpected. In order to minimize this error, the background measurement subtracted has to be the closest one in time to the measured signal[4].

- Significative non-statitstical fluctuations of the background count rates under the proton peak (BW2) have been estimated in all data sets. They are especially high in *Cycle B* data. These fluctuations are not understood at this stage, but they will be discussed in more detail in Chapter 5.

4.2.2 Not beam dependent background

Thermal noise and environmental background

Thermal noise originated in the detection system is observed in all measured pulse height spectra. It looks like a peak centered around ADC-channel 35 (see for instance, the first peak of the pulse height histogram in Fig. 4.1). Thermal noise count rate histograms differ for each set of measurement-cycles since they depend on the used treshold settings, the detector, the detection electronics, etc. In Table 4.7 the background count rates ($U_A = 780V$) in BW1 for sets of measurement-cycles from *Cycle A* and *Cycle B* are shown.

Measurement cycle	**Background count rate in BW1** $[s^{-1}]$	**Background count rate in PCW** $[s^{-1}]$	**Background subtracted proton count rate for** $U_A = 50V$ **in PCW** $[s^{-1}]$
0404D	158.8(3)	93.0(4)	206.9(4)
0504D	179.4(9)	97.8(6)	201.8(5)
0604D	70.2(3)	51.9(1)	204.3(2)
2604M	257.7(8)	72.9(5)	208.1(3)
2604N	223.4(3)	60.9(2)	202.7(4)
2704N	156.8(2)	42.8(2)	206.3(4)
3004D	144.4(5)	38.1(4)	207(2)

Table 4.7: Count rates of *Cycle A* and *Cycle B* data show background measurement cycles ($U_A = 780V$) integrated in BW1 (0 to 50 ADC-channels) and in PCW (40 to 120 ADC-channels) as well as proton count rates for $U_A = 50V$ integrated in PCW.

[4] A detailed study of the influence on the proton count rate when subtracting either the background measurement closest to the signal or another one measured one hour later can be found in [Pet07]. Differences in the order of 10^{-3} were observed in the extracted value of a, which is still lower than the statistical uncertainty.

In addition to the thermal noise, BW1 count rates include as well the environmental background since it can not be distinguished from the thermal noise in the data taking process. However, in our analysis it is not necessary to distinguish among this two background sources. Not analyzing plane dependent background can be safely subtracted by the 780 V background measurements.

During data-taking cycles of several hours, the count rates in BW1 show a drift, typically of about 2 s^{-1} (see Fig. 4.2). This drift is probably due to temperature changes in the detector itself and in its associated electronics [Pet07].

The count rate provided by thermal noise in BW2 (window on the proton peak region, between 65 and 120 ADC-channels) has been measured. For this purpose, background measurement-cycles (i.e., $U_A = 780$ V) in which both, the neutron beam and the magnetic field were switched off have been analyzed. The measurements show a negligible thermal noise count rate in BW2, less than 0.01 s^{-1}, either in the case the high voltage was switched on or it was switched off.

In the PCW (Proton Counting Window, between 40 and 120 ADC-channels), thermal noise is partially found since the proton peak and the thermal noise are not well separated. Count rates between 30 and 100 s^{-1} have been measured in this window. The signal-to-noise ratio is, in average, of about 3:1 for $U_A = 50V$ (see Fig. 4.1 and Table 4.7).

4.2.3 Beam dependent background

Neutron decay products (basically electrons), beam related rest gas ionization processes and the products from neutron capture processes that take place in the collimation system and in the beam stop are the main sources of beam related background. To reduce the amount of beam related background a good design of the neutron collimation system is crucial. The collimation system has to avoid that the neutron beam hits any other material besides the material used for the shielding and at the same time has to be designed in a way that its interaction with the neutron beam is minimal.

To minimize the beam related background, regions frequently hit by neutrons are shielded with the compound ^{6}LiF. This compound provides a high ratio of thermal neutron attenuation[5] through the reaction:

$$^6Li \quad + \quad n \quad \rightarrow \quad ^4He \quad + \quad ^3H \tag{4.2}$$

The tritium produced in this reaction (^3H) can produce fast neutrons of energies up to almost 16 MeV [Lon80] as well as gamma-rays, although both at a low level. For the absorption of scattered neutrons and to slow down fast neutrons boron loaded plastic, borosilicate glass, boron loaded rubber and boron loaded polyethylene are used, whereas lead-blocks absorb gamma-rays (the detailed aSPECT collimation system is shown in Fig. 2.9).

[5]Thermal neutron absorption cross section for ^{6}Li is of 940.3 barn.

Beam related neutral background

Neutral background related to the neutron beam can be due to gamma-rays and fast neutrons. To extract its contribution to the total background, measurements with and without neutron beam have been compared while keeping the magnetic field switched off. In this way, most charged particles can not reach the detector. During these measurements, the high voltage of the detector has been maintained to its nominal settings in order to compare them with other background measurements.

The resulting count rate contribution due to neutral beam related background in the PCW can not be quantified because in all cases the count rate is dominated by the thermal noise, which is of 2 s^{-1}. In BW2 the neutral beam related background contribution is less than 0.02 s^{-1}.

Beam related charged background

Beam related charged background is mainly composed of electrons from neutron decay, which is an unavoidable background. These electrons are time-correlated with the proton events. Electrons produced in the interaction of the beam with the collimation system are not correlated with the proton events, but we can not distinguish them from the decay electrons. They are, however, a few amount. Ions produced in the interaction of the beam with the rest gas molecules are another source of beam related background to be taken into account.

Decay electrons

Decay electrons are emitted isotropically and have a maximum kinetic energy of about 782 keV. One half of them travels in the direction to the mirror electrode $e1$ set at positive voltage and do not reach the detector. The other half travels towards the detector, from which, 2% have kinetic energies below 30 keV and consequently are reflected back by the high voltage electrode $e17$. In addition, in [Pet07] it has been estimated that about another 20% of those electrons traveling to the detector will be reflected by the magnetic mirror effect. The estimation has been obtained by calculating the maximum angle that the initial electron momentum can have with respect to the magnetic field lines in order to reach the detector. Assuming adiabaticity for the field ratio[6] $\frac{B_{detector}}{B_0} \approx 2$, the angle extracted is 45°. Then, taking into account the detector efficiency (between 85%-90%) and the amount of backscattered electrons from the detector (between 10% and 15%), the amount of electrons detected from the total amount generated in neutron decay has been estimated to be of about 13% [Pet07].

On the other hand, the minimum time needed for a decay proton to reach the proton detector is 5.2 μs. The time needed to detect decay electrons is much smaller because, compared with decay protons, they have higher kinetic energy and lower mass: $v_{\text{decay e}^-} \approx 1350 v_{\text{decay p}}$. In *Cycle B* data the detector dead time was set to 5 μs which implies that proton and electron from the same neutron decay can be counted as two consecutive events. Consequently, in this case, background due to decay electrons can be

[6]The magnetic moment invariance relation, Eq. 2.5, has been used.

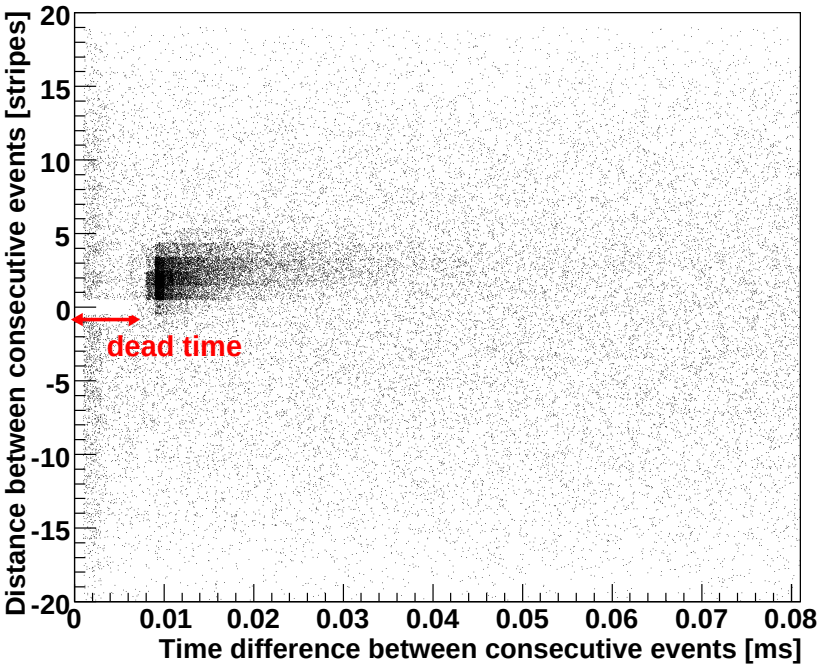

Figure 4.3: The distance (in detector stripes) between consecutive events are plotted versus their detection time difference. The data corresponds to one measurement-cycle from *0404D* and it was measured at $U_A = 50$ V and with the lower $E \times B$ set at 0/-500 V. The accumulation of events correspond to correlated electron and proton from the same neutron decay. See text for further explanation.

totally measured and subtracted from the signal. The decay electrons count rate has been determined by comparing background measurements with and without neutron beam while applying an analyzing plane voltage of $U_A = 780$ V in order to stop the protons. In those measurements the magnetic field and the high voltage were kept switched on. The comparison shows that decay electrons contribute in the PCW with about 2-3 s^{-1} and slightly less in the BW2. Most of electrons are more energetic and are detected at higher ADC-channels.

In the case of *Cycle A* data, the event length was set to 128 bins, so, the dead time of the detector electronics was 6.4 μs. This dead time is bigger than the time of flight of the fastest decay proton, 5.2 μs. Then, if a fast proton reaches the same detector stripe than the previously detected electron from the same neutron decay, the proton will not be counted. This fact would introduce a new systematic error. But the lower $E \times B$ electrode ($e8$) implemented in aSPECT almost eliminates this systematic error. The reason is that the potential applied in the lower $E \times B$ electrode shifts the protons sideways, whereas electrons are almost not shifted due to their much higher velocity. As a consequence of this, electrons and protons are detected predominantly in different detector stripes. In Fig. 4.3 it is shown the time- and channel-correlation of consecutive events for lower $E \times B$ set at 0/-500 V. This is the lowest voltage difference applied in the dipole electrode during *Cycle A* data. The applied analyzing plane voltage was 50 V. The accumulation of events

seen in Fig. 4.3 at about 7-8 μs shows the time interval between electron and proton from the same neutron decay. This accumulation disappears when applying 780 V at the analyzing plane because then no protons are detected. In this plot also the dead time after detecting the first event in the same detector stripe is visible. In the worse case, the shift in a due to undetected protons from correlated events has been estimated to be smaller than 1% [Bae08].

Positive ions from residual gas

Another source of beam related charged background are positive ions from residual gas inside the spectrometer and/or from the electrodes surface. These ions are mostly created in the decay volume from collisions of the beam products (neutrons, protons, electrons, gamma rays,...) with rest gas molecules. They are not time-correlated with decay protons. These ions are expected to have kinetic energies far below 50 eV [Glü05]. For that reason, measurements with $U_A = 0$ V are not used to extract the parameter[7] a. In case these ions manage to overcome the analyzing plane voltage, they can reach the detector and be counted as decay protons. However, in the design of aSPECT, the lower E×B electrode $e8$ has been included mainly to remove decay protons and any other beam related ionized rest gas that do not pass the analyzing plane voltage and are trapped between the mirror electrode $e1$ and the analyzing plane electrode $e14$.

4.2.4 Extra background

Summing up the different background contributions studied so far, the background count rates in the BW2 are expected to be less than 3 s^{-1}, where the main contribution is due to decay electrons. This background is not analyzing plane voltage dependent and therefore can be safely subtracted. However, in Table 4.8 it is shown that the background count rates in BW2 of the sets from *Cycle B* present often a higher count rate than the expected.

Taking a closer examination into the pulse height histograms of these cases, an **excess background** is seen in the energy range of the proton peak. An example of this excess background is shown in Fig. 4.4 where a **proton-like peak** for a $U_A = 780$ V measurement-cycle from *2604N* is centered around ADC-channel 70. The shape of the proton-like peak is similar to the proton peak. The position of the proton-like peak, determined by Gaussian fits, sometimes is the same as for the proton peak while in some cases it is shifted towards lower ADC-channels.

As long as the extra background does not depend on the analyzing plane voltage, it can be subtracted and does not add a new systematic error to the value of a. Even in case the background fluctuates non-statistically with time, its jitter will only increase the statistical error.

The angular correlation coefficient a from each measurement-cycle of *Cycle A* and *Cycle B* has been extracted assuming that the extra background is not analyzing plane-

[7]Measurements with $U_A = 0$ V are however regularly taken, since are intended to remove particles that might have been trapped between analyzing plane and the mirror electrode.

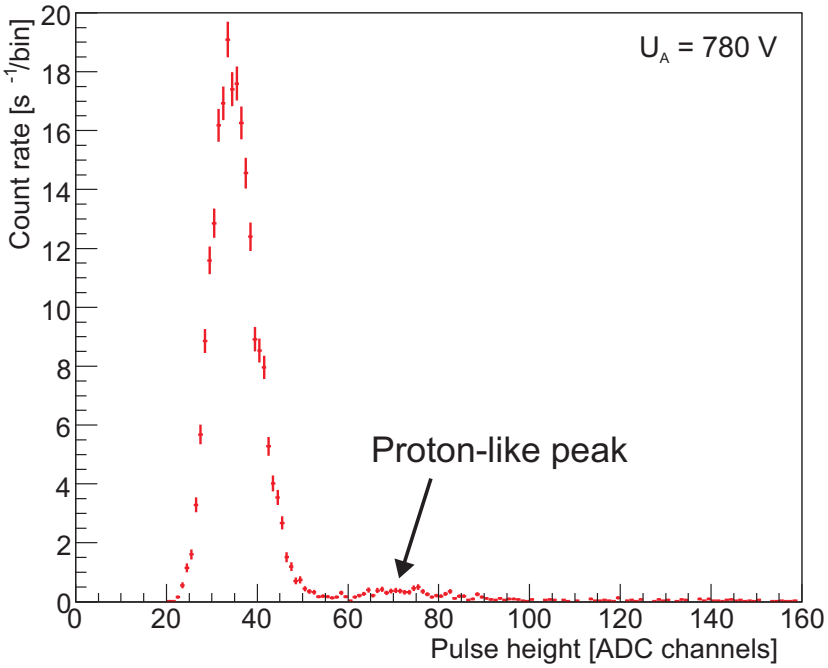

(a) Full scale graph

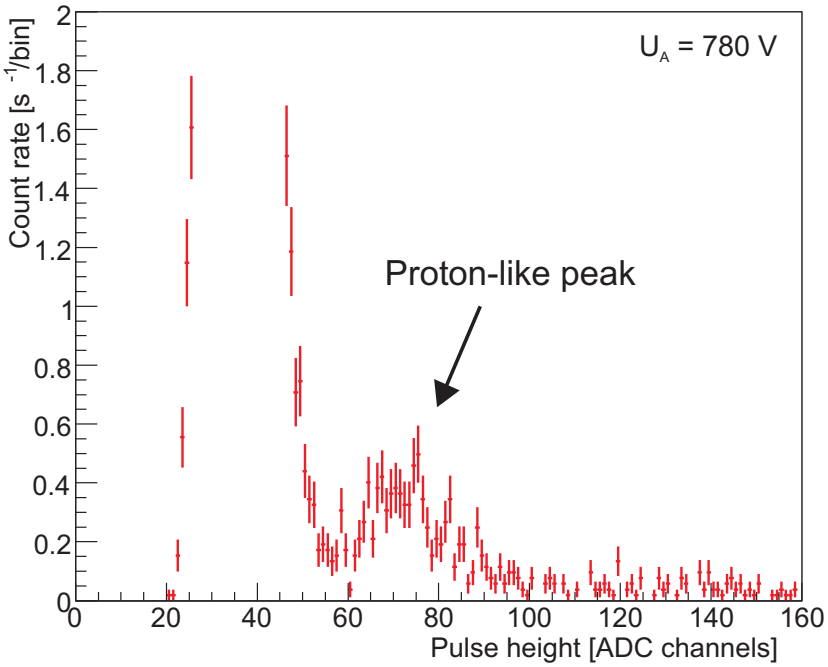

(b) Zoomed graph

Figure 4.4: Pulse height spectrum corresponding to one background measurement cycle ($U_A = 780V$) from *2604N* (*Cycle B*). The histogram contains 60 seconds of data-taking. In (a) it is shown a full-scale representation, where a proton-like peak between ADC-channels 60 and 80 is barely seen. Zooming in the count rate (plot (b)), a proton-like peak centered around ADC-channel 70 is clearly visible.

Measurement cycle	Background count rate in BW2 $[s^{-1}]$	Proton count rate for $U_A = 50V$ in PCW $[s^{-1}]$	Angular correlation coefficient a
0404D	2.49(5)	206.9(4)	-0.096(10)
0504D	2.57(4)	201.8(5)	-0.117(9)
0604D	2.96(3)	204.3(2)	-0.118(6)
2604M	4.64(5)	208.1(3)	-0.162(12)
2604N	8.43(7)	202.7(4)	-0.194(12)
2704N	3.85(7)	206.3(4)	-0.148(12)
3004D	4.51(26)	207(2)	-0.166(40)

Table 4.8: Count rates from *Cycle A* (green) and *Cycle B* (red) in the BW2 of background measurement cycles ($U_A = 780V$) and proton count rate in PCW for $U_A = 50$ V. The extracted angular correlation coefficient a is shown also for each measurement cycle. The uncertainty given is only statistical. Just for comparison, the value of a reported by the DPG is a = -0.103(4) [Ams08].

and time- dependent. The a-extraction process followed is the one described in Section 3.2.5. It uses the averaged proton count rates for each analyzing plane voltage and for each set of measurement-cycles. In *Cycle A* and *Cycle B*, the variation of the proton count rate between individual measurement-cycles is typically bigger than the statistical uncertainty, indicating the significance of non-statistical background fluctuations.

In Table 4.8 the proton count rates for $U_A = 50$ V, averaged for each set of measurement-cycles of *Cycle A* and *Cycle B* are given. The a-value extracted for each measurement-cycle is shown as well in the last column of Table 4.8.

The distribution of a-values obtained in both data Cycles is related to the background count rate in BW2 (see Table 4.8): a gets higher negative values in those measurement-cycles that have higher excess background. In order to understand this correlation, a deeper background investigation is needed.

4.3 Extracted values of a

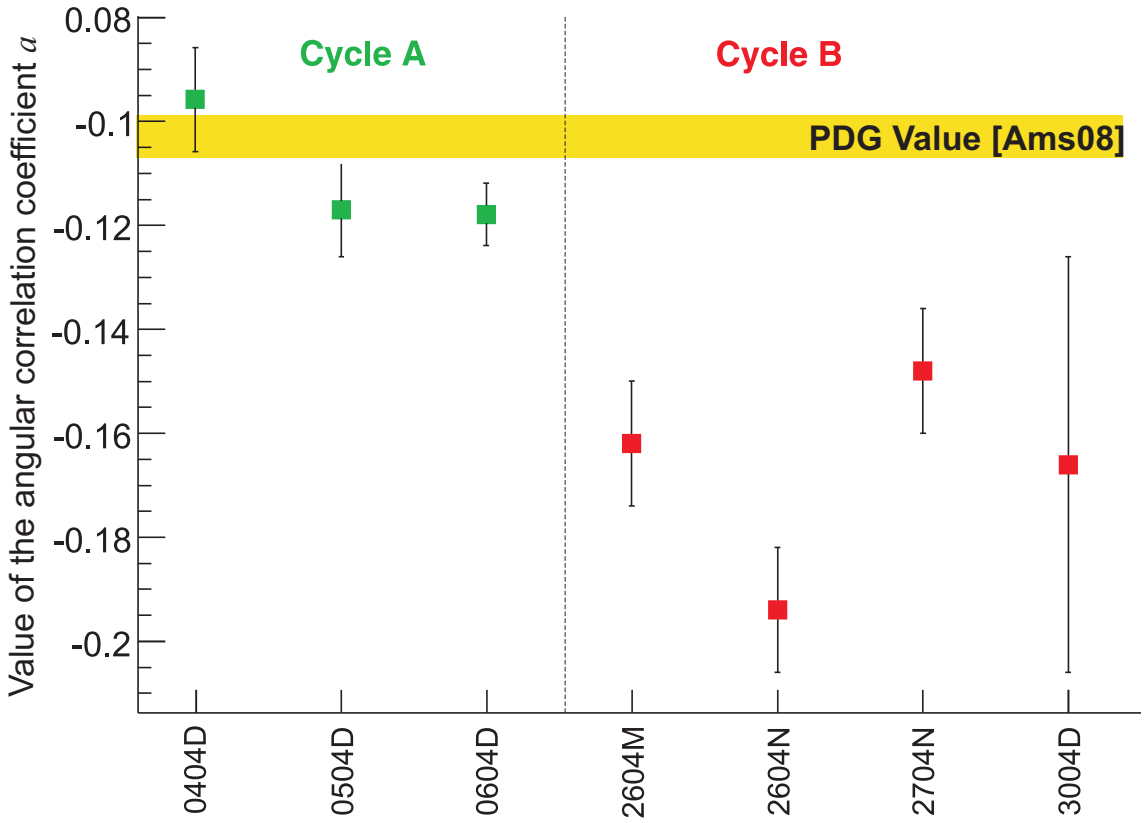

Figure 4.5: Extracted values shown in Table 4.8 of the angular correlation coefficient a for each set of measurement-cycles of *Cycle A* (in green) and *Cycle B* (in red) are represented. Only statistical errors are given.

The a-values extracted from all measurement cycles of *Cycle A* and *Cycle B* (see Table 4.8) are plotted in Fig. 4.5. The three data sets from *Cycle A* give an averaged value of $a = -0.1134(61)$, where only the statistical uncertainty is given. This result is in good agreement with the current Particle Data Group value, $a = -0.103(4)$ [Ams08]. The averaged value of a from the sets of *Cycle B* is $a = -0.168(11)$, which is clearly more negative than the PDG value.

Differences between the sets of measurement-cycles from *Cycle A* and from *Cycle B* data have been observed in the background count rate under the proton peak, i.e., in BW2 (see Table 4.8). There exists an excess background in BW2 much bigger for *Cycle B* than for *Cycle A* data.

The variation of the value of a for each set of measurement-cycles with the background count rate in BW2 is represented in Fig. 4.6. Sets of measurement-cycles where the proton-like peak is not visible are the ones with lower background count rate in BW2, and also with an extracted a-value closer to the current PDG's a-value [Ams08].

On the other hand, an unexpected proton-like peak is visible in pulse height spectra with $U_A = 780$ V of *Cycle B* data. Pulse height spectra for $U_A = 780$ V from *Cycle A*

do not present a *visible* proton-like peak (see Fig. 4.7), although this does not prove that there are no contributions of the excess background.

The shift of a to negative values for those measurements with higher background count rate in BW2, as can be seen by comparison with Figure 2.4, is an indication that either high energetic decay protons are not detected or that there exists an excess of low energy protons or some other kind of positively charged particles.

As can be seen from Table 4.8 and Fig. 4.6, the shift of the extracted values of a is correlated with the extra background count rate, introducing an additional systematic error. Therefore, without a proper background correction a definitive value for the neutrino electron angular correlation coefficient a can not be extracted from the first test of the spectrometer aSPECT at FRM-II.

In following chapter, the data taken during these beam times will be further analyzed in order to identify the sources of the extra background and of the count rate fluctuations.

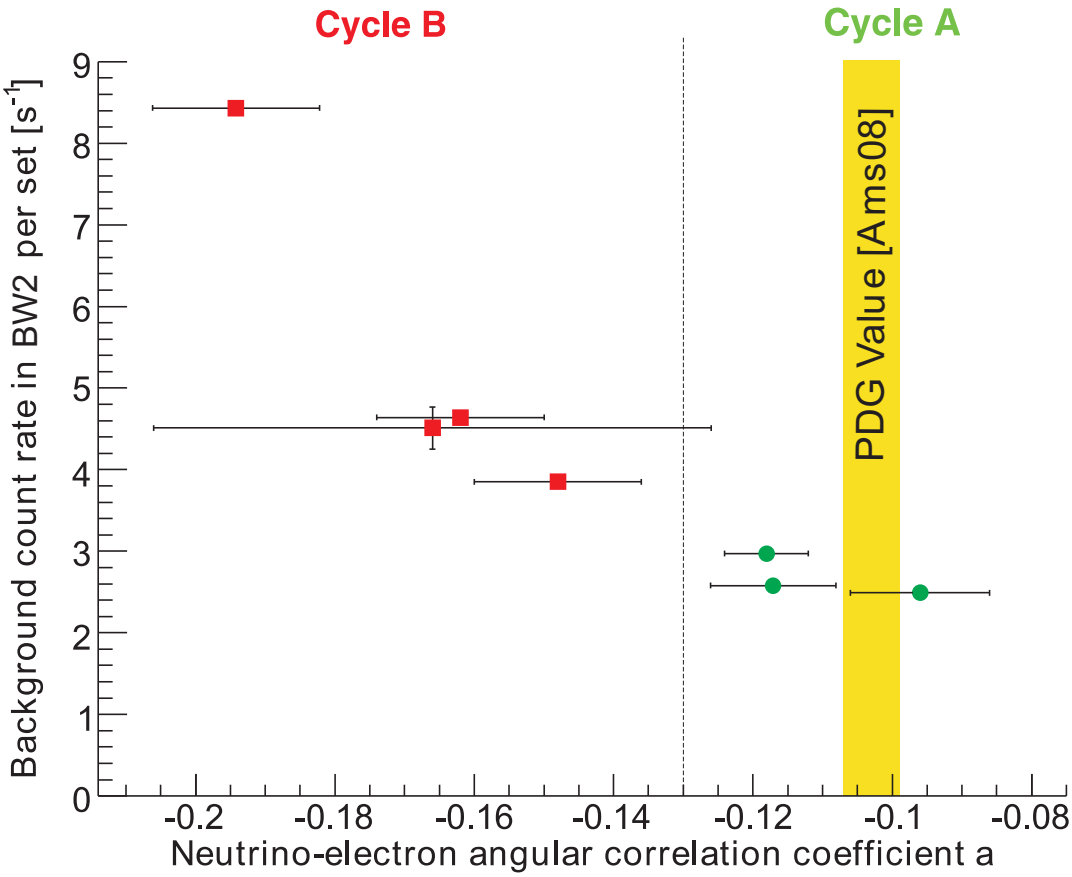

Figure 4.6: Angular correlation coefficient a values extracted from sets of measurement-cycles from *Cycle A* and *Cycle B* are plotted versus their averaged background count rate in BW2. Please note, that a-values from *Cycle A* data are found closer to the PDG's a-value [Ams08], whereas a-values from *Cycle B* tend to be more negative. Error bars contain only the statistical errors.

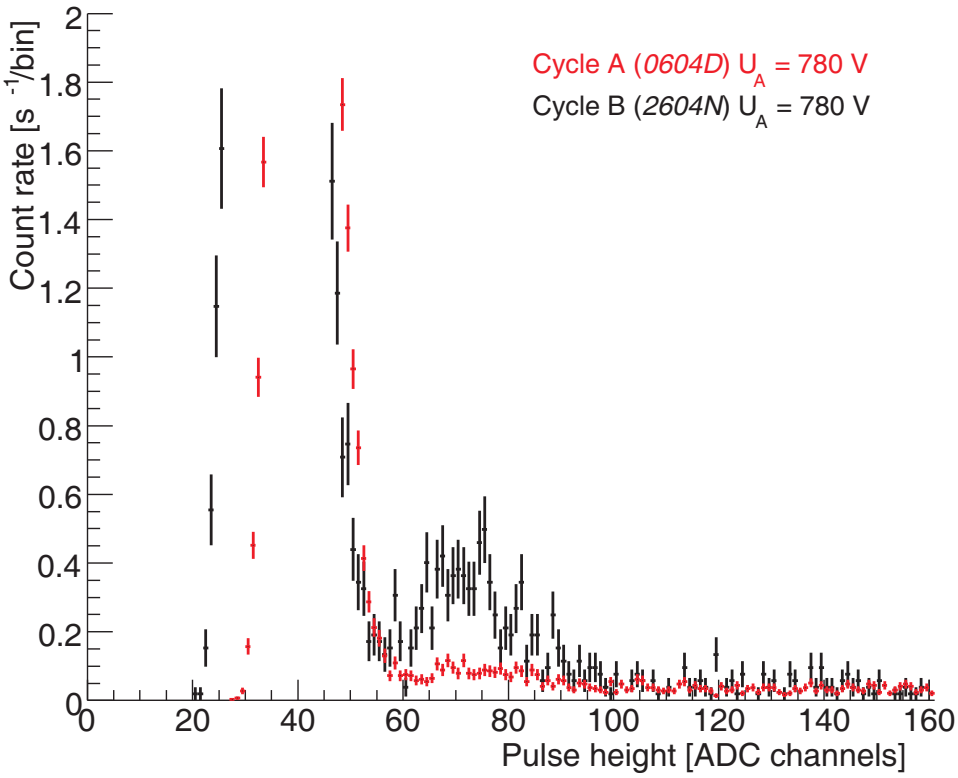

Figure 4.7: Pulse height histograms of two measurement-cycles at $U_A = 780$ V zoomed in the count rate axis to a maximum of 2 s^{-1}/bin. The red pulse height histogram corresponds to the set of measurement-cycles *0604D* (*Cycle A*), in which a proton-like peak is at least not *visible*. The black pulse height spectrum corresponds to *2604N* (*Cycle B*), in which a small proton-like peak is clearly observed.

Chapter 5

Proton-like background studies

In the previous Chapter the Background Study Window BW2 has been used to extract the background count rate on the proton peak region, or proton-like background. In this window non-statistical count rate fluctuations in all studied sets of measurement-cycles have been found. Additionally, in some sets an excess background count rate with a peak shape, the so-called proton-like peak, has been observed.

In *Cycle B* data, once the proton-like peak appears (in a *visible* way), it can persist for periods of more than 24 hours. When ramping down the main magnetic field or the voltage applied in all electrodes the proton-like peak disappears. When ramping the magnetic field and the voltage up again the proton-like peak sometimes appears again, although its amplitude can be different from before.

In order to understand better the origin of the excess background in BW2, investigations of dependencies of the background count rate in BW2 on several parameters have been performed. The results are summarized in this Chapter. The aim is to find out the characteristic conditions in which the excess background and the non-statistical fluctuations are observed in order to understand the mechanism that produces them. For this objective, additional auxiliary sets of measurement-cycles taken during the fourth beam time have been used besides the sets of measurement-cycles from *Cycle A* and *Cycle B*. The detailed experimental conditions and settings of these auxiliary-sets are given in Appendix A.

5.1 Proton-like background dependencies

5.1.1 Analyzing plane dependence

In the firsts data taking periods (or beam times) of the *a*SPECT spectrometer, performed at FRM-II, the beam-related background count rates were expected to be constant for all applied analyzing plane voltages U_A [Glü05]. Consequently, during the measurements only background measurement-cycles at $U_A = 780$ V have been taken. Background measurements for any other analyzing plane voltage almost do not exist.

Because of the unexpected excess background and the non-statistical count rate fluctuations in BW2 observed in some measurement-cycles, a possible dependence of the proton-like background on the analyzing plane voltage can not be discarded *a priori*.

To investigate the analyzing plane dependence of the proton-like background only the set of measurement-cycles *2604Nnobeam* is available. This data was taken within the set of measurement-cycles of *Cycle B 2604N* for a time of about 30 minutes, while the neutron beam was switched off. During this period the DAQ system was not interrupted, but it continued taking data as usual. Hence, *2604Nnobeam* contains measurement-cycles without neutron beam and for different analyzing plane voltages, with both, magnetic field and electrodes' voltages switched on. Notice that this data was taken during the period with one of the highest background count rate measured in BW2 at $U_A = 780V$ (see Table 4.8).

Averaged count rates in BW2 and PCW for several analyzing plane voltages from *2604Nnobeam* data are shown in Table 5.1. Notice the increase of the count rate in BW2 when increasing the analyzing plane voltage. This indicates the existance of an additional analyzing plane voltage dependent background, which is illustrated in Fig. 5.1.

Analyzing plane Voltage [V]	Total measurement-cycles	Count rate in BW2 [s^{-1}]	Count rate in PCW [s^{-1}]
0	7	1.30(12)	48.8(5)
50	2	1.43(10)	49.3(6)
400	1	2.55(20)	50.4(9)
500	1	2.33(20)	51.4(9)
600	1	4.30(29)	52.6(1.0)
780	7	4.34(29)	53.4(8)

Table 5.1: Averaged count rates in BW2 and PCW of measurement-cycles from *2604Nnobeam* for different analyzing plane voltages. During this set of measurement-cycles the neutron beam was switched off. The count rate uncertainty is only statistical.

Figure 5.2 shows the pulse height histograms of measurement-cycles from *2604Nnobeam* for different analyzing plane voltages, zoomed in the BW2 region. It is also visible that the amplitude of the proton-like peak increases when increasing the analyzing plane voltage.

Unfortunately, sets of measurement-cycles comparable to *2604Nnobeam* do not exist. However, it is possible to make use of the auxiliary set of measurement-cycles *2604Background*, taken between the sets *2604M* and *2604N*. This measurement was intended to study the background without neutron beam for $U_A = 0$ V and $U_A = 780$ V, so it can be used for a further analyzing plane voltage dependency check.

The averaged count rate in BW2 for both analyzing plane voltages $U_A = 0$ V and $U_A = 780$ V from *2604Background* are plotted in Fig. 5.3 (a). The count rates at $U_A = 0$ V extracted from *2604Background* and *2604Nnobeam* are very similar, about 1.2 s^{-1}. Also, like in *2604Nnobeam*, the count rate at the proton peak position is bigger for $U_A = 780$ V than for $U_A = 0$ V. But compared with *2604Nnobeam*, in *2604Background* the count

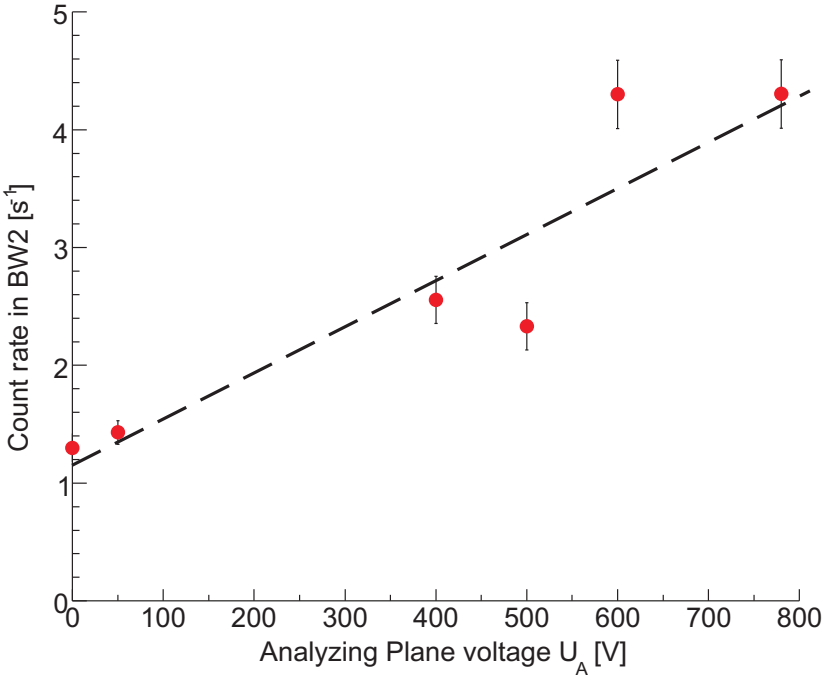

Figure 5.1: Averaged count rates in BW2 corresponding to measurement-cycles from *2604Nnobeam* measured without neutron beam for different analyzing plane voltages, see Table 5.1. The count rate increases when increasing the analyzing plane voltage.

rate increase for $U_A = 780$ V measurements is rather small. Further, as it is shown in Fig. 5.3 (b), the proton-like peaks at both, $U_A = 0$ V and $U_A = 780$ V, are not so prominent. Therefore, the additional analyzing plane voltage dependent background is not stable in time.

The background measurements without beam *2604Nnobeam* plotted in Fig. 5.1 have been used in a first attempt to correct the background subtraction from the measured count rates *2604N*. Since the background count rate measured without beam is bigger at higher analyzing plane voltages, the data from *2604N* has been reanalized by applying a more appropiate background subtraction. The background subtraction applied to the PCW count rate extracted from each measurement-cycle of the set *2604N*, for a given U_A setting, is the following[1]:

$$\begin{aligned} \#_{\text{PCW background free}}(U_A) = \quad & \#_{\text{Beam ON}}(U_A) - \#_{\text{Beam ON}}(U_A = 780V) \\ & + \#_{\text{Beam OFF}}(U_A = 780V) - \#_{\text{Beam OFF}}(U_A) \end{aligned} \tag{5.1}$$

where # indicates the amount of count rate $[s^{-1}]$. Here it is assumed that the analyzing plane voltage dependence of the extra background with neutron beam on is the same as

[1]The background measurements without beam *2604Nnobeam* do not contain measurement-cycles for all the analyzing plane voltage settings used during *2604N*. The missing values have been evaluated from a linear fit to the count rates of the existing measurements of *2604Nnobeam* (see Fig. 5.1).

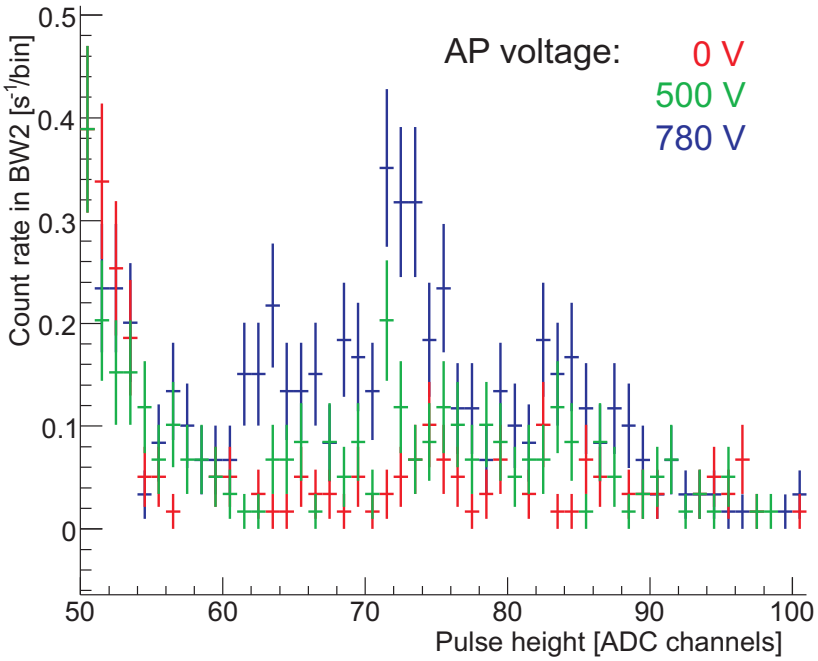

Figure 5.2: Pulse height histograms zoomed in BW2 taken without neutron beam and for different analyzing plane voltages. Data from the auxiliary set *2604Nnobeam*. The excess background has a proton-like peak shape and increases when increasing the analyzing plane voltage.

the one observed without beam.

The value of a extracted for the measurement cycle *2604N* shown in Table 4.8 and in Fig. 4.5, is $a = -0.194(12)$. After the background correction (using Eq. 5.1), the a-value extracted increases +15% with respect to the not corrected value (i.e., the absolute value increases by +0.03 to about a = -0.164). Therefore, the corrected a-value extracted is shifted to the positive value direction, coming closer to the a-values extracted from *Cycle A*, where this big amount of excess background was not observed (see Fig. 4.5). The direction of the shift is in agreement with the initial assumption, in which it was considered that the background subtracted to low analyzing plane voltage measurements was overestimated.

The result of this estimation shows that the beam-related background is not constant but dependent on the analyzing plane voltage settings, U_A. However, due to count rate instabilities in the set of measurement-cycles *2604N*, to extract a definitive background corrected a-value from this set more background measurements without beam at different analyzing plane voltages would be needed. In addition, it is not obvious that the extra background behaves in the same way with the neutron beam on like with the neutron beam off. Given these two observations the goal for future measurements with aSPECT has to be to eliminate or reduce the extra background instead of trying to correct it.

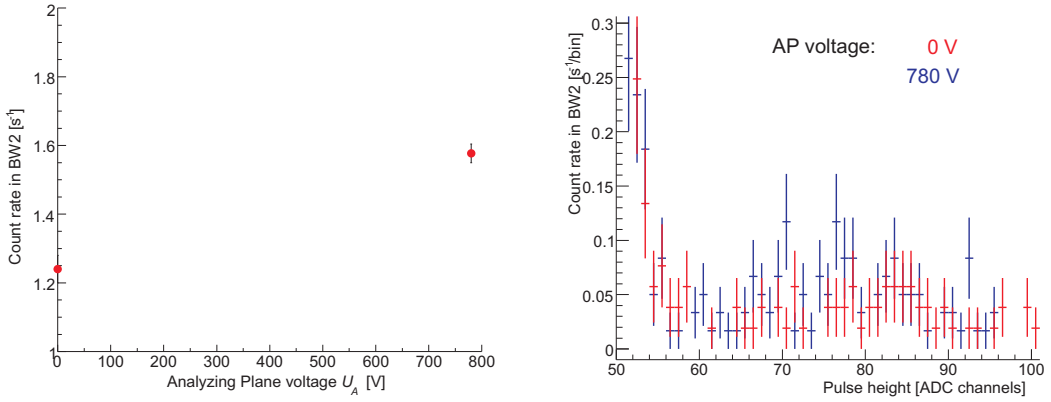

(a) (b)

Figure 5.3: Auxiliary data sets measured without neutron beam *2604Background* for analyzing plane voltages $U_A = 0$ V and $U_A = 780$ B. (*a*) shows their averaged count rate in BW2. (*b*) shows their corresponding pulse height spectra in the BW2 region.

From the available measurements without neutron beam it has to be concluded that the count rate in BW2 depends on the analyzing plane. These background spectra contain a proton-like peak shape whose amplitude increases when increasing the analyzing plane voltage.

The fact that the background is dependent on the analyzing plane voltage even when the neutron beam is off, can indicate the presence of stored and/or trapped particles in the spectrometer (as will be discussed in Section 5.2).

5.1.2 Count rate variation with leakage current

During the last data-taking period at FMR-II, the stability of the high voltage power supply system was improved and high voltage breakdowns at the detector region were less frequent than during the previous data-taking periods. Nevertheless, discharges continued taking place every now and then.

Most of the breakdowns were observed at the high voltage detector electrode *e*17. They were preceded by some seconds during which the leakage current measured at the high voltage power supply was up to five times higher than the nominal averaged rate, which was about 0.5 ± 0.2 μA. The nominal averaged leakage current rate was dominated by the leakage current produced in the high voltage cable which, in addition, fluctuated in time. For that reason, the sensitivity of our leakage current monitor to the leakage currents inside the spectrometer was limited. Only high leakage currents at the detector electrode could be monitored quantitatively.

In some occasions in which the leakage current rate was higher than usual (typically between 1 and 2.5 μA), but not high enough to produce a big discharge, an increase of the background count rate in BW2 was observed. Furthermore, this excess background showed a hysteresis behaviour. It did not necessarily disappear once the leakage current

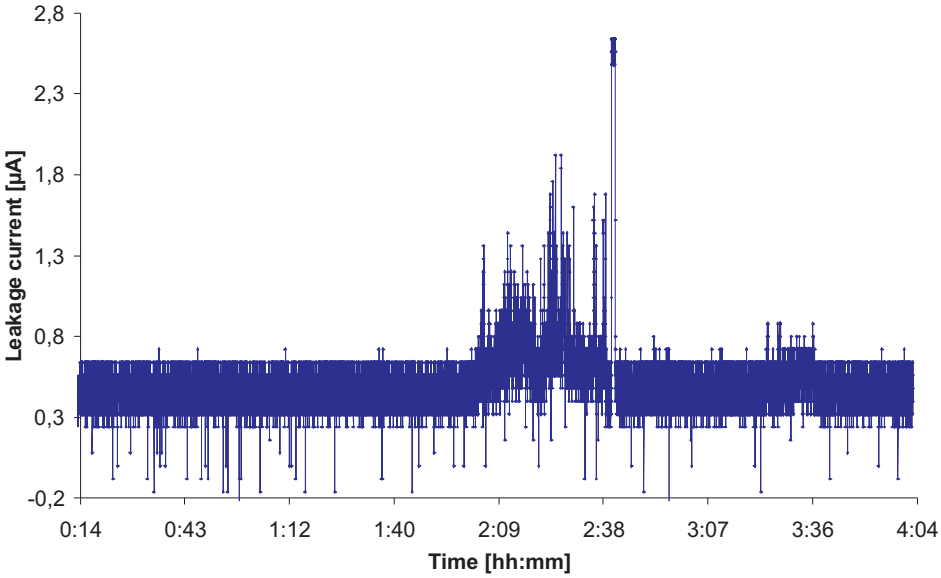

(a) Leakage current variation with time.

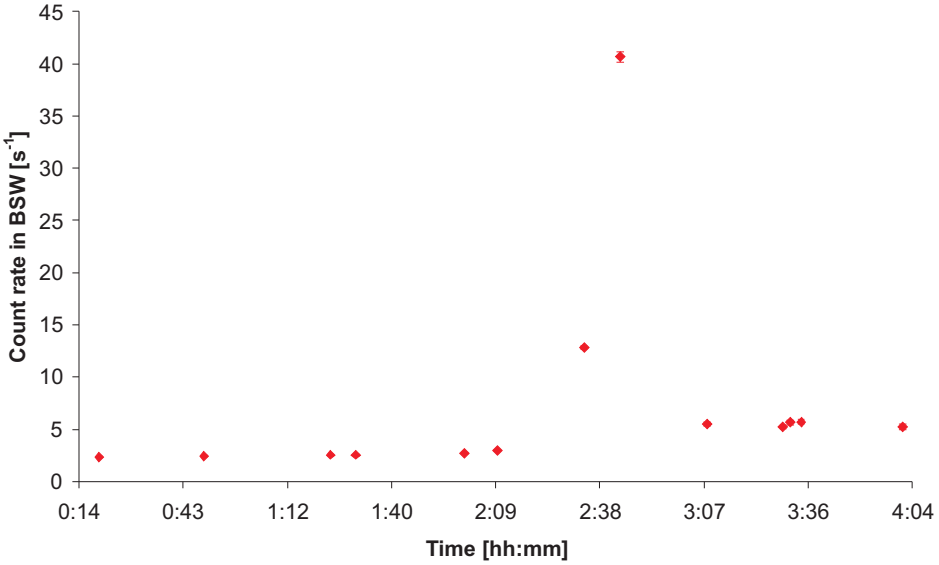

(b) Averaged background count rate in BW2 per measurement-cycle represented on the measurement time scale.

Figure 5.4: Dependence of the background count rate (U_A = 780 V) in BW2 on the leakage current from the high voltage electrode $e17$. Data from the auxiliary set *2504S*.

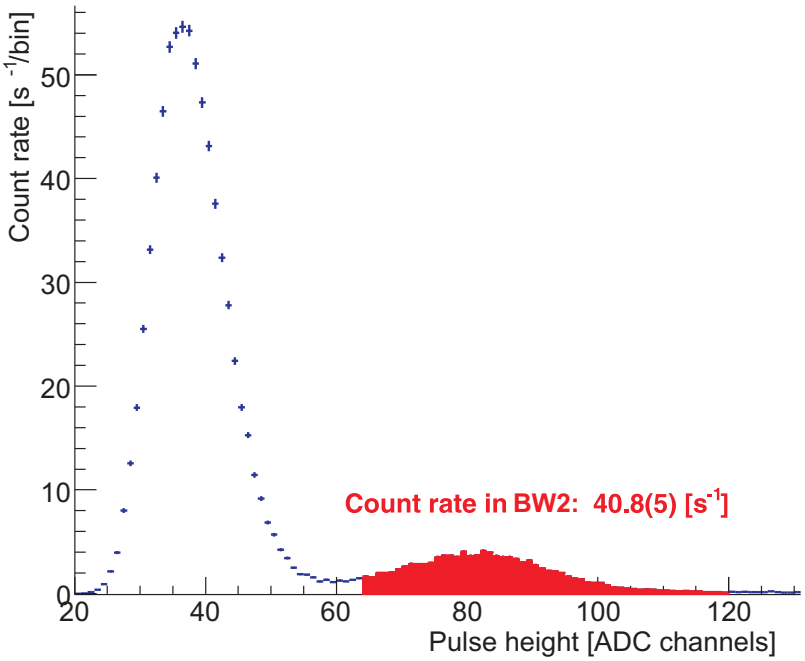

Figure 5.5: Pulse height histogram at $U_A = 780$ V corresponding to the measurement-cycle with highest count rate in BW2 from the auxiliary-set *2504S*. During this measurement, the leakage current was increased (see Fig. 5.4). A proton-like peak can be clearly seen in BW2.

was restored to normal values. Moreover, the background count rate could be either higher or lower than before. In addition, it was as well observed that by ramping down the voltage on all electrodes (including the detector high voltage), or ramping down the magnetic field, this excess background disappeared.

The clearest example of excess background by periodes of high leakage current rates is shown in the auxiliary set of measurement-cycles *2504S*. These measurement-cycles were intended to optimize the voltage applied on the upper E×B electrode ($e16$) for a better centering of the beam into the detector.

In Fig. 5.4 (a) it can be seen that during the measurement of *2504S*, a period of high leakage current started at around 2:00 and lasted about 40 minutes. During this time two measurement-cycles at $U_A = 780$ V were performed. Both of them show an unusual high count rate in BW2, as can be seen in Fig. 5.4 (b). The pulse height histogram of the measurement-cycle with the highest count rate is plotted in Fig. 5.5, where a huge proton-like peak is seen even at a full scale plot. From Fig. 5.4 it can be further demonstrated that before the high leakage current period the background count rate was stable and of about 2.5 s^{-1}. After this period, the count rate in BW2 was stabilized to about 5.5 s^{-1}. Therefore the background count rate in BW2 show a hysteresis behavior after leakage current periods.

However in the sets of measurement-cycles used to extract a from *Cycle A* and *Cycle B* data no high leakage current rates have been observed over long periods of time. Only sporadic high leakage current rates for short intervals of time have been detected in some of those sets, mainly from *Cycle B* sets. *2604M* is the set of measurement-cycles with the

highest leakage current rate periods. In Fig. 5.6, the variation of the leakage current with time from a part of this set is plotted. In the graph the background count rate in BW2 for each individual measurement-cycle is shown. In contrast with the measurement *2504S* (Fig. 5.4), in this case, within statistical fluctuations, no correlation between background count rate and leakage current are seen for *2604M*. This non-observation can be either due to the insufficient sensitivity of the current monitor or to the fact that the excess background rate is constantly increased (e.g., due to a previously not recorded high leakage current period). Also in the rest of measurements of *Cycle B* data no correlation between the leakage current rate and the excess background count rate in BW2 has been observed.

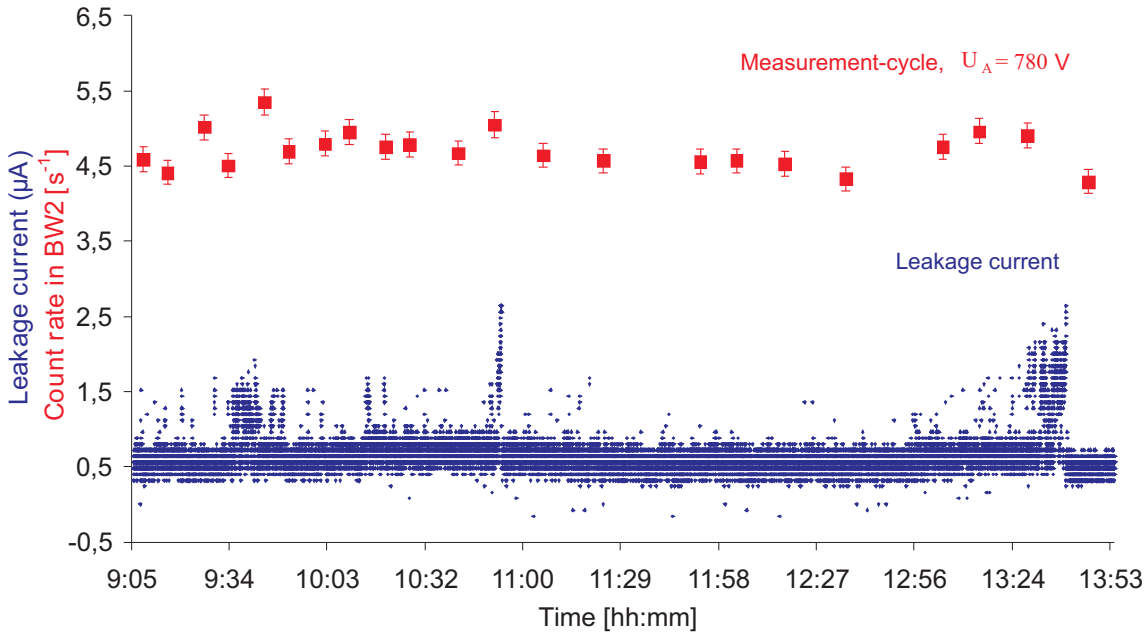

Figure 5.6: The leakage current rate during a part of the measurement *2604M* is plotted versus time. Further, the averaged count rate in BW2 of each individual measurement-cycle from the set are additionally shown. In this case, within the statistical fluctuation, no correlation of the count rates with the high leakage current periods is seen.

The increase of the leakage current rate observed sometimes could be explained by field emission processes on the electrodes from the detector area, which are those held at high voltage. Electrons that reach the tube flux in the detector region originated, for instace, by field emission would travel towards regions held at less negative potential, i.e., towards the mirror electrode direction. On their way, these electrons could ionize rest gas atoms and/or hit the inner walls of the electrode system and produce secondary electrons. The secondary electrons again could ionize rest gas molecules. The fact that positively charged particles are accelerated to the detector could explain the correlation between high leakage current and the increase of the excess background rates observed in some of the cases.

5.2 Particle traps in the spectrometer

In the last Section it has been discussed the dependence of the excess background count rate with the analyzing plane voltage when the neutron beam was switched off as well as its influence with the observation of leakage current periods. The explanation for both observations could be related to trapped particles in the spectrometer.

In *a*SPECT exist Penning-like traps[2] formed by the axial magnetic field and by the electrode system. These traps could affect both positively and negatively charged particles. In Fig. 5.7 the possible location of Penning-like traps in the *a*SPECT spectrometer and the axial electric field profile for positively and negatively charged particles are shown.

For a given magnetic field configuration, the Penning-like traps existing in the *a*SPECT spectrometer can be classified as follows:

- **P-I trap** for **negatively** charged particles: It is formed on the edges between electrodes *e16* and *e17*. The trap depth will depend on the voltage applied to both electrodes of the upper E×B (electrode *e16*), and on the detector electrode *e17*. The presence of this trap is not obvious. It has been found after simulating the electromagnetic fields in this area [Kon10b]. This trap affects to negatively charged particles, but only those off-axis.

- **P-II trap** for **negatively** charged particles: It is formed between the electrodes of the lower and upper E×B, *e8* and *e16*. The trap depth depends on the voltage applied to both electrodes of the lower and upper E×B but also on the analyzing plane electrode *e14*.

- **P-III trap** for **positively** charged particles: It is formed in the region between the mirror electrodes ($e1$ and $e2$) and the analyzing plane electrode $e14$. The trap depth depends on the voltage applied to the mirror electrodes and to the analyzing plane electrode, but also on the voltage applied to both sides of the lower E×B electrode *e8*.

- **P-IV trap** for **negatively** charged particles: It is formed between the bottom plate of the electrode system and the decay volume (electrode $e6$). Both electrodes are grounded. The trap depth depends on the voltage applied to the mirror electrodes $e1$ and $e2$.

[2] A Penning trap consists of a strong homogeneous axial magnetic field that confines charged particles radially while a quadrupole electric field confines them axially [Pen36] [Deh67]. Typically, the static electric potential is generated using a set of three electrodes: a central ring and two endcaps. To trap positively (negatively) charged particles, the endcap electrodes are kept at positive (negative) potential relative to the ring.

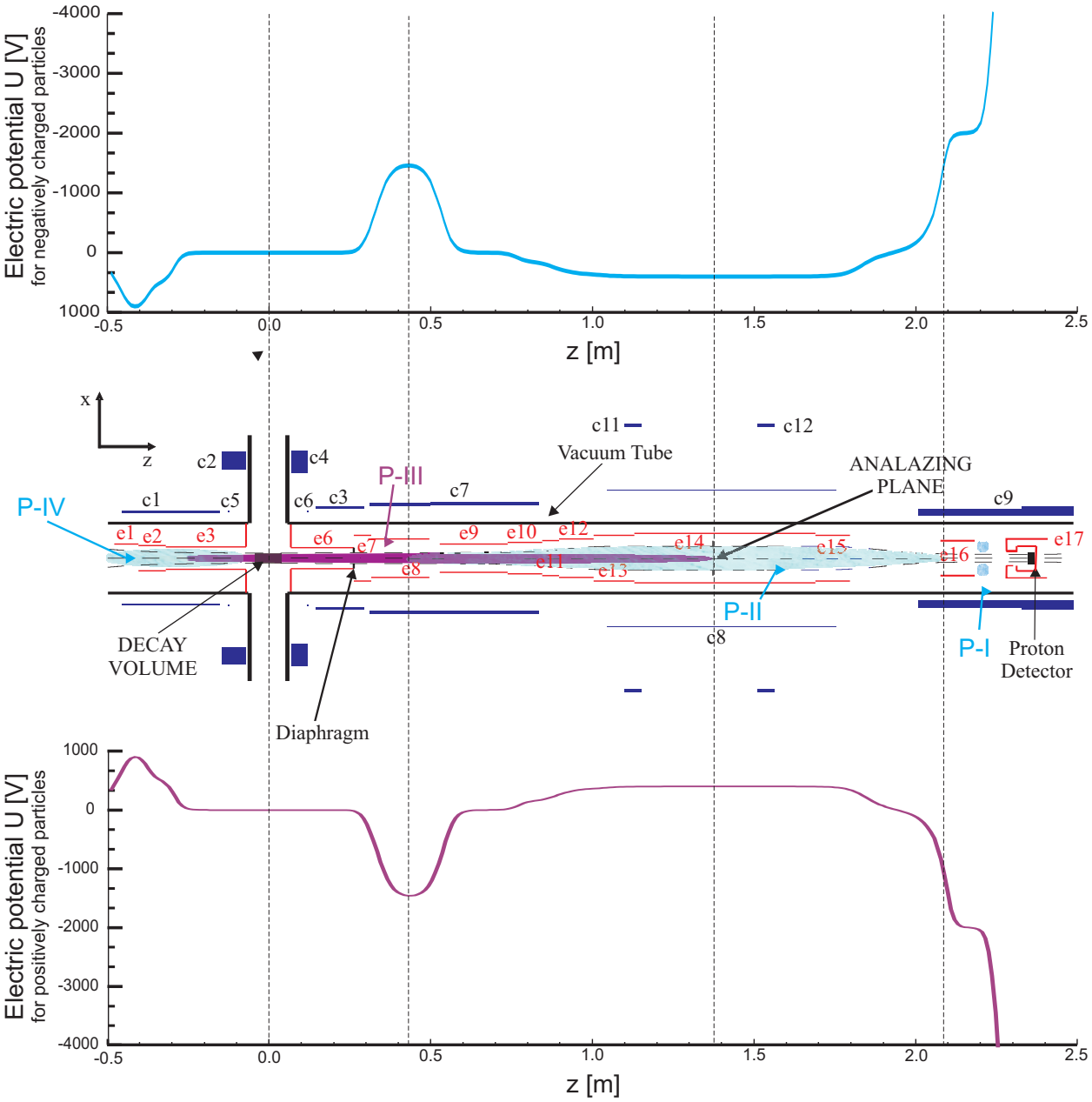

Figure 5.7: In the center it is plotted the scheme of the arrangement of the magnetic coils and electrodes in the *a*SPECT spectrometer. The regions that favor the trapping of particles have been colored. Blue regions can trap negatively charged particles. Purple regions can trap positively charged particles. Notice that both regions have overlaps. The axial electric field profile is plotted above for negatively charged particles and below for positively charged particles.

Therefore, in total, in the *a*SPECT spectrometer there exists 3 Penning-like traps for negatively charged particles and one for positively charged particles. There are also two regions in which negatively and positively charged particles overlap and where the probability of collisions and of ionization processes can be higher.

In fact, in the design of *a*SPECT, the lower E×B drift electrode *e*8 was installed with the aim to remove the decay protons which do not pass the analyzing plane barrier and any other beam related ionized rest gas that is trapped in P-III (see Section 2.4.3). Trapped particles with positive charge that scape from P-III will depend on the analyzing plane voltage. But the dependence of these particles on the analyzing plane voltage behaves opposite to what is observed in the background measurements for different analyzing plane voltage settings. For a low analyzing plane voltage the positively charged count rate that escape from P-III is bigger. Thus, the origin of the excess background is quite improvable provided by beam-related particles trapped between the mirror and the analyzing plane electrode.

On the other hand, traps for negatively charged particles a priori should not play a role in the background creation since decay electrons are too energetic to be confined in them.

But if negatively charged particles of low energy would be present inside the spectrometer, they could be stored in these Penning-like traps. Hereafter, they would ionize rest gas and create positively charged ions. The ions could then reach the detector and create the excess background. The dependence of this excess background on the analyzing plane voltage settings would behave like the one observed in the measurements. That is because the negatively charged particle traps are deeper for higher analyzing plane voltages and then, more positively charged ions are created.

In the following Section the possible mechanisms that can produce a source of negatively charged particles of low energy inside the spectrometer are discussed from a qualitatively point of view.

5.3 Origin of the excess background

Most electrons produced in neutron decay have enough energy not to be confined in the spectrometer traps. Actually, if decay electrons would be stored in these traps, an excess background dependence on the neutron beam should be observed. This is not the case. See for example, Fig. 5.1, in which excess background is seen when the neutron beam is switched off.

Other alternative processes from which electrons can be created and that could occur in the spectrometer when applying high voltages are, for example:

- **Field emission** from the upper E×B ($e16$) and the detector-electrode ($e17$).

- **Penning discharge** between electrodes $e16$ and $e17$.

Both processes are facilitated by electrode surface irregularities (tips, micro-points,...) which create local electric fields much larger than the global electric field applied to the electrode. In field emission, electrons are emitted due to quantum mechanical tunneling out of the metal in presence of a high electric field [Fow28]. The origin of Penning discharges are charged micro-particles that hit the electrode surface giving rise to local heat shocks. Such collisions produce locally evaporated material which causes a local degradation of the vacuum, initiating a breakdown in a gap between electrodes. Electron field emission and micro-particle bombardment tend to appear together. Typically, field emission processes dominate in the case of small cathode-anode gaps, while Penning discharges are more important for larger gaps.

It is assumed, that in aSPECT, either one or both of these two mechanisms act as a primary source of electrons. These electrons can travel through the whole spectrometer, accelerated by the high voltage from electrodes $e16$ and $e17$, towards the mirror electrode $e1$ (set at +1 kV). On their way, a part of the electrons can create secondary electrons by ionizing residual gas particles or by colliding with the electrode walls. Secondary electrons have less energy and can be more easily trapped in Penning traps, in which they can produce positive ions by means of rest gas ionization. If these positive ions reach the detector, they will be counted as normal events. The two-plate shaped upper E×B electrode, by means of tangential electric fields, could even contribute in guiding these positive ions to the detector by moving them radially to the center of the flux tube within the spectrometer.

With this presumption, during high leakage current periods the amount of primary electrons is increased. Consequently, the number of secondary electrons trapped in Penning traps is also increased, resulting in an increment of the detected excess background. This is exactly the behavior that was observed experimentally.

5.4 Processes of excess background production

The creation of the excess background is believed to be related with the presence of several Penning-like traps inside the *a*SPECT spectrometer together with a low energy electron source whose origin is independent on the neutron beam. In the following, based on the observed analyzing plane voltage dependence of the excess background, an attempt is made to identify in more detail the mechanisms involved in the excess background production.

5.4.1 Excess background and analyzing plane voltage: traps P-II and P-III

The observation that there is more excess background at higher analyzing plane voltages (see Fig. 5.1 and 5.2) indicates that trap **P-II** plays an important role in the production of the excess background. This trap is deeper if the analyzing plane voltage, U_A, is increased. Consequently, for higher analyzing plane voltages the amount of particles trapped in **P-II** as well as the ionizing processes will increase.

The settings of the lower E×B electrode ($e8$) influence as well the **P-II** trap depth. Applying a more negative potential on both sides of $e8$ increases the **P-II** trap strength to attract secondary electrons. Then, for a fixed analyzing plane voltage U_A an increase of the excess background is expected when making the potential in $e8$ more negative. However, there are no measurements that can clearly prove this hypothesis.

On the other hand, the measurements from *Cycle A* and *Cycle B* show an increase of the background count rate taken at $U_A = 780$ V when decreasing the potential difference between both sides of the lower E×B. As presented in Tables 4.2 and 4.3, the potential difference in the lower E×B was set between -500 and -700 V for *Cycle A* and at -150 V for all measurements of *Cycle B*. Figure 5.8 *a* and *b* show that the BW2 count rate at $U_A = 780$ V is higher in *Cycle B* measurements. The projected shape on the detector in *Cycle B* measurements show in addition a clear accumulation of events in the center of the detector, which is not seen in *Cycle A* measurements.

The higher count rate observed for smaller potential differences at the dipole $e8$ (see Fig. 5.8) can be explained by an insuficient removal of trapped particles in **P-II** and also **P-III**. Trapped particles between mirror electrode and analyzing plane electrode are removed more slowly when the potential difference applied between both sides of the lower E×B is small. In that case, particles need to pass more times the lower E×B in order to be removed from the flux tube. Therefore, they have a higher probability to participate in ionization processes and produce extra background.

There are not enough measurements to understand more qualitatively the accumulation of particles in the center of the detector, as shown in Fig. 5.8 *b*. But since this accumulation is not observed in Fig. 5.8 *a*, it could be due to the influence of traps **P-II** and **P-III**. This hypothesis is as well supported by measurements without mirror electrodes (i.e., with $e1$ and $e2$ switched off). Under such conditions traps **P-III** and **P-IV** should not exist. Two measurements without mirror electrodes (*2904M* and *2904T*) were

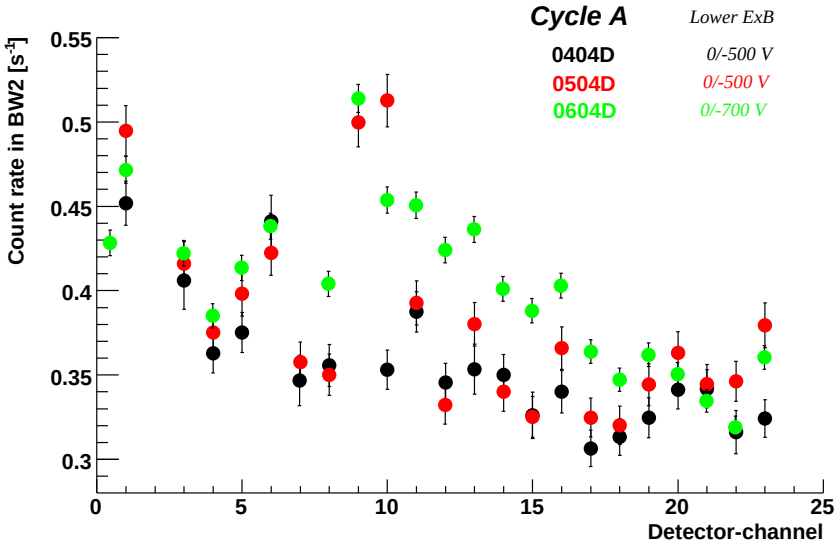

(a) *Cycle A*

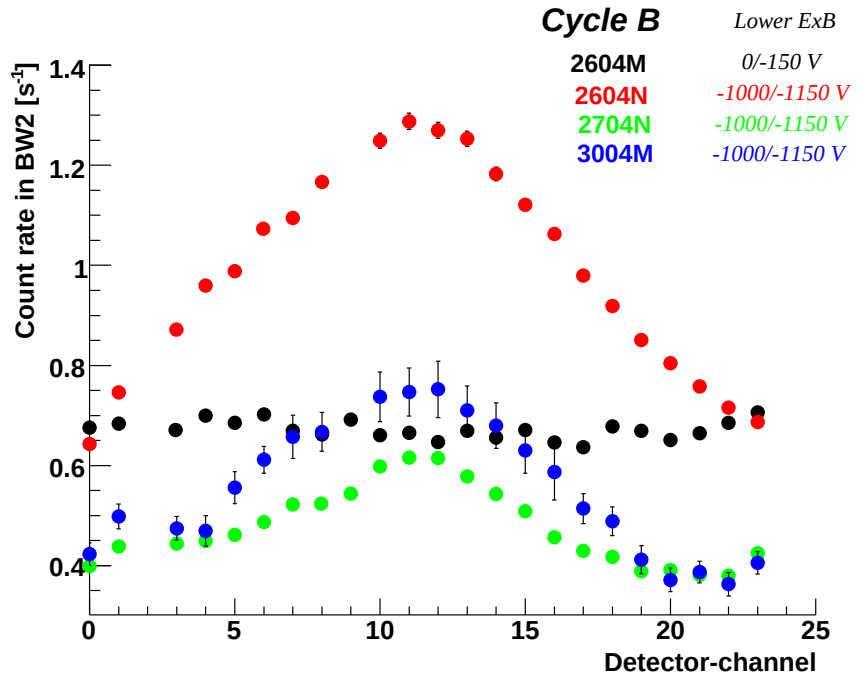

(b) *Cycle B*

Figure 5.8: Averaged background count rate ($U_A = 780$ V) in BW2 per detector-channel for the sets from *Cycle A* and *Cycle B*. The lower E×B electrode settings used in each set is indicated. Please notice that the background count rate is bigger for *Cycle B* sets, which are those sets with smaller voltage difference between both electrodes in the lower E×B. In addition, *Cycle B* sets tend to show a ∩-shape distribution, while *Cycle A* sets do not show a well defined shape. See text for further discussion.

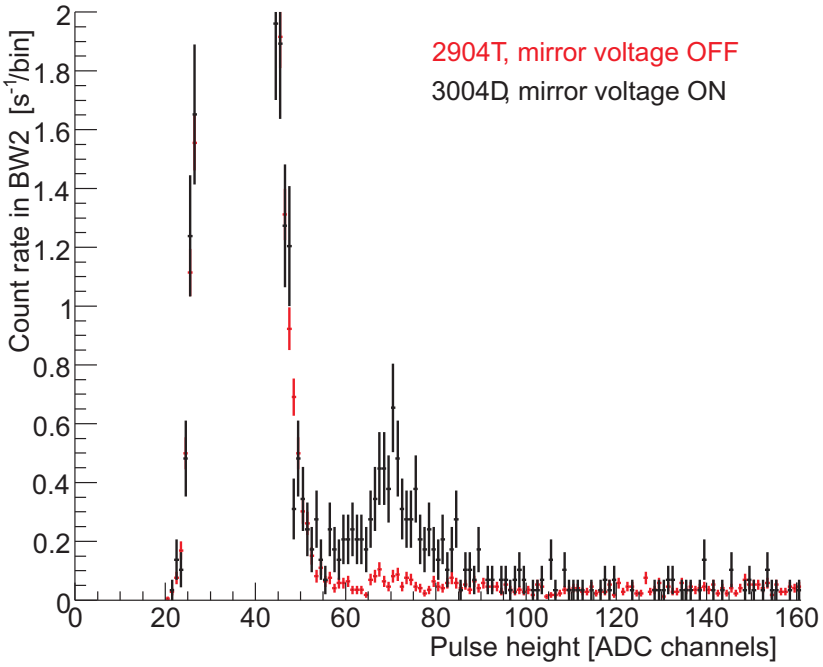

Figure 5.9: Pulse height histograms zoomed in the BW2 region with and without mirror voltage. When the mirror voltage is switched off no proton-like peak is seen.

taken within the *Cycle B* measurement period. Table 5.2 shows the count rate in BW2 and PCW at $U_A = 780$V and without mirror electrode. Notice that the background in the proton peak region (in BW2) was found to be smaller than 3 s^{-1}, that is, about half the one measured with the mirror electrode on during *Cycle B* (please also refer to Table 4.8 for better comparison).

Set of measurement cycles	Count rate in BW2 [s^{-1}]	Count rate in PCW [s^{-1}]
2904M	2.48(3)	38.6(1)
2904T	2.48(3)	38.2(1)

Table 5.2: Background count rates (i.e., $U_A = 780$ V) measured with neutron beam in BW2 and in PCW but without mirror voltage. The auxiliary data sets correspond to *2904M* and *2904T*. The finding is that the count rate in BW2 is reduced by a factor of 2 compared to *Cycle B* measurements with the mirror electrode switched on.

No visible proton-like peak has been detected in the pulse height histograms at $U_A = 780$ V for measurements without mirror electrode, see Fig. 5.9. The detector does not show accumulation of particles at its central channels, see Fig. 5.10.

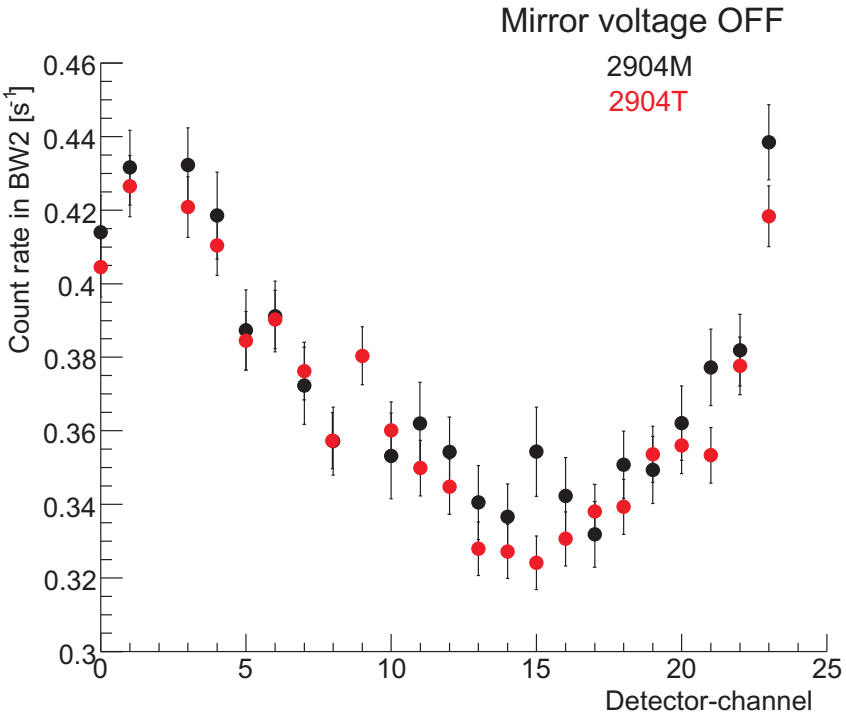

Figure 5.10: Flux tube profiles at the detector from auxiliary data sets of measurement-cycles taken at $U_A = 780$ V, with neutron beam on and mirror voltage switched off (*2904M* and *2904T*). A clear ∪-shaped profile is seen.

5.4.2 The other traps, P-I and P-IV

Positive residual gas ions created in trap **P-IV** will only pass the potential barrier in the anlyzing plane if U_A is lower than the potential at which they have been produced. In any case, the excess background due to these ions will not increase when increasing the analyzing plane voltage U_A as observed in Fig. 5.8. Therefore, trap **P-IV** can be excluded from the production of the excess background.

The Penning-like trap in the region between the electrodes $e16$ and $e17$, trap **P-I**, should not produce a background that depends on the analyzing plane voltage. This trap can be created by variations of the electric field on the edges of electrodes $e16$ and $e17$ in combination with the magnetic field, which at this region is very strong. Therefore, this trap is located off-axis and could enhance the background count rate detected at the outer detector-channels with respect to the inner detector-channels. Nevertheless, both electrodes $e16$ and $e17$ are held at high voltage and can emit electrons due to field emission processes.

Summary and Outlook

In this work, results from the first beam times of the aSPECT spectrometer at the neutron beam-line MEPHISTO at the Forschungsneutronenquelle Heinz Maier-Leibnitz (FRM-II), in Munich, are presented. aSPECT has been designed to provide very accurate measurements of the integral proton spectrum from free neutron decay. From these measurements, the antineutrino electron angular correlation coefficient a is expected to be extracted with an accuracy of better than 3×10^{-4}.

The data analysis of the first data taken with aSPECT demonstrates the capability of the spectrometer to measure the integral proton spectrum. However, an analyzing plane voltage dependent and fluctating background has been observed giving rise to an additional systematic error. Therefore, a definitive value of the angular correlation coefficient a based on data taken at FRM-II can not be reported.

The background instabilities have different origins. The less critical one is due to thermal noise of the proton detector, which partially overlaps with the proton peak. Its instability produces an increment of the proton count rate error bars, and consequently, a reduction in the accuracy of the extracted value of a. To reduce this type of background, a better separation of the thermal noise from the proton peak in the pulse height spectrum is needed.

Another source of unstable background is particle trapping inside the spectrometer, which adds an excess background in the proton peak region. This background has a proton-like peak shape and is observed in some measurements with different intensities. The existence of such excess background constitutes a severe systematic problem for determining a value of a. However, if a-values are extracted, it is found that measurements containing less excess background provide a-values closer to the currently recommended Particle Data Group value.

This excess background consists of positively charged particles whose count rate fluctuates with time and depends on the analyzing plane voltage. For higher analyzing plane voltages the measured excess background count rate is bigger. But, since background dependencies on the analyzing plane voltage have not been expected a priori, only one background level common to all analyzing plane voltages has been considered in the data acquisition and in the background subtraction process. Due to this fact, an off-line background correction is not possible. After this experience, in future aSPECT beam times it is highly recommended to have access to background measurements for several analyzing plane voltages without neutron beam. For instance, by the installation of a neutron beam shutter.

The creation of excess background in the energy range of proton events is assumed to be a complex process in which Penning traps are involved. These Penning traps are located along the spectrometer and can trap positively and negatively charged particles (see Fig. 5.7).

It is very unlikely that these traps are filled by particles created in neutron decay processes, but rather by an alternative particle source. Most probably the main electron sources are field emission and Penning discharge processes from the detector-electrode $e17$. These electrons travel along the spectrometer towards the mirror electrode, causing on their way ionization of the rest gas and creation of secondary electrons. Secondary electrons are less energetic and easier to be stored in Penning traps. Inside the trap, these electrons have more time to interact with the rest gas and produce positive ions. The latter ones, if detected, can not be distinguished from the signal of the decay protons.

The fact that the excess background count rate increases at higher analyzing plane voltages, suggests that negatively charged particles in the Penning trap located between the upper and the lower E×B electrodes (trap P-II in Fig. 5.7) play a decisive role in the creation of the excess background. Nevertheless, particles stored in the other Penning traps can contribute as well.

In order to reduce the excess background, small changes in the spectrometer can be implemented with the aim to avoid additional electron production processes, rest gas ionization or even Penning trap formation. Field emission and Penning discharges, could significantly be minimized by reducing the high voltage applied at the detector-electrode $e17$, as well as by improving the electrodes surfaces by polishing techniques. Better vacuum conditions would also reduce the probability of gas ionization processes. The usage of additional getter pumps in the main vacuum chamber could be a way to improve the UHV level. With the aim to eliminate the Penning trap located at the high voltage region (P-I trap), it is recommendable to increase the separation between the dipole electrode $e16$ and the detector-electrode $e17$. It is as well suggested to construct a new dipole electrode $e16$ with axial symmetric-shape to replace the currently used two-plate electrode in order to reduce the possibility that secondary electrons created outside the flux tube move radially towards the center of the spectrometer. Ions created inside the flux tube could then reach the detector and be counted as decay protons.

During April and May 2008, the spectrometer aSPECT performed its second beamtime at the Institute-Laue-Langevin, in Grenoble, France [Sim09] [Kon09]. For this beamtime, several of the modifications to the spectrometer proposed in this thesis have been realized, starting with the installation of a neutron beam shutter.

Also in this new beam time a new silicon drift detector (SDD) has been used [Nic06] [Gat84]. The acceleration voltages of the SDD-detector are typically in the range from -10 to -15 kV. This allows a drastical reduction of the acceleration voltage compared with the PIN-diode detector used at FRM-II. Additionally, as it is shown in Fig 5.11, the SDD-detector does not overlap thermal noise background with the proton peak, resulting in a noticeable reduction of background instability.

The probability of secondary electron production has been reduced by installing additional ion getter pumps, which have improved the UHV level by a factor of 3. Another

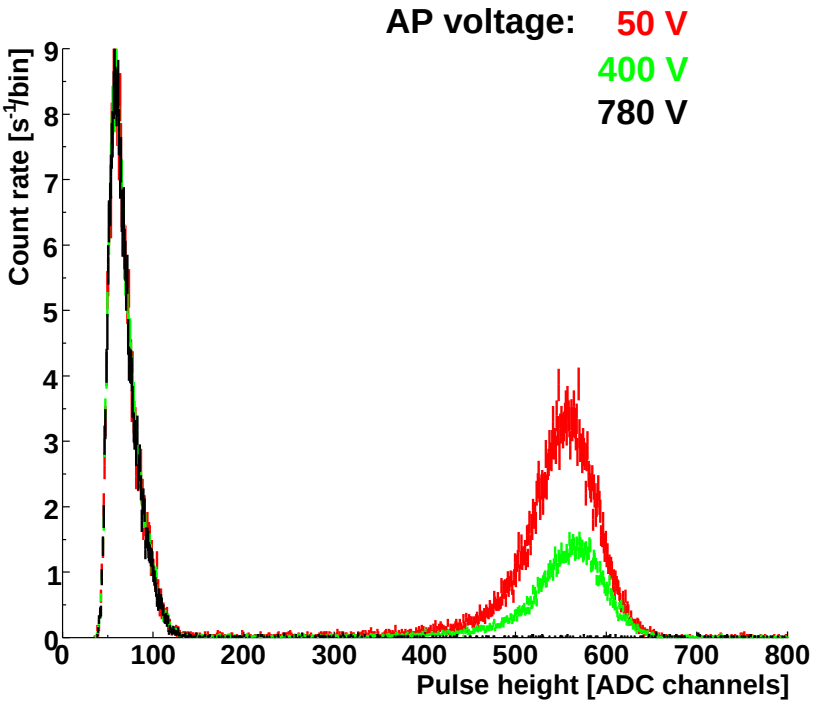

Figure 5.11: Pulse height spectra taken with *a*SPECT during its recent beam-time at the Institute-Laue-Langevin, in France. In this beam-time a new dilicon drift detector has been used. This plot has been taken with an acceleration voltage of -10 kV. Notice that the detector thermal noise is well separated from the proton peak.

effort has been devoted to redesign and polish parts of the electrode system to reduce field emission processes.

Although the data analysis of the last beam time is still under way (see [Aya11] [Bor11] [Kon11] [Sim10]), so far neither obvious background dependency on the analyzing plane nor proton-like background has been observed. As outcome, a big reduction of the background instabilities is expected. In that case, from the collected statistics a value of a with a total relative accuracy below 5% could be extracted.

Appendix A

Besides *Cycle A* and *Cycle B* data cycles, additional sets of measurement-cycles have been used as auxiliary-sets in the background analysis. Table 5.3 shows the settings of these measurement-cycles.

data sets / parameters	2504S	2604Background	2604Nnobeam
Main B [A]	50	50	50
High Voltage Electrode [kV]	-30	-30	-30
Neutron Beam	On	Off	Off
Mirror Voltage Electrode	On	On	On
Lower E × B Electrode [V]	several	-1000/-1150	-1000/-1150
Upper E × B Electrode [kV]	several	-4/-2	-4/-2
Time Meas. Cycle [s]	several	60	60
Number Meas. Cycles	25	113	20
Total duration [hours]	2.3	1.9	0.3
Frequency background measurements [Meas. Cycles]	2	4	4

data sets / parameters	2904D	2904U	2904T
Main B [A]	50	50	50
High Voltage Electrode [kV]	-30	-30	-30
Neutron Beam	On	On	On
Mirror Voltage Electrode	Off	On	Off
Lower E × B Electrode [V]	-1000/-1150	-1000/-1150	-1000/-1150
Upper E × B Electrode [kV]	-4/-2	several	-4/-2
Time Meas. Cycle [s]	180	180	180
Number Meas. Cycles	75	9	80
Total duration [hours]	3.8	0.5	4
Frequency background measurements [Meas. Cycles]	4	2	4

Table 5.3: Detailed settings of several measurement-cycles used for background analysis and that do not belong neither to *Cycle A* nor *Cycle B* data cycles.

Bibliography

[Abe97] Abele, H., *et al.*, 1997, Phys. Lett. B **407**, 212

[Abe02] Abele, H., M. A. Hoffmann, S. Baeßler, D. Dubbers, F. Glück, U. Müller, V. Nesvizhevsky, J. Reich, and O. Zimmer, 2002, Phys, Rev. Lett. **88**, 211801

[Abe08] Abele, H., 2008, Prog. Part. Nucl. Phys. **60**, 1

[Ams08] Amsler, C., *et al.*, 2008, *Particle Data Group*, Physics Letters B **667**, 1

[Ang04] Angrik, J. *et al.*, 2004, *KATRIN design report*, FZK Scientific Report **7090**

[Aya05] Ayala Guardia, F., 2005, Master's Thesis, Johannes Gutenberg-Universität Mainz

[Aya11] Ayala Guardia, F., 2011, PhD Thesis, Johannes Gutenberg-Universität Mainz. In progress.

[Arz00] Arzumanov, S., L. Bondarenko, S. Chernyavsky, W. Drexel, A. Fomin, P. Geltenbort, V. Morozov, Y. Panin, J. Pendlebury, and K. Schreckenbach, 2000, Phys. Lett. B **483**, 15

[Bae08] Baeβler, S. *et al.*, 2008, Eur. Phys. J. A **38**, 17

[Bai98] Baikie, I. D., P. Estrup, 1998, Rev. Sci. Instr. **69**, 3902

[Bea80] Beamson, G., Porter, H. Q., Turner, D. W., 1980, J. Phys. E **13**, 64

[Beg77] Beg, M. A. B. *et al.*, 1977, Phys. Rev. Lett. **38**, 1252

[Bjo63] Bjorken, J. D., Drell, S. D., 1963, *Relativistic Quantum Mechanics*, McGraw-Hill, New York

[Blu05] Blucher, E., *et al.*, 2005, Status of the Cabibbo Angle, arXiv:hep-ph/0512039

[Bop86] Bopp, P., D. Dubbers, L. Hornig, E. Klemt, J. Last, H. Schütze, S. J. Freedman, and O. Schärpf, 1986, Phy. Rev. Lett. **56**, 919

[Bor11] Borg, M., 2011, PhD Thesis, Johannes Gutenberg-Universität Mainz.

[Byr82] Byrne, J., 1982, *Weak interactions of the neutron*, Rep. Prog. Phys. **45**, 115

[Byr95] Byrne, J., 1995, *Neutrons, Nuclei and Matter*, Inst. Phys. Publ., Bristol

[Byr96] Byrne, J., P. G. Dawber, C. G. Habeck, S. J. Smidt, J. A. Spain, and A. P. Williams, 1996, Europhys. Lett. **33**, 187

[Byr02] Byrne, J., P.G. Dawber, M. G. D. van der Grinten, C.G. Habeck, F. Shaikh, J.A. Spain, R. D. Scott, C. A. Baker, K. Green, and O. Zimmer, 2002, J. Phys. G **28**, 1325

[Cab63] Cabibbo, N., 1963, Phys. Rev. Lett. **10**, 531

[Deh67] Dehmelt, H. G., 1967, Adv. At. Mol. Phys. **3**, 53

[Döh90] Döhner, J., 1990, Doctoral Thesis, Ruprecht-Karls-Universität Heidelberg

[Dew03] Dewey, M. S., *et al.*, 2003, Phys. Rev. Lett. **91**, 152302

[Dub91] Dubbers, D., 1991, Prog. Part. Nucl. Phys. **26**, 173

[Fer34] Fermi, E., 1934, *Zeitschrift für Physik* **88**, 161

[Fey58] Feynman, R. P. and Gell-Mann, M., 1958, Phys. Rev. **109**, 193

[Fow28] Fowler, R. H. and L. W. Nordheim, 1928, Proc. Soc. A **119**, 173

[Gam36] Gamow, G., and Teller, E., 1936 Phys. Rev. **70**, 572

[Gar57] Garwin, R. L., Lederman, L. M., and Weinrich, M., 1957, Phys. Rev. **105**, 1415

[Gar01] García, A., J. L. García-Luna, and G. López-Castro, 2001, Phys. Lett. B **500**, 66

[Gard01] Gardner, S., and Zhang, C. 2001, Phys. Rev. Lett. **86**, 5666

[Gat84] Gatti, E. and P. Rehak, 1984, Nucl. Instr. and Meth. A **225**, 608

[Gel60] Gell-Mann, M., and Levy, M., 1960, Nuovo Cimento **17**, 705

[Gla61] Glashow, S. L., 1961, Nucl. Phys., **22**, 579

[Glü93] Glück, F., 1993, Phys. Rev. D **47**, 2840

[Glü95] Glück, F., Joó, I., Last, J., 1995, Nucl. Phys. A, **593**, 125

[Glü05] Glück, F., *et al.*, 2005, Europhys. Journ. A **23**, 135

[Gol58] Goldhaber, M., Grodzins, L., and Sunyar, A. W., 1958, Phys. Rev. **109**, 1015

[Gor04] Gorringe, T., and H. F. Fearing, 2004, Rev. Mod. Phys. **76**, 31

[Hab97] Habeck, C. G., 1997, Doctoral Thesis, University of Sussex

[Her01] Herczeg, P., 2001, Prog. Part. Nucl. Phys. **46**, 413

[Hsu76] Hsu, T., Hirshfield, J. L., 1976, Rev. Sci. Instrum. **47**, 236

[Jam04] Jamin, M., Oller, J. A., and Pich, A., 2004, JHEP **02**, 047

[Jac57] Jackson, J. D., Treiman, S. B., and Wyld Jr., H. W., 1957, Phys. Rev. **106**, 517

[Jac75] Jackson, J. D., 1975, *Classical Electrodynamics*, John Wiley & Sons, 2^{nd} edition

[Jon09] Jones, G., 2009, *The aCORN experiment* Talk at 7th International UCN Workshop, Saint Petersburg, Russia

[Kob73] Kobayashi, M. and Maskawa, T., 1973, Prog. Theo. Phys. **49**, 652

[Kon09] Konrad, G., *et al.* 2009, Proceedings of the PANIC08 Conference. Eilat, Israel. Nucl. Phys. A, **827**, 529

[Kon10a] Konrad, G., 2010, Proceedings of the 5th International BEYOND Conference, Cape Town, South Africa, to be published in World Scientific, Singapore

[Kon10b] Konrad, G., 2010, *Privat communication*

[Kon11] Konrad, G., 2011, PhD Thesis, Johannes Gutenberg Universität-Mainz. In progress.

[Kra05] Kraus, Ch. *et al.*, 2005, Eur. Phys. J. C **40**, 447

[Kru83] Kruit, P., Read, F. H., 1983, J. Phys. E **16**, 313

[Lee56] Lee, T. D. and Yang, C. N., 1956, Phys. Rev. **104**, 254

[Leo94] Leo, W. R., 1994, *Techniques for Nuclear and Particle Physics Experiments*, Springer-Verlag, 2^{nd} edition

[Lia97] Liaud, P., K. Schreckenbach, R. Kossakowski, H. Nastoll, A. Baussière, J. P. Guillaud, and L. Beck, 1997, Nucl. Phys. A **612**, 53

[Lob85] Lobashev, V. M., Spivak, P. E., 1985, Nucl. Instrum. Methods A **240**, 305; Picard, A., Backe, H., Barth, H., Bonn, J. *et al*, 1992, Nucl. Instrum. Methods B **63**, 345; Weinheimer, Ch., Degen, B., Bleile, A., Bonn, J., Bornschein, L., Kazachenko, O., Kovalik, A., Otten, E. W., 1999, Phys. Lett. B **460**, 219

[Lon80] Lone, M. A., D. C. Santry and W. M. Inglis, 1980, Nucl. Instr. Meth. **174**, 521

[Mam89] Mampe, W., P. Ageron, C. Bates, j. M. Pendlebury, and A. Steyerl, 1989, Phys. Rev. Lett. **63**, 593

[Mam93] Mampe, W., *et al.*, 1993, JETP Lett. **57**, 82

[Mar88] Marciano, W. J., A. Sirlin, 1988, Phys. Rev. Lett. **61**, 1815

[Mar06] Marciano, W. J., A. Sirlin, 2006, Phys. Rev. Lett. **96**, 032002

[Moh75] Mohapatra, R. N., and Pati, J. C., 1975, Phys. Rev. D **11**, 566

[Mos00] Mostovoi, Y. A., Y. V. Gaponov, and B. G. Yerozolimsky, 2000, Phys. At. Nucl. **63**, 1193

[Mos01] Mostovoi, Y. A., I. A Kuznetsov, A. P. Serebrov, and B. G. Yerozolimsky, 2001, Phys. At. Nucl. **64**, 1955

[Mos76] Mostovoi, Y. A., Frank, A. I., 1976, JETP Lett. **24**, 38

[Mue05] Muehlbauer, M., 2005, Diploma Thesis, TU München

[Mun06] Muñoz Horta, R., *et al.*, 2006, Proceedings of the XIV International Seminar on Interaction of Neutrons with Nuclei. Joint Institute for Nuclear Research, Dubna, Russia.

[Nac68] Nachtmann, O., 1968, *Zeitschrift für Physik* **215(5)**, 505-514

[Nam60] Nambu, Y., 1960, Phys. Rev. Lett. **4**, 380

[Nes92] Nesvizhevsky, V., *et al.*, 1992, JETP Lett. **75**, 405

[Nic06] Niculae, A. *et al.*, 2006, Nucl. Instr. and Meth. A **568**, 336

[Osi01] Osipowicz, A., *et al.*, 2001, arXiv:hep-ex/0109033; Weinheimer, Ch., 2008, arXiv:hep-ex/0210050v2

[Ott08] Otten, E. W., Weinheimer, C., 2008, Rep. Prog. Phys. **71**

[Pat74] Pati, J. C., and Salam, A., 1974, Phys. Rev. D **10**, 275

[Pen36] Penning, F. M., 1936, Physica (Utrecht) **3**, 873

[Pet07] Petzoldt, G., 2007, Doctoral Thesis, Technische Universität München

[Rob58] Robson, J.M., 1958, Can. J. Phys. **36**, 1450

[Sal68] Salam, A., 1968, *Elementary Particle Theory*, Almquist Wiksells

[Sco68] Scott, G. B., M. Springford, and J. R. Stockton, 1968, Journ. of Phys. E **1**, 925

[Ser05] Serebrov, A., *et al.*, 2005a, Phys. Lett. B **605**, 72

[Sim06] Simson, M., 2006, Master's thesis, Technische Universität München.

[Sim09] Simson, M., *et al.* 2009, Proceedings of the IWPPSN Workshop 2008. Institut Laue-Langevin, Grenoble, France. Nucl. Instr. and Meth. A, **611**, 203

[Sim10] Simson, M., 2010, PhD Thesis, Technische Universität München.

[Sev06] Severijns, N., Beck, M., Naviliat-Cuncic, O., 2006, Rev. Mod. Phys. **78**, 991

[Spi88] Spivak, P. E., 1988, Sov. Phys. JETP **67**, 1735

[Sch07] Schumann, M. 2007, Doctoral Thesis, Universität Heidelberg

[Str78] C. Stratowa, R. Dobrozemsky, and P. Weinzierl, 1978, Phys. Rev. D **18**, 3970

[Sud58] Sudarshan, E. C. G. and Marshak, R. E., 1958, Phys. Rev. **109**, 1860

[Tow02] Towner, I. S., Hardy, J. C., 2002, J. Phys. G:Nucl. Part. Phys. **29** 197

[Tow07] Towner, I. S., Hardy, J. C., 2007, arXiv:0710.3181v1

[Yao06] W.-M. Yao et al., 2006, J. Phys. G **33**, 1

[Rit99] van Ritbergen, T., Stuart, R.G., 1999, Phys. Rev. Lett. **82**, 488

[Vla61] Vladimirskii, V. V., 1961, Sov. Phys.-JETP **12**, 740

[Wei67] Weinberg, S., 1967, Phys. Rev. Lett. **19**, 1264

[Yer97] Yerozolimsky, B., I. Kuznetsov, Y. Mostovoy, and I. Stepanenko, 1997, Phys. Lett. B **412**, 240

[Wei58] Weinberg, S., 1958, Phys. Rev. **112**, 1375

[Wie05] Wietfeldt, F. E., 2005, Nucl. Instr. Methods Phys. Res. A **545**, 181

[Wu57] Wu, C. S., Ambler, E., Hayward, R. W., Hoppes, D. D., and Hudson, R. 1957, Phys. Rev. **105**, 1413

[You02] Young, A., 2002, Talk at the Workshop on Quark-Mixing and CKM-Unitarity, Heidelberg, Germany

[Zie06] Ziegler, J. F. *et al.*, 2006, SRIM - The Stopping and Range of Ions in Matter. Computer Program. http://www.srim.org

[Zim00] Zimmer, O., J. Byrne, M. G. D. v.d. Grinten, W. Heil, F. Glück, 2000, Nucl. Inst. Meth. A **440**, 548